In-situ spectroscopic studies of electrocatalytic electrodes

Walker, Rachel Claire

Award date:
1998

Awarding institution:
University of Bath

In-situ Spectroscopic Studies of Electrocatalytic Electrodes

submitted by Rachel Claire Walker

for the degree of PhD

of the University of Bath

1998

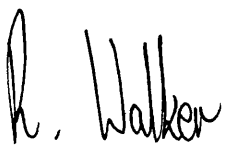

Rachel C. Walker

ProQuest LLC
789 East Eisenhower Parkway
P.O. Box 1346
Ann Arbor, MI 48106-1346

University of Bath

School of Chemistry

Doctor of Philosophy

In-situ Spectroscopic Studies of Electrocatalytic Electrodes

By Rachel Claire Walker

ABSTRACT

Potential modulated reflectance spectroscopy (PMRS) is a powerful *in-situ* technique which enables changes in optical properties of the electrode-electrolyte interface to be monitored as a function of an externally applied, varying potential bias. This technique is able to observe changes in the surface state(s) of an electrode and / or dissolution processes. In this work, PMRS has been employed to study the anodic behaviour of electrocatalytic electrodes, namely Ru metal and Ru-Ir alloy anodes.

A theoretical expression for the optical response of a redox system has been derived and related to Faradaic admittance for both a diffusion-controlled and a surface bound redox process. The ferro-ferricyanide redox couple has been used as a model diffusion-controlled process to verify this relationship. A PMRS study of this simple reversible redox system demonstrates how spectroscopic and kinetic information can be obtained from the frequency dependent optical response.

A PMRS study of the anodic oxidation of ruthenium identified soluble RuO_4^{2-} (Ru(VI)) and RuO_4^- (Ru(VII)) species formed at the onset of oxygen evolution in alkali media. The PMR spectra exhibit an isosbestic point that is attributed to the RuO_4^{2-} /RuO_4^- redox couple. Frequency response analysis of the optical response in the same potential region identified a diffusion-controlled process which supports the solution

RuO_4^{2-}/RuO_4^- redox couple identified by PMRS. The same study also identified the presence of a surface redox process in the high frequency range. This is attributed to a change in stoichiometry of RuO_{2-x} to $RuO_{2-x+\delta x}$. PMRS studies of ruthenium dissolution in acid solutions indicate that RuO_4 is the only identifiable corrosion product formed in the oxygen evolution region.

The anodic behaviour of a ruthenium-iridium mixed alloy ($Ru_{0.4}Ir_{0.6}$) was also investigated by PMRS. The PMR spectra correlate well with reported PMR spectra for anodically grown iridium oxide films in alkali media. No corrosion products were identified. It is concluded that the surface electrochemistry of a $Ru_{0.4}Ir_{0.6}$ alloy is dominated by iridium, probably as a result of surface segregation.

Acknowledgements

Many thanks must go to my supervisor, Professor Laurence M. Peter for all his guidance, knowledge and advice which has been invaluable. I would also like to thank Dave Hodgson for the support and encouragement he has given me over the past three years as my industrial supervisor.

I am also very thankful to Laurent Beden, whom I worked in conjunction with during the study of the model ferro-ferricyanide system. He very kindly made his results on the frequency dependent response of ferro-ferricyanide available for publication in this thesis. Thank-you.

Thank-you must also go to Dr. Mike Bailes, for without his help in the understanding of computer soft-ware and electronics, I would certainly be no nearer understanding a lock-in amplifier now than I was three years ago! Thanks also to the technical support of Mr. Mike Lock of the Science Workshop at the University of Bath.

Of course, a big thank-you to everyone in the Electrochemistry group, with whom I have worked. Dr. Adrian Fisher, Gabry, Ruilin, Noel, Nick, Upal, Alice, Nicki, Khaled, and to the dearly departed, Jason, Rob, Mark, David, Sabino and of course Laurent.

To my family, for all their support and encouragement during my time at Bath, I am eternally thankful. Yes, I will start paying my taxes now! And finally a big thank-you to all my friends (drinking companions) you know who you are, who managed to keep me sane over the final few months!

Thank-you everyone

Rachel

Dedicated to :

Mum and Dad

List of Symbols

Symbol	Meaning	Units
A	cross-sectional area of an electrode	cm^2
$\mathcal{A}$	absorbance	
C_a	concentration of species a	mol cm^{-2}
d	optical path length	cm
E	potential of an electrode versus a reference	V
E_e	equilibrium potential	V
E^o	a) standard potential of an electrode	V
	b) standard emf of a half-reaction	V
$E^{o'}$	formal potential of an electrode	V
E_{ac}	*ac* component of potential in PMRS	V,mV (rms)
E_{dc}	*dc* component of potential in PMRS	V, mV
E_o	amplitude of modulation of *ac* potential signal	V, mV (rms)
i	current	A
I_F	Faradaic current	A
I	intensity of light	
I_o	intensity of incident light beam	
ΔI	amplitude of the modulated light intensity	
j	current density	mA cm^{-2}
j_o	exchange current density	mA cm^{-2}
j_{op}	operating current density of chlor-alkali cells	A m^{-2}
N_d	electron density in semi-conductors	
n	electrons per molecule oxidized or reduced	
O	reduced form of the standard system, $O + ne^- \rightleftharpoons R$	
Q	Charge density	C cm^{-2}
R	oxidised form of the standard system, , $O + ne^- \rightleftharpoons R$	
R	resistance	Ω
R_{ct}	charge transfer resistance	Ω
ΔR	amplitude of the *ac* optical response	
S	an electrocatalytic site at an electrode surface	
T	transmittance, ratio I/I_o	
x	distance, usually from an electrode surface	cm

Y	admittance	Ω^{-1}
Y_F	Faradaic admittance	Ω^{-1}
Z	impedance	Ω
Z_F	Faradaic impedance	Ω

Greek symbols

α	transfer coefficient	none
	molar absorption coefficient	cm^{-1}
δ	diffusion layer thickness at an electrode-electrolyte interface	cm
ε	molar extinction coefficient	$M^{-1}\ cm^{-1}$
Γ	concentration of surface species	$mol\ cm^{-2}$
η	overpotential, E-E_e	V/mV
θ	degree of surface coverage of an anode	
λ	wavelength of light	nm
σ	$\sigma = \frac{RT}{n^2F^2A\sqrt{2}}\left(\frac{1}{D_O^{1/2}C_O^*}+\frac{1}{D_R^{1/2}C_R^*}\right)$	$\Omega\ sec^{1/2}$
ρ	electromodulation reflection coefficient$=\frac{1}{R}.\frac{dR}{dE}$	
ω	frequency of an *ac* signal ($\omega=2\pi f$)	Hz

Subscripts / Superscripts

A	anodic
C	cathodic
F	Faradaic
ac	*ac* component
dc	*dc* component

Abbreviations

AIROF	anodic iridium oxide film
CIS	colour impedance spectroscopy
DSA	dimensionally stable anode
ECMS	electrochemical modulation spectroscopy
EER	electroreflectance effect

EOT	electro-optical transmittance= $\frac{\Delta T}{\Delta E.T}$
ITO	indium-doped tin oxide
MSRS	modulated specular reflectance spectroscopy
PANI	polyanaline
PMRS	potential modulated reflectance spectroscopy
RTO	RuO_2/TiO_2 mixed oxide
SAM	scanning Auger microscopy
SEM	scanning electron microscopy
SMACRS	sinusoidally modulated *ac* reflectance spectroscopy
SNFTIRS	surface-normalised interfacial fourier transform infra-red spectroscopy
TEM	transmission electron microscopy
XPS	X-ray photoelectron spectroscopy
XRD	X-ray diffraction

Contents

Chapter 1

Chapter 1

Electrocatalytic Electrodes : An Introduction

Electrocatalytic electrodes play a major part in the chlor-alkali industry as anodes for the electrolysis of brine to produce chlorine. The introduction of RuO_2/TiO_2 based anode systems in particular or 'Dimensionally Stable Anodes' (DSAs®) [1] has stimulated research aimed at improving understanding of the mechanism of chlorine evolution and also of oxygen evolution [2]. This chapter discusses the industrial development of DSAs® in the chlor-alkali industry and reviews some of the research on the kinetics and mechanism of chlorine and oxygen evolution.

1.1 The Chlor-Alkali Industry

Chlorine production involves electrolysis of an aqueous electrolyte of ~30% aqueous sodium chloride (brine) at pH 2-4 and a temperature of 75-90°C [3]. The passage of electrical current through the brine solution results in the evolution of chlorine at the anode. The corresponding reaction at the cathode results in the formation of hydrogen. The mechanism is shown below.

At the anode : $2Cl^- \rightleftharpoons Cl_2 + 2e^-$ $\qquad E^o_{298} = 1.36V$ $\qquad (1.1)$

At the cathode : $2H_2O + 2e^- \rightleftharpoons H_2 + 2OH^-$ $\qquad E^o_{298} = -0.83V$ $\qquad (1.2)$

Giving overall :

$$2NaCl + 2H_2O \rightarrow 2NaOH + Cl_2 + H_2 \qquad E^o_{298} = 2.19V \qquad (1.3)$$

Ideally, the evolution of Cl_2 at the anode should occur at pH ~3-4 in order to prevent the formation of hypochlorite from Cl_2, as well as to minimise the competing O_2 evolution reaction due to water oxidation at the anode. The pH at the cathode is ~14 as a result of the generation of OH^-.

Chlorine and sodium hydroxide produced from the electrolysis of brine have a variety of uses in the chemical industry and examples are summarised in **Table 1.1**. Hydrogen is also used to a lesser extent as a chemical in the hydrogenation of fats and also as a fuel in fuel cells [3].

Chlorine:
Manufacture of polyvinylchloride (20)
Preparation of chlorinated organic solvents, e.g. methylene chloride, chloroform, carbon tetrachloride, *per-* and *tri*-chloroethylene, 1,1,1-*tri*-chloroethane (26)
Preparation of propylene oxide (8)
Synthesis of other organic compounds, e.g. chlorobenzenes, alkyl chlorides (particularly methyl chloride for lead alkyls), herbicides (7)
Preparation of fluorocarbons (4)
Pulp and paper manufacture (14)
Preparation of inorganic compounds, e.g. sodium hypochlorite, titanium tetrachloride, iodine chlorides (12)
Water treatment (4)
Sodium hydroxide (Caustic soda):
Synthesis of many organic compounds (38)
Manufacture of textiles and rayon (5)
Soap and detergent production (5)
Oil refining (5)
Paper and pump manufacture (20)
Aluminium extraction (4)
Manufacture of inorganic compounds, e.g. sodium cyanide, sodium salts (11)

* Figures in brackets are percentages of US production (taken from E. Spore and B. V. Tilak (1987)) *J. Electrochem. Soc.*, 134, 179c.

Table 1.1 : Major uses of chlorine and sodium hydroxide [3].

Three types of cells are used for commercial chlorine production by the electrolysis of brine.

1.1.1 The mercury cell [3,4]

The anode used is a mesh coated with a RuO_2-TiO_2 mixed oxide. The cathode is flowing liquid mercury. During electrolysis, sodium ions are reduced to sodium which

dissolves in the mercury cathode and forms an amalgam. Following its removal from the cell, the amalgam is decomposed through contact with water and carbon pieces to produce sodium hydroxide (caustic soda) and hydrogen. The highly concentrated solution of sodium hydroxide (50%) of high purity and low Cl^- concentration, is removed and the sodium-free mercury is recirculated into the cell for re-use. The two electrochemical processes are

$$\text{At the anode : } 2Cl^- \rightleftharpoons Cl_2 + 2e^- \qquad E^o_{298} = 1.36\text{V} \qquad (1.4)$$

$$\text{At the cathode : } Na^+ + Hg + e^- \rightleftharpoons Na(Hg) \qquad E^o_{298} = -1.87\text{V} \qquad (1.5)$$

Decomposition of the sodium amalgam occurs according to :

$$2Na(Hg) + 2H_2O \rightarrow 2Hg + 2Na^+ + 2OH^- + H_2 \qquad (1.6)$$

The standard emf for the mercury cell is therefore 3.23V, ~1V higher than the E^o for Cl_2 evolution according to Eq. (1.1) and Eq. (1.2). The overall operating cell voltage is ~4.6V due to electrode polarisation and ohmic losses [4]. **Figure 1.1** illustrates the mercury cell.

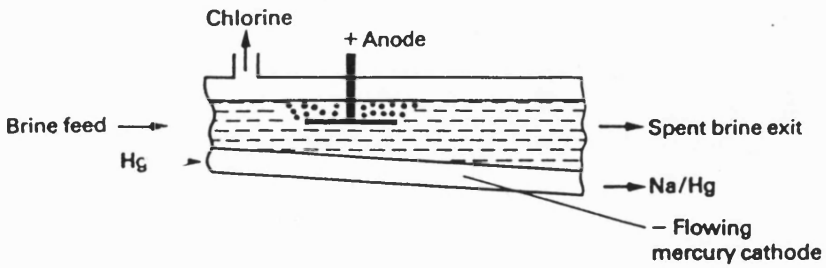

Figure 1.1 : A schematic of the mercury cell [4].

1.1.2. The diaphragm cell [3,4]

The diaphragm cell was introduced after the mercury cell to address increased environmental demands to reduce the use of mercury in the electrolysis process. In this cell, the cathode and anode are placed vertically in two compartments that are separated from each other by a diaphragm. The cathode is made of steel coated with a Ni catalyst. The anode is in the form of a DSA® as for the mercury cell. The reactions at each electrode follow Eq. (1.1) and Eq. (1.2).

The diaphragm consists of asbestos and additives. It acts as a separator, through which ions and electrolyte can flow between the anode and cathode compartments as a result of hydrostatic pressure. The diaphragm also minimises the mixing of the products formed at the two anodes, which would result in the formation of unwanted by-products e.g hypochlorite / chlorate. However, the passage of Cl^- ions through the diaphragm results in contamination of the caustic soda. As a result, caustic soda is formed at a lower concentration (~12%) and purity than in the mercury cell, with a significant amount of Cl^- (15%) remaining in the electrolyte. The savings made by the reduced cell voltage are therefore balanced by the cost of purifying the caustic soda, making the mercury and diaphragm cell similar in price to operate. The diaphragm cell is illustrated in **Figure 1.2**.

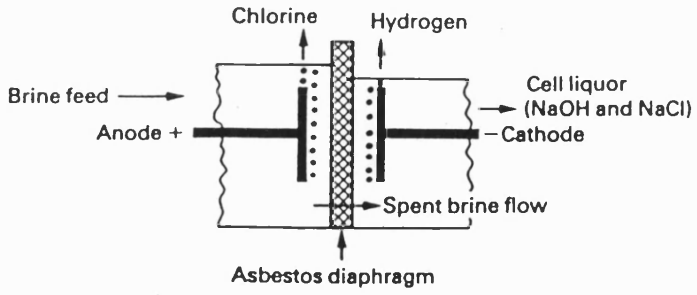

Figure 1.2 : A schematic of the diaphragm cell [4].

1.1.3 The membrane cell [3,4]

The membrane cell was introduced in the 1970s following the development of perfluorinated ionomer membranes. These membranes offer good stability to chlorinated brine and concentrated caustic soda at the cell conditions of 90°C, high conductivity, high cation transport number and good mechanical strength. They act as a separator, allowing only sodium ions to pass through them. The passage of Cl^- and OH^- through the membrane is therefore not possible, which ensures that the catholyte and anolyte are completely separated. As a result, the caustic soda formed is free of Cl^- ions. Cl_2 is again evolved at the anode with H_2 at the cathode as for the diaphragm cell.

The membrane cell has proved to be the most energy efficient of the three cell types, combining the high purity, Cl^- free caustic soda (~35%) performance of the mercury cell with the low cell voltage performance (3.1V) of the diaphragm cell. **Figure 1.3** illustrates the membrane cell.

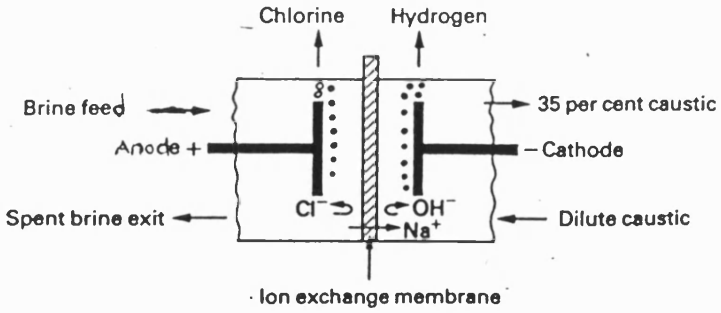

Figure 1.3 : A schematic of the membrane cell [4].

1.2 Electrocatalytic Electrodes : Their development in the chlor-alkali industry

Following the introduction of RuO_2/TiO_2 based anodes as electrocatalytic electrodes in the chlor-alkali industry, research has been based on developing an

understanding of electrocatalytic performance of the anode and the properties which contribute to it [2,5-8].

1.2.1 Electrocatalysis

Electrocatalysis is a term used to describe the acceleration or promotion of a particular electrode reaction. Both thermodynamic and kinetic properties need to be considered when looking at the electrocatalytic performance of a particular anode. The cell potential for the reaction of interest E_{CELL}, incorporates some of these properties and can be represented as follows :

$$E_{CELL} = E_e^C - E_e^A + |\eta_C| + |\eta_A| + |i|R_{CELL} + |i|R_{CIRCUIT} \qquad (1.7)$$

E_e^C and E_e^A are the equilibrium potentials for the anode and cathode respectively, $|\eta_c|$ and $|\eta_A|$ the overpotentials for the respective electrodes and $|i|R_{CELL}$ and $|i|R_{CIRCUIT}$ correspond to the ohmic drops in the cell and circuit. The overpotential η, corresponds to the difference between the equilibrium potential and the observed potential at the electrode, where $\eta = E - E_e$. Clearly, E_{CELL} is directly related to the difference in equilibrium potential at the anode and cathode. The difference in equilibrium potential is a thermodynamic property and therefore dependent on pH, [Cl^-] and also temperature T. The value should be independent of electrode material. In contrast, overpotential η is a kinetic property that depends on the electrode material and is directly related to the current density j_o , and therefore to the Tafel slope dη/d(log j) (See Section 1.6 for details). The ohmic drops in the circuit and cell are a matter of cell design. An electrode can therefore be classified as more electrocatalytic than another if, at a constant

overpotential, the electrode reaction of interest proceeds at a higher rate i.e. higher current density j.

If we consider the Cl_2 evolution process, there are in fact two processes possible at the anode as shown :

$$2Cl^- \rightleftharpoons Cl_2 + 2e^- \qquad E^o_{298} = 1.36V \qquad (1.8)$$

$$2H_2O \rightleftharpoons O_2 + 4H^+ + 4e^- \qquad E^o_{298} = 1.23V \qquad (1.9)$$

O_2 evolution is more thermodynamically feasible than Cl_2 evolution over the pH range 0-14. Since the overpotential is dependent on electrode material, it is therefore desirable to have an anode material which has a high overpotential for oxygen evolution and low overpotential for Cl_2 evolution, to a point where Cl_2 evolution becomes kinetically viable. In the case of the RuO_2 electrode [8], as the pH decreases from 14 to 0 a crossover point between the overpotential for O_2 and Cl_2 evolution occurs at pH 4. At <pH 4, Cl_2 evolution becomes kinetically more viable. This supports the development of chlor-alkali cells which function at pH 2-4 during electrolysis.

It is clear that overvoltage and current density play important roles in assessing the electrocatalytic performance of an electrode. In industry however, the primary factor which determines the performance of an electrode is cost per unit product. This factor, together with the electrochemical factors discussed above, have led industry to place several technological demands on electrode design which are summarised below [7].

a. Increase the electrocatalytic activity for wanted reactions e.g. Cl_2 evolution.

b. Decrease the electrocatalytic activity for unwanted reactions e.g. O_2 evolution.

c. Increase the stability of electrode materials towards wear.

d. Increase the operating current density j_{op}.

e. Develop new materials to reduce cost and address environmental issues.

f. Ensure the cycle life is consistent with other components (e.g. membranes).

As a result of these demands, there has been a considerable amount of research aimed at developing efficient anode materials for Cl_2 evolution. The next section will discuss the developments made in this area over the past 30 years.

1.2.2 The development of anode systems in the chlor-alkali industry

Prior to the introduction of DSAs®, graphite anodes had been used as electrodes for Cl_2 evolution due to their reasonable chemical inertness during Cl_2 evolution [4]. The major problem with the graphite anode was that of high wear-rate, where carbon was lost as carbon dioxide. This resulted in a lowering of the electrocatalytic performance of the anode during Cl_2 evolution and led to replacement of the anodes on a near yearly basis. The high wear-rate, together with a low electrical conductivity and high overpotential for Cl_2 evolution, resulted in the demand for a more stable and efficient anode system.

H.B. Beer first introduced the concept of the use of coated-metal anodes for chlorine production in the 1950s [9]. Titanium was selected as the substrate on which to deposit the anode due to the corrosion resistance of titanium [5,9]. It was established that titanium formed an inert oxide film that prevented corrosion of the substrate during electrolysis. However, the film still allowed conduction to the electroactive films deposited on it. As a result of the stability of the Ti substrate, platinum coated titanium anodes, formed by electrodeposition were introduced in 1958. A high overpotential for Cl_2 evolution at Pt anodes [9], as well as surface passivation of Pt which is accompanied

by corrosion of the film [10,11], led to the development of 70/30 Pt-Ir coatings (of the form platinum metal-iridium oxide) for use in the chlor-alkali industry. Problems associated with cost then led to the introduction of Beer's first ruthenium-based mixed oxide system, which was patented in 1965 [12].

The aim of Beer's work was to develop a DSA® system which satisfied the industrial demands. The RuO_2-based anode proved superior in all these respects, with long-term dimensional stability and lower overpotential for Cl_2 evolution compared to the graphite anode. A second patent quickly followed in 1967 which involved the codeposition of a RuO_2/TiO_2 (RTO) coating on a titanium substrate, with a lower ruthenium oxide content of <50% [13]. It was found that as the weight % of RuO_2 in the RTO anode decreased then the oxygen / chlorine electrode overpotential difference increased, making Cl_2 evolution more favourable.

These findings, together with the improved stability of RuO_2 as a result of codeposition with titanium, resulted in the development of what are now referred to as DSAs®, so called because they are inert and stable to corrosion but electrochemically active. They therefore maintain their dimensions over a long period of time and have a service life of several years. This is in contrast to graphite anodes where replacement was necessary on a yearly basis due to rapid corrosion. RuO_2-TiO_2 (RTO) anodes with RuO_2 at *ca.* 30-40 mole %, are widely used for commercial chlorine production today [3].

Following the introduction of RuO_2-based anodes in the chlor-alkali industry, there has been a drive towards the development of other RuO_2-based mixed oxide systems with improved stability, selectivity and cost effectiveness [14-23]. The replacement of TiO_2 with SnO_2 or IrO_2 in RTO anodes has been shown to improve stability of the anode and also selectivity towards Cl_2 and O_2-evolution [14-16]. Ternary mixed oxides such as

Ru-Ti-Sn, Ru-Ir-Sn, Ru-Ti-Pt and Ru-Ti-Ce have proved attractive as possible future anodes [17-23]. The use of RuO_2-based electrodes as cathodes in water electrolysis for the generation of hydrogen has also attracted interest [24,25].

1.3 Film Preparation

RuO_2 films are generally prepared by thermal decomposition of a precursor, $RuCl_3.3H_2O$ on a titanium substrate [26]. Titanium is chosen as a substrate due to its passivating properties (see Section 1.2). The Ti substrate is etched in hot aqueous oxalic acid prior to thermal decomposition, in order to produce a roughened surface of high surface area. This aids adhesion of the film to the substrate.

The $RuCl_3.3H_2O$ precursor is dissolved in an organic solvent, usually isopropanol and the resulting solution is applied to the etched titanium substrate. The electrode is then heated in air at a temperature of 300-500°C for 1-5 minutes to evaporate the solvent and decompose the Ru salt to give a conducting film. This procedure is repeated, building up layers until the desired film thickness (generally a few microns) is achieved. The final coating is fired at a temperature of ~450°C for 0.5-1 hour to oxidise the film.

RTO mixed oxide films are also prepared by a similar thermal decomposition process. The solvent solution in this case contains $RuCl_3.3H_2O$ and Ti isopropoxide. Commercial RTO anodes used in the chlor-alkali industry have a composition of 30 mole % RuO_2 + 70 mole % TiO_2.

1.4 RuO_2-based Anodes : Structural and morphological properties

It is widely accepted that the structural and morphological properties of RuO_2-based anodes effect their electrocatalytic performance. It is therefore important to

develop a good knowledge of these properties in order to gain a full understanding of the effect they have on the efficiency of the anode system under study. Since the RTO anode is the most widely used system in the chlor-alkali industry, the discussion will be focused on this mixed oxide.

The structural and morphological properties of the individual components of the RTO anode are key factors in determining the resultant properties of the mixed oxide system. Therefore, some of the structural properties of the individual components of RTO anodes, RuO_2 and TiO_2 have been summarised in **Table 1.2.**

Compound	*Structure*	*Shape*	*Electron configuration*
RuO_2	Rutile	Tetragonal	$4d^4$
TiO_2	Rutile / Anatase	Tetragonal	$3d^0$

Table 1.2 : A summary of some of the structural and electronic properties of the RTO oxide components [27,28].

X-ray analysis of RTO anodes has been used to gain an understanding of the morphology of the anode films [29,30]. Two phases have been identified in RTO mixed oxide films, a rutile structure of the mixed oxide, RuO_2-TiO_2 together with an anatase structure of TiO_2 [29]. The amount of each phase was found to be directly related to the composition of the oxide. The amount of the rutile mixed oxide phase decreases sharply with RuO_2 <40 mole % and is accompanied by a corresponding increase in the amount of the anatase phase. X-ray diffraction studies (XRD) have shown that RTO anodes form solid solutions when annealed at temperatures in the range of 350-600°C, where complete miscibility between the two oxides occurs [30]. At higher temperatures (700-

800°C), X-ray diffraction patterns indicate that two separate phases of pure RuO_2 and TiO_2 exist.

Scanning electron microscopy (SEM) [31,32] has provided morphological information on the surface of thermal RuO_2 and RTO films. A characteristic honeycomb structure has been identified for RuO_2 films, where each cell is separated by narrow and deep channels. This structure is generally referred to as a "mud-cracked" structure. The porosity of the walls of the cells for RuO_2 films was found to increase with an increase in annealing temperature [31]. Scanning Auger microscopy (SAM) confirmed a cracked-mud structure for RTO films and identifed segregation of RuO_2 in the cracks of RTO films [33]. RuO_2 films formed electrochemically by potential cycling at Ru anodes, have also been investigated using SEM and transmission electron microscopy (TEM) [34] and a porous structure was observed. **Figure 1.4** illustrates typical SEMs for RuO_2 and RTO films.

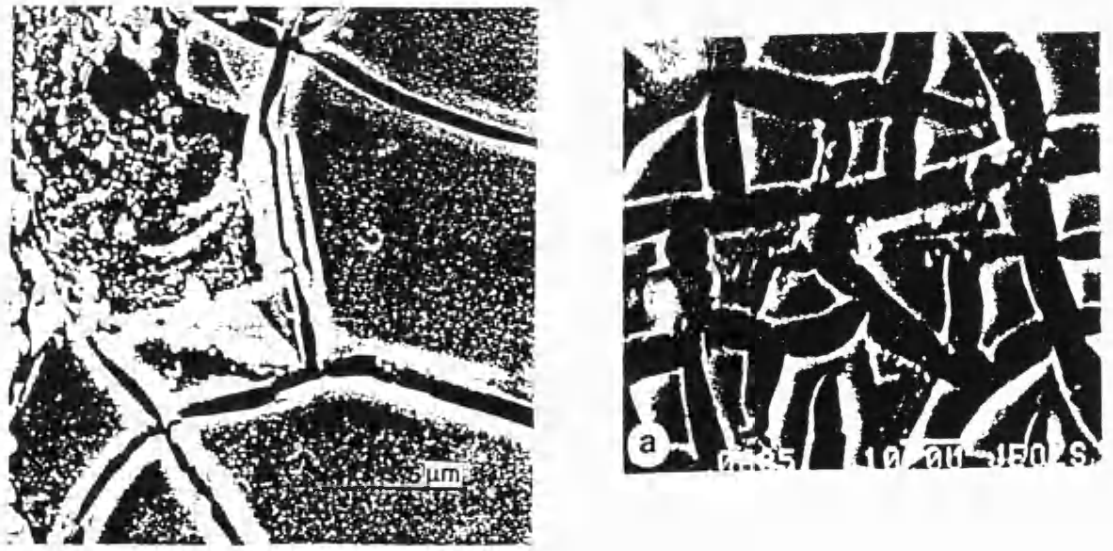

RuO_2 film RTO film

Figure 1.4 : SEM of RuO_2 and RTO films [31,32]

1.5 Electrical and Physical Properties of RuO_2-based Anodes

1.5.1 Non-stoichiometry in RuO_2-based anodes

It has been established that RuO_2 films have a non-stoichiometric structure [2]. However, there still appears to be uncertainties as to the exact nature of the non-stoichiometry. Oxygen deficiency in RuO_2 films has been reported [35] using chemical analysis and residual chlorine in both RuO_2 and RTO films has been confirmed by secondary ion mass spectrometry (SIMS) [36], chemical analysis [37] and X-ray spectrometry [32]. The presence of Ru^{3+} in RuO_2 films has also been proposed [38,39]. It is postulated that the chlorine ions could exist in oxygen lattice positions, where the difference in charge is compensated by the presence of Ru^{3+} ions.

However, the degree of non-stoichiometry is affected by the film preparation conditions. Both the amount of Ru^{3+} in RuO_2 films [39] and residual chlorine in RuO_2 [37] and RTO films [32] have been reported to decrease with an increase in annealing temperature. Oxygen deficiency has been shown over a large temperature range, with a decrease in deficiency as the temperature increases [37]. However, despite these studies the exact structure of RuO_2-based films is still far from certain.

1.5.2 The conductivity of RuO_2-based anodes

The conductivity of RuO_2-based anodes has been a source of debate since their introduction in the chlor-alkali industry. There have been several conflicting reports as to the nature of the conductivity of the anodes. RuO_2 in the form of a single crystal is known to behave as a metallic conductor. The characteristic increase in resistivity with increasing temperature has been reported and resistivity values of the order of 35-40$\mu\Omega$ cm at room temperature have been obtained [40,41]. In contrast, TiO_2 acts as an oxygen-deficient *n*-type semiconductor in the rutile form [42]. In the case of RuO_2 films

formed by the thermal decomposition process, authors have reported both quasi-metallic conductivity [26, 32] and semiconductor behaviour [30,31,37,43]. RTO anodes show a semi-conductor - conductor transition at RuO_2 ~20-30 mole % with metallic conductivity reported for RuO_2 > 30 mole % [32,44].

The metallic conductivity of RuO_2-based films has been attributed to the overlap of inner *d*-orbitals of neighbouring cations [32]. This is said to enable conduction via *d*-electrons in the partially filled *d*-bands (Ru-O π^*band) [27]. It can be represented by the following band-energy diagram. The band-energy diagram of TiO_2 is also shown for comparison.

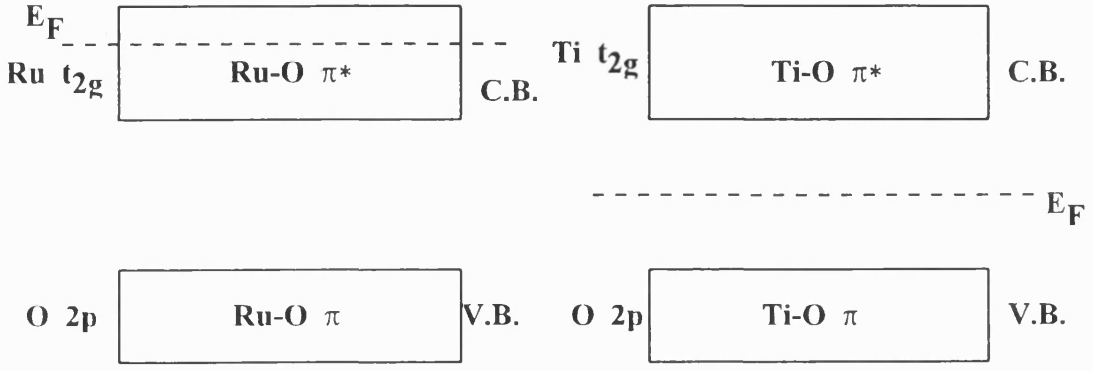

Figure 1.5 : A band-energy diagram of RuO_2 and TiO_2 films based on Ref. [27].

The conductivity observed has also been attributed to the non-stoichiometric nature of the oxide [26,35,38]. One possibility is that oxygen vacancies formed as a result of oxygen deficient non-stoichiometry [35] i.e. RuO_{2-x}, generate electrons in the conduction band. This results in *n*-type conductivity. Provided that the concentration of vacancies is high enough, the Fermi level, E_F enters the conduction band. The material becomes a degenerate *n*-type semi-conductor which shows the semi-conducting behaviour observed by several authors. **Figure 1.6** illustrates this behaviour.

However, the effect of annealing temperature on conductivity of RuO_2 films contradicts the proposal that the conductivity of RuO_2 films is an effect of the degree of

non-stoichiometry. An increase in annealing temperature is accompanied by an increase in conductivity of the films [37]. Therefore at room temperature, the low conductivity is in contrast to the large degree of non-stoichiometry, which decreases with increasing temperature [35]. This calls into question the proposal that RuO_2 films behave like *n*-type semi-conductors.

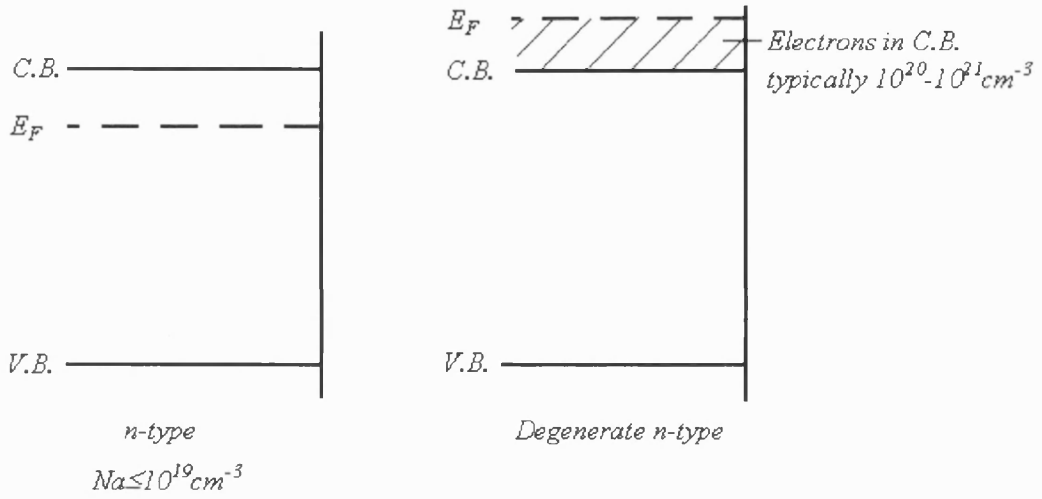

Figure 1.6 : Semiconductor model of RuO_2 anodes (N_d=electron density)

Compact RuO_2 films have shown conductivity as high as 10^3-10^4 ohm^{-1} cm^{-1} [37]. The formation of highly conducting single crystals of RuO_2 at RuO_2 films has also been confirmed by SEM at high annealing temperatures, during the thermal decomposition process [31]. These observations suggest that increasing conductivity with annealing temperature is related to the morphology of RuO_2 films. It can be said that RuO_2 films are primarily metallic conductors. However, the presence of pores, cracks, grain boundaries and phase changes in the film could reduce the metallic behaviour associated with RuO_2. Distortion of the crystal lattice possibly due to the presence of structural defects i.e. residual chlorine [32,37] could also effect the overlap of *d*-orbitals

responsible for metallic conduction, and hence the conductivity observed.

1.5.3 capacitive behaviour

The charging process which occurs at RuO_2-based anodes during potential cycling has also attracted a great deal of attention. A typical cyclic voltammogram of an RuO_2 anode, together with that of an RTO anode is shown in **Figure 1.7**.

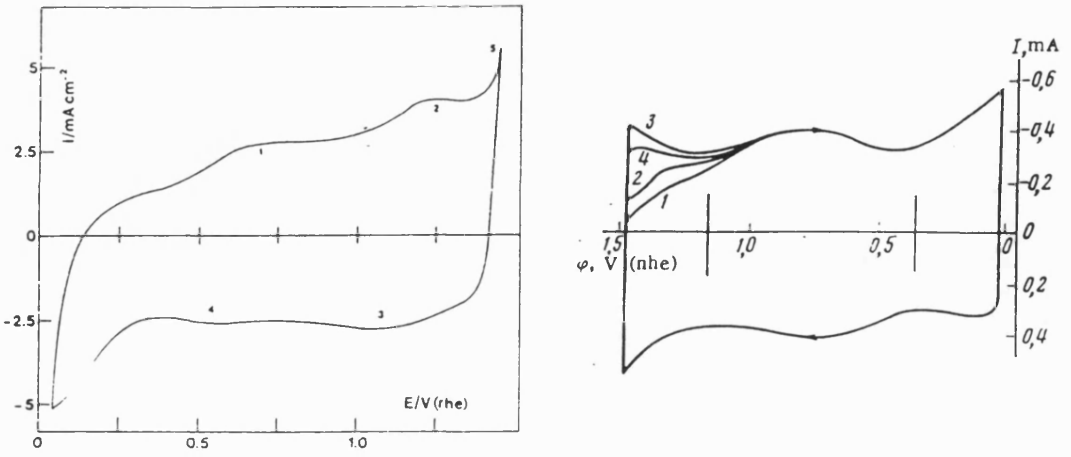

RuO_2 anode RTO anode

Figure 1.7 : Cyclic voltammograms of RuO_2 (1M $HClO_4$, v=60mVs^{-1}) [26] and 30 % RTO anodes (1N H_2SO_4, v=130mVs^{-1}) [50].

The charge observed during electrochemical cycling of RuO_2-based films is associated with Faradaic processes, as opposed to simply double-layer charging. It is injected over a large potential range which results in the characteristic broad, featureless cyclic voltammograms shown.

By definition, the relationship between charge Q and current density j is given as :

$$j = \frac{dQ}{dt} = \frac{dQ}{dE} \cdot \frac{dE}{dt} = \frac{dQ}{dE} \cdot v \qquad (1.10)$$

where v=sweep-rate (V s^{-1}) and dE corresponds to the potential range of the charge measured. The resultant capacitance of the film is referred to as a pseudocapacitance C_p. Since by definition, $Q=CV$, it follows that $C_p = \frac{dQ}{dE}$ and hence :

$$j = C_p v \tag{1.11}$$

Using the above relationships, it is therefore possible to evaluate the pseudocapacitance of RuO_2-based films from their cyclic voltammetric behaviour.

The exact nature of the redox process which results in the charge appears to be uncertain. Trasatti *et al.*, [26,38,39,45] have proposed that the voltammetric charge is due to the oxidation of non-stoichiometric Ru^{3+}, which is accompanied by diffusion of protons [46,47] into the bulk of the film. They proposed the following mechanism.

$$RuO_2 + xe^- + xH^+ \rightarrow RuO_{2-x}(OH)_x \tag{1.12}$$

In contrast to this work, the voltammetric charge has been attributed to interfacial charging processes, as opposed to bulk oxide processes [48,49]. Possible redox couples involved in the interfacial charging processes are OH_{ads}/H_2O, O_{ads}/OH_{ads}, and / or Ru^{3+}/Ru^{4+}. However, the use of cyclic voltammetry as a technique for the identification of redox processes, whether bulk or interfacial process, must be treated as purely speculative since no direct spectroscopic identification of the species is possible.

These conflicting views can be attributed to the definition of Q. Charge values reported are generally normalised to unit area and defined as charge density Q_d with units C cm^{-2}. As a result, the surface area of the anode film must be taken into account.

RuO_2-based films are highly porous with large surface areas [48]. The previous assumption that the voltammetric charging is a bulk process was based on the geometric surface area of the anode. Re-evaluation of Q, using the true surface area values from BET analysis, led to a typical value of Q=500mC cm^{-2} for a four layer RuO_2 film, annealed at 350°C. This value was equivalent to a surface redox process. A linear relationship between Q and the true surface area of the anode A was established. This indicates that the redox process associated with the charge is directly related to the true surface area of the anode. A similar relationship was found for RTO anode films [50]. This result stresses the importance of taking the true surface area of an anode into account when considering the electrochemical behaviour of RuO_2-based films.

It is clear from the above discussion that morphology and electrical and physical properties of the electrode play important roles in the interpretation of the electrochemistry of the anode under study, and also the electrocatalytic performance. **Figure 1.8** is an example of how changes in structure as a function of RuO_2 mole % are linked to changes in electrical, physical and electrochemical properties [44]. As the RuO_2 mole % increases from 0 to ~30 mole %, changes in the structure of the mixed oxide i.e. the ratio of rutile phase : anatase phase, are accompanied by a changes in electrochemical properties (capacity, potentials, O_2 and Cl_2 evolution currents at constant potential) of the anode. At >30-40 mole %, very little change in all the film properties is observed. The same author reports a similar change in conductivity at ~30 mole % (see Section 1.5.2). As well as establishing a link between structure and electrical, physical and electrochemical properties, the above results also support the viewpoint that RTO anode of *ca.* 30-40 mole % RuO_2 possess the optimum properties for Cl_2 evolution.

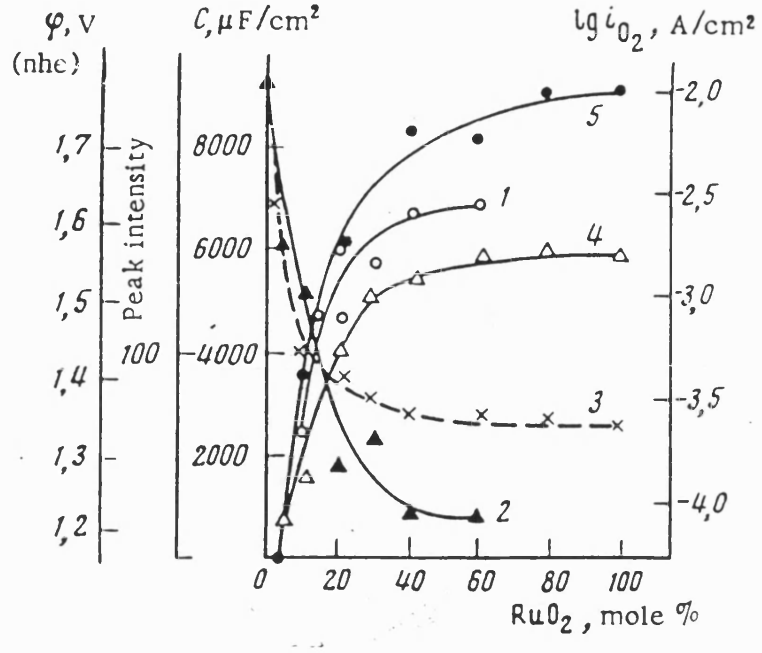

Figure 1.8 : The effect of RuO_2 concentration in RTO anode films on 1) the concentration of rutile phase, 2) concentration of anatase phase, 3) anode potential at CD=0.1A/cm^2 in 5N NaCl, 4) capacitance C (μF cm^{-2}) at E=0.45V and 120Hz and 5) C.D. of O_2-evolution at E=1.34V [44].

1.6 Kinetic and Mechanistic Studies

1.6.1 Electrode kinetics : A background discussion

As previously discussed in Section 1.2, electrocatalytic activity is directly related to overpotential η. The relationship between overpotential and current density is represented by the Butler-Volmer equation as follows :

$$j = j_0\left[exp\left(\frac{a_A nF}{RT}\eta\right) - exp\left(\frac{-\alpha_C nF}{RT}\eta\right)\right] \qquad (1.13)$$

where α_A and α_C correspond to the transfer coefficients at the anode and cathode respectively, with $\alpha_A + \alpha_C = 1$, j is the experimental current density at the potential E, and j_o is the exchange current density at equilibrium potential E_e. Eq. (1.13) has two limiting cases. Firstly, when η is large and negative, the first term in the Butler-Volmer equation becomes negligible compared with the second giving :

$$-j = j_0 \exp\left(-\frac{\alpha_C nF}{RT}\eta\right) \Leftrightarrow \log(-j) = \log j_0 - \frac{\alpha_C nF}{2.3RT}\eta \qquad (1.14)$$

which is referred to as the cathodic Tafel equation. Likewise, when η becomes large and positive, the anodic Tafel equation is defined as :

$$\log j = \log j_0 + \frac{\alpha_A nF}{2.3RT}\eta \qquad (1.15)$$

Eq. (1.14) and Eq. (1.15) only apply if η>~52mV where the current I, increases exponentially with overpotential η. As a result, a plot of log j *vs.* η enables kinetic information such as j_o, α_A and α_C to be evaluated from the gradient and intercept. The gradient of this plot is referred to as the Tafel slope. **Figure 1.9** illustrates how these kinetic parameters can be evaluated from Tafel plots.

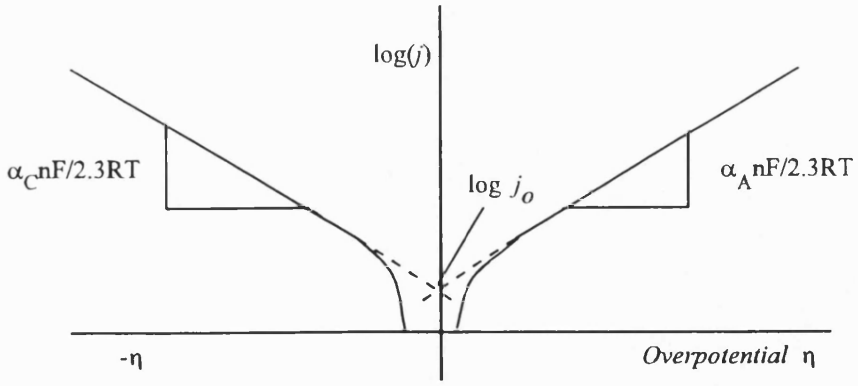

Figure 1.9 : Tafel plots for anodic and cathodic Tafel equations.

1.6.2 Kinetic and mechanistic studies of chlorine evolution

Electrochemical studies on the kinetics and mechanisms of Cl_2 and O_2 evolution at RuO_2-based anodes have been carried out mainly at RuO_2 and RTO anodes [52-63]. It has generally been considered that Cl_2 evolution could follow two mechanisms, namely the Volmer-Heyrowsky and the Volmer-Tafel mechanism [61]. In the Volmer-Heyrowsky mechanism, Cl_2 is evolved by the electrochemical desorption of an adsorbed chlorine atom with a chloride ion in solution as shown below. The Heyrowsky reaction is the rate-determining step.

Mechanism 1 : Volmer-Heyrowsky mechanism

The Volmer reaction $\quad Cl \rightleftharpoons Cl_{ad} + e^- \quad (1.16)$

The Heyrowsky reaction $\quad Cl^- + Cl_{ad} \rightarrow Cl_2 + e^- \text{ (RDS)} \quad (1.17)$

The Volmer-Tafel mechanism involves a recombination-desorption process where two adsorbed chlorine atoms recombine at the electrode surface and then desorb. This is referred to as the Tafel reaction and is rate-determining.

Mechanism 2 : Volmer -Tafel mechanism

The Volmer reaction $\quad Cl^- \rightleftharpoons Cl_{ad} + e^- \quad (1.18)$

The Tafel reaction $\quad 2Cl_{ad} \rightarrow Cl_2 \text{ (RDS)} \quad (1.19)$

However, neither reaction scheme takes the state of the electrocatalytic surface component into consideration. It is considered that Ru acts as the electrocatalytic site

during Cl_2 evolution [62,63]. A further mechanism has been proposed which introduces the oxidation state of the Ru surface into the reaction scheme and this is illustrated in mechanism 3.

Mechanism 3 : Krishtalik mechanism [62]

$$Ru(n) + Cl^- \rightleftharpoons Ru(n)Cl + e^- \quad (1.20)$$

$$Ru(n)Cl \rightarrow Ru(n+1)Cl + e^- \quad (1.21)$$

$$Ru(n+1)Cl + Cl^- \rightleftharpoons Ru(n) + Cl_2 \quad (1.22)$$

A theoretical relationship between exchange current density j_o, overpotential η, and degree of coverage θ of the anode with chlorine has been derived [64], which has led to the evaluation of theoretical Tafel slope values for the different proposed reaction mechanisms. As a result, evaluation of the experimental Tafel slope has been used to elucidate the reaction mechanism for Cl_2 evolution.

Authors have reported Tafel slopes of generally 30-40mV. Tafel slopes of 30mV [52,53,56,59] support the Volmer-Tafel mechanism with Tafel slopes of 40mV proposed to support the Volmer-Heyrowsky mechanism [57,58,60,62,63]. In contrast to the above, Tafel slopes of 108mV have also been reported [43]. The conflicting theories and the fact that the role of the electrocatalytic site has not been considered, suggests that the elucidation of the reaction mechanism directly from the Tafel slope alone is premature.

1.6.3 Kinetic and mechanistic studies of oxygen evolution

Several mechanisms have been proposed for the O_2 evolution process. A general mechanism proposed by Iwakura *et al.*, [65] is as follows.

$$S + H_2O \rightleftharpoons SOH + H^+ + e^- \text{ where S=site at electrode surface} \quad (1.23)$$

$$2SOH \rightleftharpoons SO + S + H_2O \quad (1.24)$$

$$2SO \rightleftharpoons 2S + O_2 \quad (1.25)$$

In contrast to the mechanism discussed above, other authors have proposed mechanisms for O_2 evolution which incorporate the role of ruthenium [47,66,67]. These mechanisms are based on the electrochemical properties of ruthenium, and an example is shown below for RuO_2 in acid media.

$$RuO_2 + H_2O \rightleftharpoons RuO_3 + 2H^+ + 2e^- \quad (1.26)$$

$$RuO_3 \rightleftharpoons RuO_2 + O_{ads} \quad (1.27)$$

$$2O_{ads} \rightleftharpoons O_2 \quad (1.28)$$

$$O_{ads} + OH_{ads} \rightleftharpoons O_2 + H^+ + e^- \quad (1.29)$$

It is generally accepted that adsorbed intermediates such as OH, O and O_2H could be involved in the reaction mechanism. However, the exact process is still far from certain.

1.7 Surface Characterisation Studies

Despite the electrochemical studies into understanding the performance of DSAs® during O_2 or Cl_2 evolution, there has been a lack of research concerning the role of ruthenium during gas evolution. Surface characterisation techniques which incorporate both *ex-situ* and *in-situ* spectroscopy have been directed at identifying the oxidation state(s) of ruthenium surfaces formed during O_2 or Cl_2 evolution.

1.7.1 *Ex-situ* spectroscopic techniques

X-ray photoelectron spectroscopy (XPS) has been used to study the changes in oxidation state and chemical composition of Ru-based anodes during O_2 and Cl_2 evolution, in order to characterise the anode surface [68,71]. Spectra for each anode have generally been obtained before and after electrolysis in order to observe any changes in composition of the anodes as a result of polarisation.

RuO_3 [Ru(VI)] has been identified in fresh, thermally prepared RuO_2 and RTO anodes using XPS [68]. This is in support of previous work by Kim and Winograd [72] who studied the surface chemistry of a series of Ru-oxy compounds and identified RuO_3 in RuO_2 powder and also single crystal. The Cl 2p spectra for RuO_2 identified the presence of two different chlorine species, chloride ions in the RuO_2 lattice and adsorbed atomic chlorine. The Cl 2p spectrum of freshly prepared RTO showed the presence of only one chlorine species, that of chloride ions in the RTO lattice. The XPS spectra of the anodes following electrolysis in 4M NaCl revealed no change in the composition of the film with regard to the Ru(IV) : Ru(VI) and Ru : Ti ratios. The residual chloride in RuO_2 and RTO anodes was found to be equal which indicates that the degree of chlorine doping in the films is dependent on annealing temperature and not on Ru content. The same author used X-ray diffraction (XRD) to study RTO mixed oxide anodes with Ru~22 mole %. XRD indicated that the anode film was a solid-solution of the two oxides, RuO_2 and TiO_2.

XPS studies of the O_2-evolution mechanism at sputtered Ru metal anodes and thermally prepared RuO_2 anodes by Kötz *et al.* [69,70], have led to the proposal that O_2 evolution is accompanied by corrosion of the anode. **Figure 1.10** illustrates the proposed mechanism. At Ru anodes, an hydrated oxide film has been identified at the

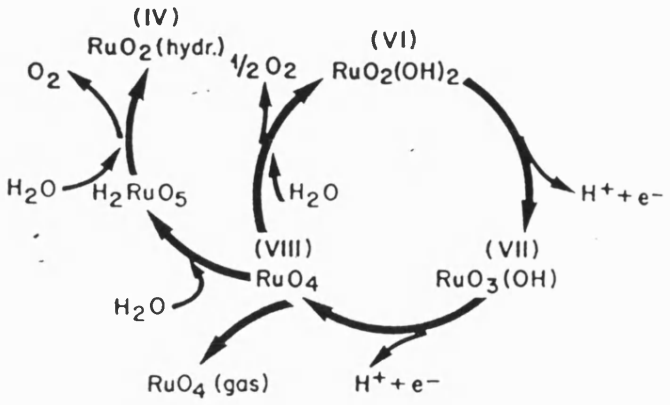

Figure 1.10 : Model for O_2 evolution and corrosion at Ru / RuO_2 anodes [69].

surface during O_2 evolution which supports the proposal by Iwakura *et al.* [65] that corrosion of Ru via RuO_4 results in the formation of $RuO_2.xH_2O$ at the surface. No higher stable oxide was identified. The identification of Ru(VI) at the surface of RuO_2 anodes [68-70] has led Kötz *et al.* [69] to propose that O_2 evolution proceeds via a two electron step from Ru(VI), in the form of an oxide or hydroxide to give Ru(VIII), as RuO_4. Two routes are then possible. Firstly, RuO_4 corrodes as either a gas, RuO_4 or soluble species, H_2RuO_5. A further reaction with H_2O results in O_2 evolution and formation of an hydrated oxide film of stoichiometry between RuO_2 and $RuO_2.xH_2O$. Secondly, RuO_4 can dissociate into oxygen and Ru(VI). It is proposed that the stability of Ru(VI) in the films determines the route taken. In the case of Ru metal, no identification of Ru(VI) was possible, which suggests that this higher oxidised species has a low stability on Ru metal anodes. As a result, they propose that the first route is more favourable for Ru anode, which results in corrosion of the Ru anode at a much faster rate than RuO_2.

As a result of these findings, it has been speculated that RuO_3 may be responsible for the excellent stability of RuO_2-based anodes during Cl_2 or O_2 evolution. However,

surface studies such as XPS and Auger electron spectroscopy are not completely reliable due to the fact that analysis occurs outside the electrochemical cell and at high vacuum. The use of high vacuum techniques is problematic due to the possible change in surface composition during transport from the cell to the high vacuum conditions of XPS as a result of air oxidation and adsorption processes. To eliminate these uncertainties, *in-situ* spectroelectrochemical techniques have been developed which combine spectroscopic analysis directly with electrochemical studies.

1.7.2 *In-situ* spectroscopic techniques

In-situ differential spectroscopy, surface-normalised interfacial fourier transform-IR spectroscopy, (SNFTIRS) and on-line mass spectrometry have led to the identification of various corrosion products formed at Ru and RuO_2 anodes during O_2 evolution [73-75]. RuO_4 has been identified as the main corrosion product during O_2 evolution in acid media using differential reflectance spectroscopy [73]. In this study the reflectance R was recorded at two different potentials, 1.40V and -0.1V *vs.* RHE and a difference spectrum calculated as a function of wavelength i.e. $[R(1.40V)-R(-0.1V)]/R(-0.1V)]$. The formation of RuO_4 as a volatile corrosion product has also been confirmed by on line mass spectrometry [75].

SNIFTIRS has been used to study O_2 evolution at Ru anodes in both acid and alkali media [74]. RuO_4 was again identified at 1.40V *vs.* RHE in acid media. No other bands were observed in the potential range of -0.00 to +1.40V. In alkali media, a peak was observed between 1.25V and 1.30V *vs.* RHE which could correspond to perruthenate(VII), RuO_4^-, but full identification of this peak was not possible due to a lack of IR data of this ruthenium-oxy species. The RuO_4^- anion was identified both on

the electrode surface and also in solution by the use of *s* and *p*-polarised light. No other peaks were observed at lower potentials.

No *in-situ* studies regarding the Cl_2 evolution mechanism at RuO_2-based anodes have been reported.

1.8 Potential-Modulated Reflectance Spectroscopy

Understanding of the mechanism of O_2 and Cl_2 evolution at RuO_2-based anodes is still far from complete. The use of *ex-situ* techniques such as XPS introduce uncertainties due to the possible modification of the surface during transport between the electrochemical cell and the high vacuum conditions. *In-situ* spectroscopic techniques have proved more attractive and enable identification of Ru-oxy species formed during O_2 evolution at Ru anodes. The aim of this thesis is to demonstrate how the technique of potential modulated reflectance spectroscopy (PMRS) [76] can be applied to the study of RuO_2-based anodes.

The theory and applications of PMRS are presented. As a result, it is demonstrated how quantitative spectroscopic and kinetic information can be derived for an electrochemical process. A model solution redox system, the ferro-ferricyanide redox couple is studied to model the responses of PMRS for a diffusion-controlled process.

An electrodeposited Ru metal film has been chosen as a model RuO_2-based anode for the study of the O_2 evolution mechanism. PMRS results in both acid and alkali media are presented. Finally, the anodic behaviour of the mixed alloy anode, Ru-Ir is investigated using PMRS in alkali media. The stabilising effect of Ir is discussed.

References

1. DSA is a registered trade-mark of Diamond Shamrock
2. S. Trasatti and W.O'Grady, "*Properties and Applications of RuO_2-based Electrodes. Advances in Electrochemistry and Electrochemical Engineering*" Vol.12, Wiley-Interscience, New York (1982)
3. D. Pletcher and F.C. Walsh, "*Industrial Electrochemistry*", 2nd edition, Chapman & Hall, London (1990), p.174
4. W.N. Brooks, *Chemistry in Britain*, December, 1095 (1986)
5. H.B. Beer, *J. Electrochem. Soc.*, **127**(8), 303 (1980)
6. S. Trasatti, *Electrochimica Acta*, **29**(11), 1503 (1984)
7. S. Trasatti, *Electrochimica Acta*, **36**(2), 225 (1991)
8. S. Trasatti, *Electrochimica Acta*, **32**(3), 369 (1987)
9. P.C.S. Hayfield, *Platinum Metals Rev.*, **42**(1), 27 (1998)
10. G. Faita, G. Fiori and J.W. Augustynski, *J. Electrochem. Soc.*, **116**(7), 928 (1969)
11. R.T. Atanasoski, B. Ž. Nikolic, M.M. Jakšic and A.R. Despic., *J. Appl. Electrochem.*, **5**, 155 (1975)
12. H.B. Beer, *British Patent No.* 1,147,442; (1965)
13. H.B. Beer, *British Patent No.* 1,195,871; (1967)
14. Ch. Comninellis and G.P. Vercesi, *J. Appl. Electrochem.*, **21**, 335 (1991)
15. C. Iwakura and K. Sakamoto, *J. Electrochem. Soc.*, **132**(10), 2420 (1985)
16. R. Kötz and S. Stucki, *Electrochimica Acta*, **31**(10), 1311 (1986)
17 J.F.C. Boodts and S. Trasatti, *J. Electrochem. Soc.*, **137**(12), 3784 (1990)
18. A.I. Onuchukwu and S. Trasatti, *J. Appl. Electrochem.*, **21**, 858 (1991)
19. Shih-Min Lin and Ten-Chin Wen, *J. Electrochem. Soc.*, **140**(8), 2265 (1993)
20. D.T. Shieh and B.J. Hwang, *Electrochimica Acta*, **38**(15), 2239 (1993)

21. R. Hutchings, K. Müller, R. Kötz and S. Stucki., *J. Mater. Sci.*, **19**, 3987 (1984)

22. T.A.F. Lassali, J.F. C. Boodts and S. Trasatti., *Electrochimica Acta*, **39**(11-12), 1545 (1994)

23. L.A. De Faria, J.F. C. Boodts and S. Trasatti., *Electrochimica Acta*, **37**(13), 2511 (1992)

24. A. Cornell and D. Simonsson, *J. Electrochem. Soc.*, **140**(11), 3123 (1993)

25. R. Kötz and S. Stucki, *J. Appl. Electrochem.*, **17**, 1190 (1987)

26. S. Trasatti and G Buzzanca, *J. Electroanal. Chem.*, **29**, App.1-5 (1971)

27. D.B. Rogers, R.D. Shannon, A.W. Sleight and J.L. Gillson, *Inorg. Chem.*, **8**(4), 841 (1969)

28. F.A. Cotton and J.T. Mague, *Inorg. Chem.*, **5**(2), 317 (1966)

29. I.E. Veselovskaya, E.K. Spasskaya, V.A. Sokolov, V.I. Tkachenko and L.M. Yakimenko, *Soviet Electrochem.*, **10**(1), 62 (1974)

30. F. Hine, M. Yasuda and T. Yoshida., *J. Electrochem. Soc.*, **124**(4), 500 (1977)

31. G. Bianchi, *J.Appl. Electrochem.*, **1**, 231 (1971)

32. P.H. Duvigneaud and A. Coussement, *J. Solid State Chemistry*, **52**, 22 (1984)

33. K. Kameyama, K. Tsukada, K. Yahikozawa and Y. Takasu, *J. Electrochem. Soc.*, **140**(4), 966 (1993)

34. V. Birss, R. Myers, H. Angerstein-Kozlowska and B.E. Conway, *J. Electrochem. Soc.*, **131**(7), 1502 (1984)

35. G. Lodi, *Mater. Chem.*, **1**, 77 (1976)

36. C. Iwakura, H. Tada and H. Tamura, *Electrochimica Acta*, **22**, 217 (1977)

37. S. Pizzini, G. Buzzanca, C. Mari, L. Rossi and S. Torchio, *Mater. Res. Bull.*, **7**, 449 (1972)

38. D. Galizzioli, F. Tantardini and S. Trasatti., *J. Appl. Electrochem.*, **4**, 57 (1974)

39. D. Galizzioli, F. Tantardini and S. Trasatti., *J. Appl. Electrochem.*, **5**, 203 (1975)

40. W.D. Ryden, A.W. Lawson, and C.C. Sartain, *Phys. Lett.*, **26A**(5), 209 (1968)

41. S.M. Marcus, *Phys. Lett.*, **28A**(3), 191 (1968)

42. D.C. Cronomeyer, *Phys. Rev.*, **87**, 876 (1952)

43. A.T. Kuhn and C.J. Mortimer, *J. Electrochem. Soc.*, **120**(2), 231 (1972)

44. E.K. Spasskaya,Yu.B. Makarychev, A.A. Yakovleva and L.M. Yakimenko, *Soviet Electrochem.*, **13**(3), 279 (1977)

45. S. Trasatti, *J. Electrochem. Soc.*, **120**, 1703 (1973)

46. T. Arikado, C. Iwakura and H. Tamura, *Electrochimica Acta*, **22**, 513 (1977)

47. K. Doblhofer, M. Metikoš, Z. Ogumi and H. Gerischer, *Ber. Bunsenges Phys. Chem.*, **82**, 1046 (1978)

48. L.D. Burke, O.J. Murphy and J.F. O'Neill, *J. Electroanal. Chem.*, **81**, 391 (1977)

49. L.D. Burke, O. J. Murphy, J.F. O'Neill and S. Venkatesan, *J. Chem. Soc., F.T 1*, **73**, 1659 (1977)

50. D.V. Kokoulina, T.V. Ivanova, Yu.I. Krasovitskaya, Z.I. Kudryavtseva and L.I. Krishtalik, *Soviet. Electrochem.*, **13**(10), 1293 (1977)

51. A.J. Bard and L.R. Faulkner in "Electrochemical Methods : Fundamentals & Applications" Wiley & Sons (1980)

52. G. Faita and G. Fiori, *J. Appl. Electrochem.*, **2,** 31 (1972)

53. R.G. Érenburg, L.I. Krishtalik and V.I. Bystrov, *Soviet. Electrochem.*, **8**(12), 1690 (1972)

54. R.G. Érenburg, L.I. Krishtalik and I.P. Yaroshevskaya, *Soviet Electrochem.*, **11**(7), 989 (1975)

55. R.G. Érenburg, L.I. Krishtalik and I.P. Yaroshevskaya, *Soviet Electrochem.*, **11**(7), 993 (1975)

56. R.G. Érenburg, L.I. Krishtalik and I.P. Yaroshevskaya, *Soviet Electrochem.*, **11**(8), 1150 (1975)

57. L.J.J. Janssen, L.M.C. Starmans, J.G. Visser and E. Barendrecht, *Electrochimica. Acta*, **22**, 1093 (1977)

58. I.R. Burrows, D.A. Denton and J.A. Harrison, *Electrochimica Acta*, **23**, 493 (1978)

59. I.R. Burrows, J.H. Entwistle and J.A. Harrison, *J. Electroanal. Chem.*, **77**, 21 (1977)

60. D.A. Denton, J.A. Harrison and R.I. Knowles, *Electrochimica Acta*, **24**, 521 (1979)

61. L.J.J. Janssen, "Modern Chlor-Alkali Technology" Vol. 12 (1982), C. Jackson Ed. Ellis Howard Chichester 1983

62. L.I. Krishtalik, *Electrochimica. Acta*, **26**, 329 (1981)

63. T. Arikado, C. Iwakura and H. Tamura, *Electrochimica Acta*, **23**, 9 (1978)

64. L.J.J. Janssen and J.G. Hoogland, *Electrochimica Acta*, **15**, 941 (1970)

65. C. Iwakura, K. Hirao and H. Tamura, *Electrochimica Acta*, **2**, 329 (1977)

66. L.D. Burke, O. J. Murphy, J.F. O'Neill and S. Venkatesan, *J. Chem. Soc., F.T. 1*, **73**, 1659 (1977)

67. M.E.G. Lyons and L.D. Burke, *J. Chem. Soc., F.T. 1*, **83**, 299 (1987)

68. J. Augustynski, L. Balsenc and J. Hinden, *J. Electrochem. Soc.*, **125**, 1093 (1978)

69. R. Kötz, H.J. Lewerenz and S. Stucki, *J. Electrochem. Soc.*, **130**, 825 (1983)

70. R. Kötz, H.J. Lewerenz, P. Brüesch and S. Stucki, *J. Electroanal. Chem.*, **150**, 209 (1983)

71. M. Vukovic, T. Valla and M. Milan, *J. Electroanal. Chem.*, **356**, 81 (1993)

72. K.W. Kim and N. Winograd, *J. Catalysis*, **35**, 66 (1974)

73. R. Kötz, S. Stucki, D. Scherson and D.M. Kolb, *J. Electroanal. Chem.*, **172**, 211 (1984)

74. A. Bewick, C. Gutiérrez and G. Larramona, *J. Electroanal. Chem.*, **332**, 155 (1992)

75. M. Wohlfahrt-Mehrens and J. Heitbaum, *J. Electroanal. Chem.*, **237**, 251 (1987)

76. see e.g. *Spectroscopic and Diffraction techniques in Interfacial Electrochemistry*, Editors C. Gutiérrez and C. Melendres. p.223. Kluwer (1990)

Chapter 2

Chapter 2

Potential Modulated Reflectance Spectroscopy : An Introduction

2.1 Introduction

Potential Modulated Reflectance Spectroscopy (PMRS) [1] is an optical modulation technique that enables the electrode-electrolyte interface to be studied in the *UV-Visible* region *in-situ.* Optical modulation techniques involving reflectance at an electrode surface have proved to be very powerful techniques for the study of physical properties of both metals and semi-conductors. Electrolyte Electro-Reflectance (EER) spectroscopy was developed in the 1960s and applied mainly to the study of semi-conductors [2]. The electro-reflectance effect involves changing the optical properties of the solid by modulation of the electric field. EER spectra provide information about the electronic properties of the system i.e. bandgap energy, defects and crystallinity. In EER, no electrochemical reactions are associated with the EER response. By contrast PMRS, which was developed directly from EER, is generally used to study systems where electrochemistry occurs.

PMRS was first used as a spectroelectrochemical technique by Bewick *et al.* [3] in 1970 for the study of change in reflectivity of a platinum electrode. Here, electrochemical information regarding surface oxide layer formation and adsorption of hydrogen on platinum was derived from the modulated reflectance response. Since then, this powerful modulation technique has been increasingly employed in electrochemical studies, most notably of the passivation of metal electrodes [4-7], the identification of intermediates in electrochemical reactions [8] and the study of adsorption species at

electrode surfaces [9-11]. Several other terms have been coined to describe the PMRS technique including "Electrochemical Modulation Spectroscopy" (ECMS) [10,12], "Modulated Specular Reflectance Spectroscopy" (MSRS) [3,8] and "Sinusoidally Modulated AC Reflectance Spectroscopy" (SMACRS) [13]. The basic principles behind all these *in-situ* techniques are the same.

Small synchronous changes in the optical properties of the electrode-electrolyte interface that arise from modulation of the electrode potential by a sine or square wave of known amplitude and frequency of modulation, can be measured as a function of a range of variables i.e. wavelength λ, potential E, and frequency ω. The optical properties of the interfacial region may be changed generally in one of two ways [1]. In many electrochemical systems, the optical properties of the interface are perturbed as a consequence of Faradaic reactions, involving either a surface layer or soluble species, provided the species involved absorb light in the selected wavelength region. However, the optical properties of the interfacial region can also be changed by an electroreflectance effect without a reaction taking place. The electrolyte electroreflectance effect (EER) arises from modulation of the dielectric constant of the substrate by the applied electric field, and EER spectra of single crystal semiconductors and of semiconducting layers such as anodic oxides exhibit well defined structures at the bandgap energy [14]. It will be shown in Section 2.4 that it is possible to distinguish between electroreflectance effects and optical changes due to Faradaic reactions by studying the frequency dependence of the optical response. Since the change in absorbance due to Faradaic processes is proportional to the charge passed, the modulated reflectance signal attenuates with increasing frequency. By contrast, electroreflectance effects usually persist to high frequencies. In this work, EER effects were found to be unimportant.

Figure 2.1 illustrates the experimental arrangement used for PMRS measurements. A monochromatic *UV-Visible* light beam is focused onto the electrode surface and an *ac* sinusoidal signal is superimposed onto the *dc* electrode potential. The electrode is therefore modulated between the potentials E_2 and E_1, centred on the mean *dc* potential E_{dc}. Provided that the potential modulation perturbs an electrochemical process, a periodic change in concentration and / or oxidation state of the species involved in the Faradaic process takes place at the same frequency as the *ac* potential modulation. This leads to an oscillation of the intensity of reflected light between two limiting values I_2 and I_1, provided that one or more of the species involved in the Faradaic process absorbs light at the selected wavelength λ. A phase shift ϕ exists between the potential modulation applied and the modulated *ac* current response due to the Faradaic process. **Figure 2.2** illustrates the relationship between the potential modulation and the *ac* current response observed. Since the *ac* current response is directly related to the intensity of light, the relationship between potential modulation and the resultant change in intensity of the light is also illustrated. It should be noted that a positive change in potential does not necessarily result in a positive change in intensity of light, but is dependent on the redox system under study (refer to Section 2.3 for details of sign convention).

The reflected periodic light signal is detected by a photodiode, which is connected to a lock-in amplifier. The current signal from the photodiode is amplified and converted to voltage via a photodiode amplifier. Hence, the signal received and recorded by the lock-in amplifier is directly proportional to the intensity of light I. A lock-in amplifier records the change in light intensity ΔI, as a result of the potential modulation. ΔI does not however correspond to I_2-I_1 as expected, but is directly related to the difference in intensity of light at E_2 and E_{dc} i.e. I_2-I, where I corresponds to the intensity of the

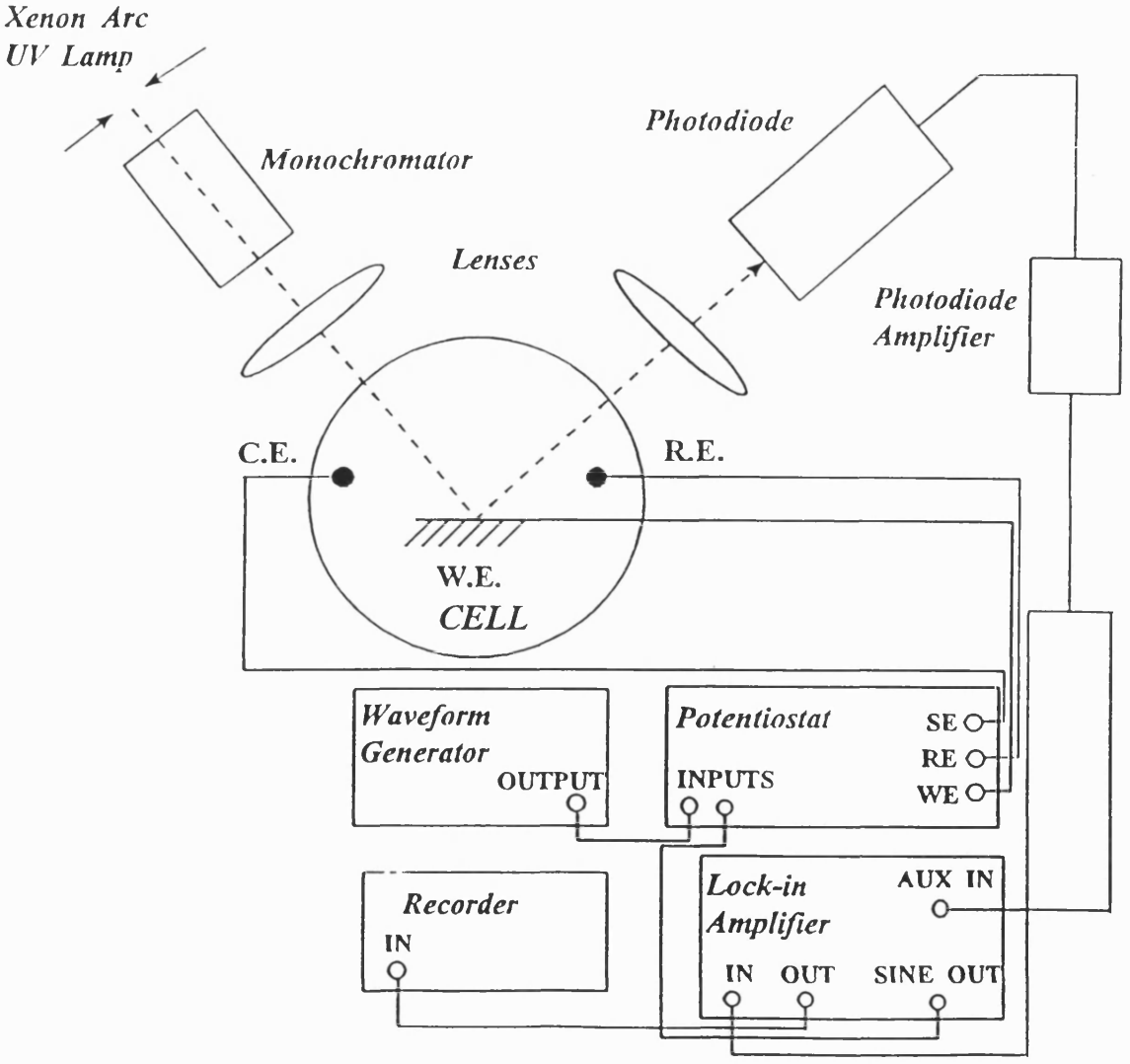

Figure 2.1 : A schematic diagram of the PMR apparatus.

reflected light at *dc* potential. This is due to the phase sensitive detection technique of the lock-in amplifier. Normalisation of the modulated signal leads to the following expression :

$$\frac{\Delta I}{I} = \frac{I_2 - I}{I} = \frac{I_2/I_o - I/I_o}{I/I_o} = \frac{R_2 - R}{R} = \frac{\Delta R}{R} \qquad (2.1)$$

where R_2=reflectance at potential E_2

R=reflectance at the mean *dc* potential, E_{dc}

I_o=intensity of incident light beam

Normalisation is necessary in order to compensate for the wavelength dependence of the incident lamp intensity and to allow for changes in surface reflectivity that may occur during the electrochemical process. Normalisation is performed by the lock-in amplifier which measures both the *dc* and *ac* signals from the photodiode output and computes the ratio of the two. The resultant $\Delta R/R$ signal is termed the optical response of the system under study. Throughout the remainder of the thesis the *ac* reflectance signal will be referred to in this way.

The periodically modulated potential is produced by the superposition of an *ac* sinusoidal potential, produced by the lock-in amplifier, on a *dc* potential signal produced by the potentiostat. The optical response has the same frequency as the *ac* potential modulation and the lock-in amplifier only records the signal produced at this frequency, thus eliminating any background signals due to noise. The *ac* nature of the optical response enables $\Delta R/R$ to be represented in the complex plane. **Figure 2.3** illustrates the relationship between the different components of the optical response using complex

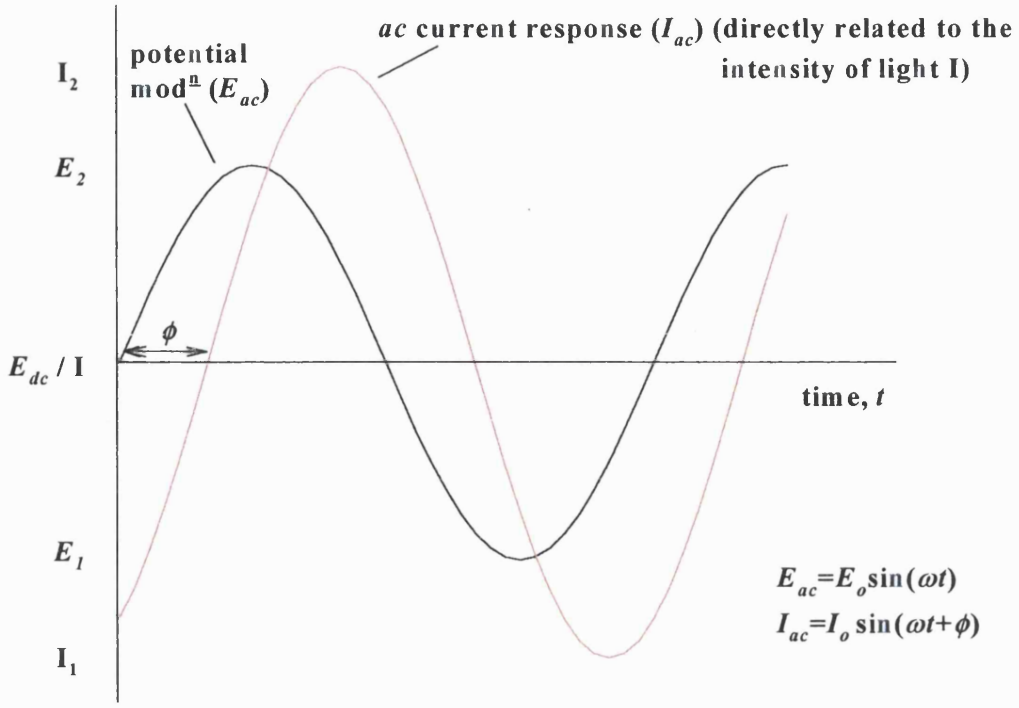

Figure 2.2 : The relationship between potential modulation and the resultant change in light intensity / *ac* current response. Potential modulation and *ac* current response are not to scale.

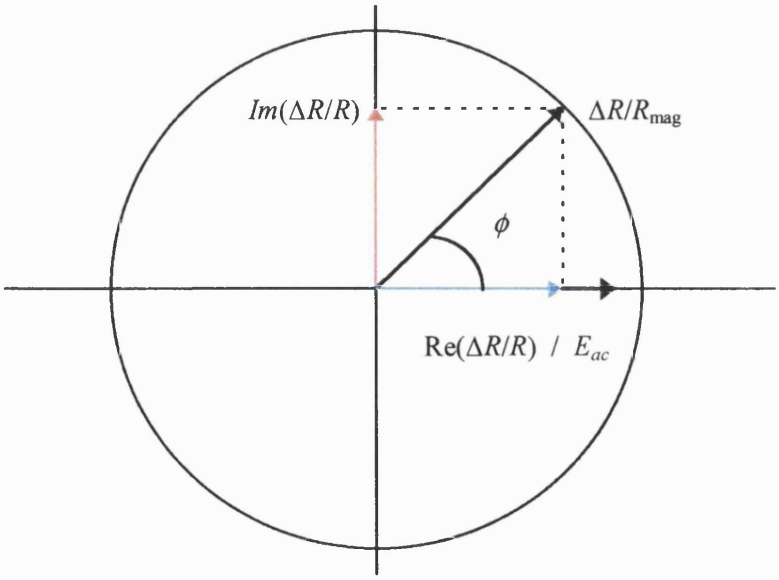

Figure 2.3 : Complex plane analysis of the optical response.

plane analysis. The lock-in amplifier can record the 0° in phase (real) and 90° out of phase (imaginary) components of $\Delta R/R$. Alternatively, the magnitude of the optical response $\Delta R/R_{mag}$ and the phase angle ϕ are recorded. ϕ corresponds to the phase angle between the potential modulation E_{ac} and optical response $\Delta R/R_{mag}$.

The PMRS technique offers three types of measurements, as summarised in **Table 2.1**. $\Delta R/R$ can be measured as a function of i) wavelength λ, ii) potential E, or iii) frequency ω.

Analysis of the wavelength dependence of $\Delta R/R$ provides spectroscopic identification of the species involved, whereas analysis of the frequency response enables kinetic information to be obtained.

Technique	*Variable function*	*Information obtainable*
PMR Spectroscopy	Wavelength, λ	Spectroscopic identification of redox states of species
PMR Voltammetry	Potential, E	Potential dependence of Faradaic processes
Frequency Resolved PMR	Frequency, ω	Kinetic information, e.g. R_{ct}, σ Distinction between kinetic and diffusion-controlled processes

Table 2.1 : A summary of the information obtainable from PMRS.

The theory and applications of the three aspects of the PMR technique are discussed in detail in Sections 2.3-3.5. Firstly however, let us consider the origin of the

optical response and look at the relationship it has with the electrical response of the system.

2.2 PMRS : The relationship between electrical and optical response

It can be shown that the PMR response of a system is directly proportional to the concentration of the light absorbing species involved and is therefore directly related to the Faradaic current I_F of the process under study. Since I_F can be correlated to the Faradaic admittance of the system Y_F, it follows that a direct relationship exists between the optical response and impedance behaviour of the system. This second relationship will be discussed in detail in Section 2.5.

Firstly let us consider the case when light passes through a sample of an absorbing species of concentration C and thickness dx. The reduction in intensity of the light beam dI is expressed by the Beer-Lambert law :

$$d\mathrm{I} = -\mathrm{I}_0 a[C]dx \tag{2.2}$$

where α=molar absorption coefficient

I_0=intensity of incident light

I=intensity of emergent light

Since $$\frac{1}{\mathrm{I}_0}.d\mathrm{I} = d\ln\mathrm{I} \tag{2.3}$$

This leads to :

$$d\ln\mathrm{I} = -\alpha[C]dx \tag{2.4}$$

If the concentration is dependent on time t and distance x, the integrated form of Eq. (2.4) becomes

$$\int_{I_0}^{I} d\ln I = -\alpha \int_0^d C(x,t)dx \text{, which leads to :} \tag{2.5}$$

$$ln\frac{\mathrm{I}}{\mathrm{I_o}} = -\alpha \int_0^d C(x,t)dx \tag{2.6}$$

where the concentration is integrated over the optical path length d.

The absorbance $\mathcal{A}$ is defined as

$$\mathcal{A} = -\log T = -\frac{1}{2.303} ln\frac{\mathrm{I}}{\mathrm{I_0}} \tag{2.7}$$

where transmittance T, corresponds to the ratio $\frac{\mathrm{I}}{\mathrm{I_0}}$.

Let us now consider transmission spectroscopy at an electrode surface. In the case of a simple redox process, $O + ne^- \rightleftharpoons R$ at the electrode-electrolyte interface, involving a solution process with no homogeneous complications, and where only R is absorbing :

$$\mathcal{A}(\lambda,x,t) = \varepsilon_R(\lambda)\int_0^{\delta} C(x,t)dx \tag{2.8}$$

where $\varepsilon_R = \frac{\alpha}{2.303}$

δ=diffusion layer thickness at the interface

C=concentration of absorbing species at the interface

ε_R=molar extinction coefficient of species R (M^{-1} cm^{-1})

If both the oxidised and reduced species are absorbing at the wavelength of interest, Eq. (2.8) can be expressed in the form :

$$\mathcal{A}(\lambda,x,t) = \Delta\varepsilon(\lambda)\int_0^{\delta} C(x,t)dx \text{ , where } \Delta\varepsilon = \varepsilon_R - \varepsilon_O \tag{2.9}$$

In reflection spectroscopy, a correction factor is necessary to take into consideration the angle of incidence and also the fact that the light beam passes through the solution twice. This leads to the expression

$$\mathcal{A}(\lambda,x,t) = \frac{2\Delta\varepsilon(\lambda)}{\cos\theta}\int_0^{\delta} C(x,t)dx \tag{2.10}$$

For a simple redox couple described, the change in concentration over a distance x, from the electrode surface depends on the charge transferred at the interface, and is therefore related to the Faradaic component of the current I_F as follows :

$$\int_0^{\delta} C(x,t)dx = \frac{Q}{nFA} \text{ where } Q = \int_0^{t} I_F(t)dt \text{ and } Q\text{=charge transferred.}$$

$$\int_0^{\delta} C(x,t)dx = \frac{1}{nFA}\int_0^{t} I_F(t)dt \tag{2.11}$$

Substitution of Eq. (2.11) into Eq. (2.10) leads to :

$$\mathcal{A} = \left(\frac{2\Delta\varepsilon(\lambda)}{nFA\cos\theta}\right)\int_0^{t} I_F(t)dt \tag{2.12}$$

As a result of the relationship between absorbance and the incident and reflected light intensities (see Eq. (2.7)), the expression for absorbance in Eq. (2.12) can be written as

$$\frac{\mathrm{I}}{\mathrm{I}_0} = \exp\left(-\left(\frac{4.606\Delta\varepsilon}{\mathrm{nFA}\cos\theta} \right) \int_0^t I_F(t)dt \right) \tag{2.13}$$

We now need to consider the origins of the optical response in terms of the Faradaic current I_F. When an *ac* potential modulation is superimposed on the *dc* potential, the resultant Faradaic current response will also have *ac* and *dc* components. The potential applied and resultant Faradaic current response can be represented according to the following equations.

$$E = E_{dc} + E_{ac} = E_{dc} + E_o \sin(\omega t) \tag{2.14}$$

$$I_F = I_{F_{dc}} + I_{F_{ac}} = I_{F_{dc}} + I_{F_o} \sin(\omega t + \phi) \tag{2.15}$$

In PMR, it is assumed that the *dc* Faradaic current is constant within the timescale of the modulation. As a result, only the *ac* component of I_F is considered.

The expression for the optical response in Eq. (2.1) can be written as follows :

$$\frac{\Delta R}{R} = \frac{\mathrm{I}_2}{\mathrm{I}} - 1 \tag{2.16}$$

where I_2=intensity of light at E_2

I=intensity of light at E_{dc}

This leads to the following expression :

$$\frac{\Delta R}{R} = \frac{I_2}{I} - 1 = \exp\left(-\left(\frac{4.606\Delta\varepsilon}{nFA\cos\theta} \right) \int_0^t I_F(\omega t)dt \right) - 1 \qquad (2.17)$$

where I_F corresponds to the *ac* Faradaic current response, which is a function of frequency ω and time t. When the optical response is much smaller than 1, which is generally the case, the above equation can be expanded and simplified to give :

$$\frac{\Delta R}{R} = -\left(\frac{4.606\Delta\varepsilon}{nFA\cos\theta} \right) \int_0^t I_F(\omega t)dt \qquad (2.18)$$

Eq. 2.18 shows that when an electrode process is perturbed by an applied *ac* modulation, the optical transmission of the electrode-electrolyte interface alters in a way that depends on the absorption properties of the redox species ($\Delta\varepsilon(\lambda)$) and is directly proportional to the integrated *ac* Faradaic component of the current I_F, and hence charge Q. As a consequence of this integration, the optical response $\Delta R/R$ is also phase shifted by 90° relative to the Faradaic current I_F. This relationship also leads to a correlation between Faradaic admittance Y_F (and hence Faradaic impedance Z_F) and the frequency dependent optical response $\Delta R/R$. As a result, it is possible to derive kinetic information regarding the system under study. The relationship between the optical response and impedance response of a system will be discussed in detail in Section 2.4.

2.3 PMR Spectroscopy

PMRS is a spectroscopic technique where the wavelength of a *UV-Visible* monochromatic light beam is scanned and the optical response is recorded as a function of wavelength at a constant *dc* potential E_{dc}. Potential modulation occurs at the

electrode-electrolyte interface by the superposition of an *ac* potential signal at constant frequency of modulation ω and constant amplitude of modulation E_o. The PMR spectra are directly related to the absorption spectra of the species generated or removed in the electrochemical process. In fact, the spectra are determined by the difference between the absorption spectra of the species involved at the two potentials E_2 and E_1. This relationship can be seen in Eq. (2.17), where $\Delta R/R$ is directly proportional to $\Delta\varepsilon$.

Figure 2.4 illustrates schematically typical PMR spectra that can be obtained, based on their corresponding difference absorption spectra. As would be expected, a positive change in light absorption leads to a negative change in the optical response due to a decrease in reflectivity. The first PMR spectrum corresponds to a monopolar band formed as a result of electrochemical oxidation-reduction at the interface, where only one species is absorbing. In the second example, a bipolar band is formed as a result of a band shift in absorption at the different potentials. The bipolar band corresponds to modulation of the interfacial region between two species with differing λ_{max} values.

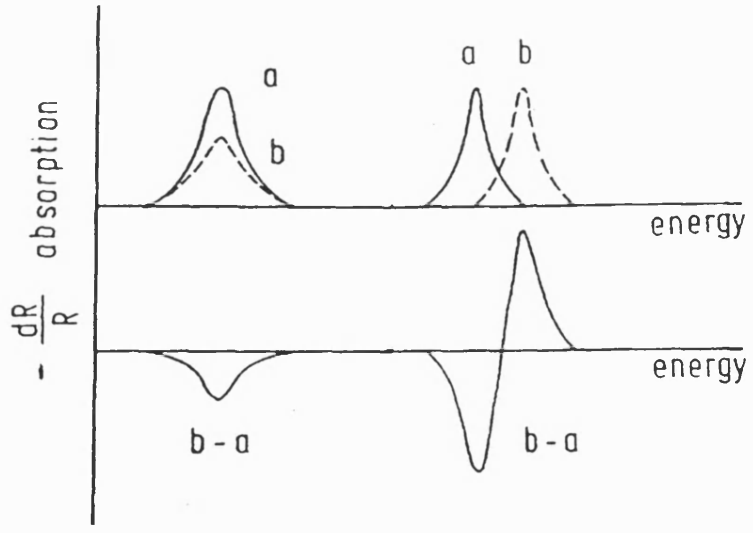

Figure 2.4 : Models of typical PMR spectra. Above : The absorption spectra at two Potentials b and a. Below : PMR spectra [1].

If the absorption spectra and extinction coefficients of possible species of interest are known, the PMR spectra can be used to identify the oxidation states and concentrations of species involved in the Faradaic process.

2.4 Frequency Response Analysis

Frequency response analysis involves studying the effect of frequency on the electrical or optical response of a system at a constant wavelength and *dc* potential. The first paper in this area was published by Adzic *et al.* [15], who used complex plane analysis to study the real and imaginary components of the electromodulation reflection coefficient, $\rho=(1/R).(dR/dE)$ as a function of frequency in order to gain kinetic information concerning adsorption-desorption processes at metal electrodes. Complex plane plots for both diffusion controlled and kinetically controlled processes were presented. More recently, Gabrielli *et al.* [16,17] have studied the electro optical transmittance ($EOT=\Delta T/\Delta E.T$) and absorbance ($\Delta\mathcal{A}/\Delta E$) of WO_3 films. Peter *et al.* [18,19] have investigated polyaniline (PANI) films on ITO coated glass electrodes using potential-modulated transmittance ($\Delta T/T$) and *ac* impedance. Kalaji and Peter derived a relationship between the optical transmittance response and the integrated Faradaic admittance Y_F. Analysis of data obtained for PANI films showed that the current in the voltammetric response is associated entirely with charge transfer and not with charging of the electrical double layer. This work demonstrated that it is possible to distinguish between Faradaic and non-Faradaic processes, using the complementary techniques of PMR and impedance.

The technique of *ac* modulated transmittance, where $T=\Delta T/\Delta E$, has also been referred to as Color Impedance Spectroscopy (CIS) [20-24]. CIS was used to study the

charge transfer kinetics of polypyrrole films [20-23] and the electrochromic behaviour of WO_3 films [24]. Frequency response analysis has also been used to determine the electron transfer rate constant of an electrochemically active dye (hemin and Nile Blue A) adsorbed on a glassy carbon electrode [25].

In this work, two limiting cases are used to model the relationship between frequency response PMR and impedance spectroscopy. A diffusion-controlled redox process in solution, and that of a kinetically controlled surface redox process are considered. By modelling the relationship between frequency response and impedance for the two limiting cases, it shows that it is possible to apply frequency response analysis of PMR to more complex systems.

2.4.1 Frequency response analysis : Diffusion-controlled process

When considering the frequency response of a diffusion-controlled process, the simplest system to look at is a single reversible electron transfer process, $O + ne^- \rightleftharpoons R$ at the surface of an inert electrode, where O and R are solution redox species.

The relationship between the optical and Faradaic responses of a redox process has been defined as :

$$\frac{\Delta R}{R} = -\left(\frac{4.606\Delta\varepsilon}{nFA\cos\theta}\right)\int_0^t I_F(\omega t)dt \qquad (2.18)$$

Using complex plane analysis, where : $I_{ac} = I_0 \sin(\omega t + \phi) \equiv I_0 e^{j\phi}.e^{j\omega t}$

$$\int I_F(\omega t)dt = \left[\frac{I_0 e^{j\phi}}{j\omega}\right]e^{j\omega t} \qquad (2.19)$$

Also, $I_0 e^{j\phi} e^{j\omega t}$ can be expressed as $Y_F E_o e^{j\omega t}$ since by definition, $I_o e^{j\phi} \equiv Y_F E_o$, where Y_F=Faradaic admittance and E_o=potential amplitude of modulation (A.M.). This gives

$$\frac{\Delta R}{R} = -\left(\frac{4.606\Delta\varepsilon}{nFA\cos\theta}\right)\frac{Y_F E_o e^{j\omega t}}{j\omega} = -\left(\frac{4.606\Delta\varepsilon}{nFA\cos\theta}\right)\frac{Y_F E_{ac}}{j\omega} \tag{2.20}$$

where $E_{ac}=E_o e^{j\omega t}$

It has already been shown in **Figure 2.3** that the optical response $\Delta R/R$ can be represented in complex notation. As a result, it is possible to resolve the optical signal into real and imaginary components. Since the applied modulated potential is taken as the reference, the amplitude of modulation has no imaginary component. Therefore $Re(E)=E_0$, which gives the following expression for the optical response.

$$\frac{\Delta R}{R} = -\left(\frac{4.606\Delta\varepsilon}{nFA\cos\theta}\right)\frac{\left(Re(Y_F) + jIm(Y_F)\right)}{j\omega}E_o \tag{2.21}$$

Identification of the real and imaginary components of $\Delta R/R$ gives :

$$Re\left(\frac{\Delta R}{R}\right) = -\left(\frac{4.606\Delta\varepsilon}{nFA\cos\theta}\right)Im\left(\frac{Y_F}{\omega}\right)E_o \tag{2.22}$$

$$Im\left(\frac{\Delta R}{R}\right) = \left(\frac{4.606\Delta\varepsilon}{nFA\cos\theta}\right)Re\left(\frac{Y_F}{\omega}\right)E_o \tag{2.23}$$

It is clear from this derivation that the frequency dependent $\Delta R/R$ signal is 90° out of phase with respect to the Faradaic current, I_F. Most importantly, it has been

demonstrated that there is a direct relationship between the PMR signal and Faradaic response, Y_F and hence impedance, Z_F. These expressions are similar to those reported by Fermin *et al.* [24] where PMR spectroscopy was used to study the kinetics of charge transfer across liquid | liquid interfaces.

The equivalent circuit for a simple electrode process involving soluble redox species is illustrated in **Figure 2.5**.

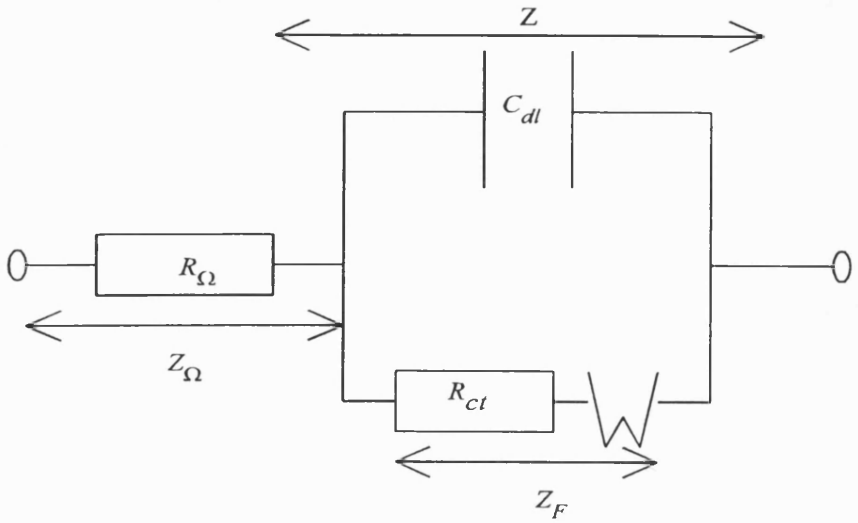

Figure 2.5 : Equivalent circuit for a simple electrode process, involving a soluble redox species. R_Ω=solution resistance, C_{dl}=double layer capacitance, R_{ct}=charge transfer resistance, W=Warburg impedance.

For this equivalent circuit, the following expressions have been derived for the total impedance, Z_{tot}, of the system [27].

$$Re(Z_{tot}) = R_\Omega + \frac{R_{ct} + \sigma\omega^{-\frac{1}{2}}}{\left(C_{dl}\sigma\omega^{\frac{1}{2}} + 1\right)^2 + \omega^2 C^2_{dl}\left(R_{ct} + \sigma\omega^{-\frac{1}{2}}\right)^2} \qquad (2.24)$$

$$Im(Z_{tot}) = \frac{\omega C_{dl}\left(R_{ct} + \sigma\omega^{-\frac{1}{2}}\right)^2 + \sigma\omega^{-\frac{1}{2}}\left(\omega^{\frac{1}{2}} C_{dl}\sigma + 1\right)}{\left(C_{dl}\sigma\omega^{\frac{1}{2}} + 1\right)^2 + \omega^2 C^2{}_{dl}\left(R_{ct} + \sigma\omega^{-\frac{1}{2}}\right)^2} \tag{2.25}$$

where $$\sigma = \frac{RT}{n^2 F^2 A\sqrt{2}}\left(\frac{1}{D_o^{1/2} C_o^*} + \frac{1}{D_R^{1/2} C_R^*}\right) \tag{2.26}$$

D_o and D_R are the diffusion coefficients of the oxidised and reduced forms respectively and C_o^* / C_R^* are the concentrations of each species in the bulk solution.

From the expressions in Eq. (2.24) and Eq. (2.25), a plot of $Im(Z_{tot})$ *vs.* $Re(Z_{tot})$ as a function of ω should produce a semi-circular response at high ω and a straight line at the lower ω range. In order to obtain kinetic information regarding the system under study, it is necessary to look at the limiting behaviour of $Im(Z_{tot})$ and (ReZ_{tot}) at high and low ω values.

In the limit $\omega \to \infty$, according to Eq. (2.24), $Re(Z_{tot}) \to R_\Omega$ and it is therefore possible to evaluate the solution resistance from the intercept of the semi-circle with the *x*-axis at the high frequency limit. When $\omega \to 0$, Eq. (2.24) and Eq. (2.25) can be simplified to :

$$Re(Z_{tot}) = R_\Omega + R_{ct} + \sigma\omega^{-\frac{1}{2}} \tag{2.27}$$

$$Im(Z_{tot}) = \sigma\omega^{-\frac{1}{2}} + 2\sigma^2 C_{dl} \tag{2.28}$$

A plot of $Im(Z_{tot})$ *vs.* $Re(Z_{tot})$ as a function of ω should therefore give a straight line plot of gradient equal to 1, where the extrapolated line intersects the real axis at $R_\Omega + R_{ct} - 2\sigma^2 C_{dl}$. In the case of a solution process, it is the low frequency limit which is of

importance due to the mass transfer control of a solution process. The straight line is therefore characteristic of a diffusion-controlled electrode process, where the Warburg impedance, W is the contributing factor. As a result of the relationship between Z_{tot} and ω, and as illustrated in Eq. (2.28) and Eq. (2.29), evaluation of C_{dl} and R_{ct} is also possible by plotting $Re(Z_{tot})$ *vs.* $\omega^{-1/2}$ and $Im(Z_{tot})$ *vs.* $\omega^{-1/2}$. **Figure 2.6** illustrates the effect of frequency on an impedance plot where mass transfer control and kinetic control are present.

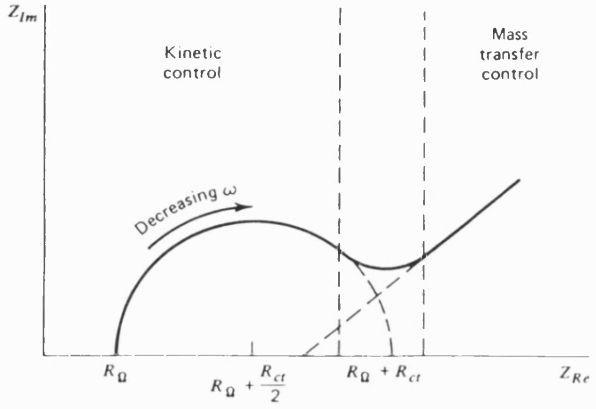

Figure 2.6 : The effect of frequency on an impedance plot where mass transfer control and kinetic control are present [25].

Knowledge of C_{dl} and R_{ct} then enables the Faradaic impedance, Z_F and hence admittance, Y_F of the system to be calculated. The relationship between total impedance, Y_{tot} and Faradaic admittance, Y_F is derived as follows.

From the equivalent circuit shown in **Figure 2.5**, $Z_{tot}=Z_\Omega+Z$, where $Z_\Omega=R_\Omega$.

Hence : $Re(Z)=Re(Z_{tot})-R_\Omega$ (2.29)

$Im(Z)=Im(Z_{tot})$ (2.30)

The real and imaginary components of admittance, Y, are

$$Re(Y) = \frac{1}{Z^2} Re(Z) \tag{2.31}$$

$$Im(Y) = \frac{1}{Z^2} Im(Z) \quad \text{where } Z^2 = Re^2(Z) + Im^2(Z) \tag{2.32}$$

Since $Y = Y_F + Y_{dl}$, where $Y_{dl} = j\omega C_{dl}$ and Y_{dl}=admittance at the double layer, C_{dl}=double layer capacitance:

$$Re(Y_F) = Re(Y) \tag{2.33}$$

$$Im(Y_F) = Im(Y) - C_{dl}\omega \tag{2.34}$$

Hence : $$Re(Z_F) = \frac{1}{Y_F^2} Re(Y_F) \tag{2.35}$$

$$Im(Z_F) = \frac{1}{Y_F^2} Im(Y_F) \tag{2.36}$$

where $$Y_F^2 = Re^2(Y_F) + Im^2(Y_F) \tag{2.37}$$

According to Eq. (2.22) and Eq. (2.23), provided the relationship between the optical response of the system and the Faradaic admittance holds, a plot of $Re(\Delta R/R)$ *vs.* $Im(Y_F)/\omega$ and $Im(\Delta R/R)$ *vs.* $Re(Y_F)/\omega$ should have a linear relationship, with a slope corresponding to $k = \left(\frac{4.606\Delta\varepsilon}{nFA\cos\theta}\right)E_o$.

Simulation of the optical response as a function of frequency using equivalent circuit analysis provides a means of verifying the relationship between the optical and Faradaic response. The equivalent circuit for the Faradaic reaction of a soluble system is

a series combination of R_{ct} and Warburg impedance, W (see **Figure 2.5**). The following expressions can be derived [27] for $Re(Z_F)$ and $Im(Z_F)$ in terms of R_{ct} and σ.

$$Re(Z_F) = R_{ct} + \left(\frac{1}{\omega}\right)^{1/2} \sigma \tag{2.38}$$

$$Im(Z_F) = \left(\frac{1}{\omega}\right)^{1/2} \sigma \tag{2.39}$$

Rearrangement of Eq. (2.35) and Eq. (2.36) gives expressions for the components of Faradaic admittance, Y_F, as shown :

$$Re(Y_F) = \frac{1}{|Z_F|^2}\left(Re(Z_F)\right) \tag{2.40}$$

$$Im(Y_F) = -\frac{1}{|Z_F|^2}\left(Im(Z_F)\right) \tag{2.41}$$

where $|Z_F|$ can be expressed in terms of Eq. (2.36) and Eq. (2.37) as follows.

$$|Z_F|^2 = \left[R_{ct} + \left(\frac{1}{\omega}\right)^{1/2} \sigma\right]^2 + \left[\left(\frac{1}{\omega}\right)^{1/2} \sigma\right]^2 \equiv R_{ct}^2 + 2R_{ct}\sigma\left(\frac{1}{\omega}\right)^{1/2} + \frac{2\sigma^2}{\omega} \tag{2.42}$$

Therefore the expressions for optical response in Eq. (2.22) and Eq. (2.24) can be written in terms of R_{ct} and σ giving :

$$Re\left(\frac{\Delta R}{R}\right) = -k\frac{1}{|Z_F|^2 \omega}\left(\frac{1}{\omega}\right)^{1/2} \sigma \tag{2.43}$$

$$Im\left(\frac{\Delta R}{R}\right) = k\frac{1}{|Z_F|^2\omega}\left[R_{ct} + \left(\frac{1}{\omega}\right)^{1/2}\sigma\right] \tag{2.44}$$

where $$k = \left(\frac{4.606\Delta\varepsilon}{nFA\cos\theta}\right)E_o \tag{2.45}$$

Let us now consider the two limiting cases for ω in relation to the optical response.

When $\omega \to \infty$, $Re\left(\frac{\Delta R}{R}\right)$ and $Im\left(\frac{\Delta R}{R}\right) \to 0$

and when $\omega \to 0$, $|Z_F|^2.\omega \to 2\sigma^2$, :

Hence : $$Re\left(\frac{\Delta R}{R}\right) = -.\frac{k}{2\sigma}\left(\frac{1}{\omega}\right)^{1/2} \tag{2.46}$$

$$Im\left(\frac{\Delta R}{R}\right) = \frac{k.R_{ct}}{2\sigma^2} + \frac{k}{2\sigma}\left(\frac{1}{\omega}\right)^{1/2} \tag{2.47}$$

Substitution of Eq. (2.46) into Eq. (2.47) leads to the relationship

$$Im\left(\frac{\Delta R}{R}\right) = -Re\left(\frac{\Delta R}{R}\right) + \frac{k.R_{ct}}{2\sigma^2} \tag{2.48}$$

It follows that in the low frequency limit, a plot of $Im(\Delta R/R)$ *vs.* $Re(\Delta R/R)$ will have a line of slope=1 and an intercept=$k.\frac{R_{ct}}{2\sigma^2}$. This correlates with the corresponding impedance plot for a diffusion-controlled process discussed earlier. Values for the

kinetic parameters R_{ct} and σ, can therefore be obtained from frequency response analysis studies of the optical response for a solution process.

2.4.2 Frequency response analysis : A surface bound redox system

When considering a surface bound redox process, e.g. redox polymers [18-23], the relationship between the optical and electrical response, as discussed in Section 2.2 still applies. However, in the case of a surface bound system, the concentration of the surface film is defined as Γ (mol cm^{-2}), with a surface film thickness d. If we consider a simple surface redox process $O + ne^- \rightleftharpoons R$, the following expression for absorbance is derived :

$$\mathcal{A}(\lambda,x,t) = \frac{2\Delta\varepsilon(\lambda)}{\cos\theta}\int_0^d \Gamma(x,t)dx \qquad (2.49)$$

From this, the same relationship between optical response and Faradaic admittance is derived.

The equivalent circuit of a simple electrode process involving a surface bound redox process is illustrated in **Figure 2.7**.

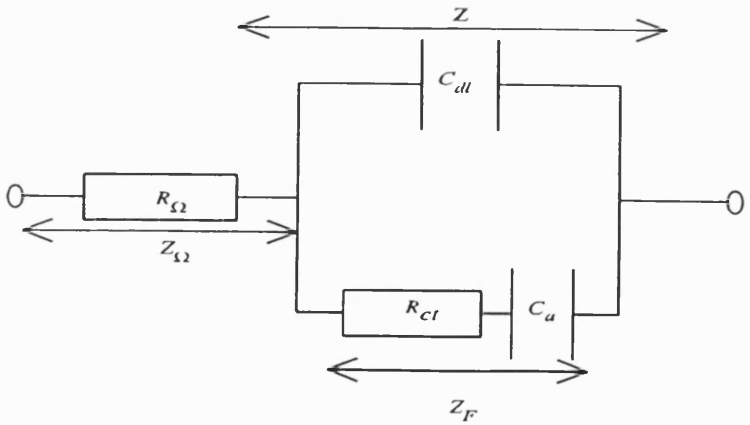

Figure 2.7 : The equivalent circuit for a simple electrode process involving a surface bound redox system.

The equivalent circuit of a Faradaic response at a surface bound redox system corresponds to a charge transfer resistance R_{ct} and capacitor C_a in series. The expressions for the Faradaic admittance response and thus that of the optical response can be derived as follows.

$$Re(Z_F) = R_{ct} \tag{2.50}$$

$$Im(Z_F) = \frac{1}{jC_a\omega} \tag{2.51}$$

Hence : $$|Z_F|^2 = R_{ct}^2 + \frac{1}{C_a^2\omega^2} \tag{2.52}$$

The expressions for the Faradaic admittance can therefore be defined as

$$Re(Y_F) = \frac{1}{|Z_F|^2} Re(Z_F) = C_a \frac{\omega^2 C_a R_{ct}}{\omega^2 C_a^2 R_{ct}^2 + 1} \tag{2.53}$$

$$Im(Y_F) = -\frac{1}{|Z_F|^2} Im(Z_F) = C_a \frac{\omega}{\omega^2 C_a^2 R_{ct}^2 + 1} \tag{2.54}$$

As a result, the same expressions are derived for the relationship between Faradaic admittance, Y_F and the optical response, $\Delta R/R$ of a surface film (see Eq. (2.22) and Eq. (2.23)), where substitution of Eq. (2.53) and Eq. (2.54) gives (for $R_{ct} >> R_\Omega$) :

$$Re\left(\frac{\Delta R}{R}\right) = -\left(\frac{4.606\Delta\varepsilon}{nFA\cos\theta}\right) Im\left(\frac{Y_F}{\omega}\right) E_o = -kC_a \frac{1}{\omega^2 C_a^2 R_{ct}^2 + 1} \tag{2.55}$$

$$Im\left(\frac{\Delta R}{R}\right)=\left(\frac{4.606\Delta\varepsilon}{nFA\cos\theta}\right)Re\left(\frac{Y_F}{\omega}\right)E_o=-kC_a\frac{\omega C_a R_{ct}}{\omega^2 C_a^2 R_{ct}^2+1} \tag{2.56}$$

where : $$k=\left(\frac{4.606\Delta\varepsilon}{nFA\cos\theta}\right)E_o \tag{2.45}$$

Rearrangement of Eq. (2.55) and Eq. (2.56) gives :

$$Im\left(\frac{\Delta R}{R}\right)=-\omega C_a R_{ct}.Re\left(\frac{\Delta R}{R}\right) \tag{2.57}$$

It follows therefore that for a surface film, a plot of $\frac{Im(\Delta R/R)}{Re(\Delta R/R)}$ *vs* ω should give a straight line of slope $-C_aR_{ct}$. Elimination of ω from the expression, as in the case of impedance, is carried out as follows from Eq. (2.57).

$$Im\left(\frac{\Delta R}{R}\right)^2=-\omega^2 C_a^2 R_{ct}^2.Re\left(\frac{\Delta R}{R}\right)^2 \tag{2.58}$$

Rearrangement of Eq. (2.55) gives

$$\omega^2 C_a^2 R_{ct}^2=\frac{kC_a}{Re\left(\frac{\Delta R}{R}\right)}-1 \tag{2.59}$$

Substitution of the Eq. (2.59) in Eq. (2.58) gives :

$$Im\left(\frac{\Delta R}{R}\right)^2=Re\left(\frac{\Delta R}{R}\right)kC_a-Re\left(\frac{\Delta R}{R}\right)^2$$

which can also be expressed in the form :

$$Im\left(\frac{\Delta R}{R}\right)^2 + Re\left(\frac{\Delta R}{R}\right)^2 - Re\left(\frac{\Delta R}{R}\right)kC_a + \frac{1}{4}(kC_a)^2 - \frac{1}{4}(kC_a)^2 = 0 \qquad (2.60)$$

$$Im\left(\frac{\Delta R}{R}\right)^2 + \left(Re\left(\frac{\Delta R}{R}\right) - \frac{kC_a}{2}\right)^2 = \left(\frac{kC_a}{2}\right)^2 \qquad (2.61)$$

This is the equation of a semi-circle, as in the case of impedance for a kinetically-controlled process. The plot should therefore have the following characteristics, as illustrated in **Figure 2.8**.

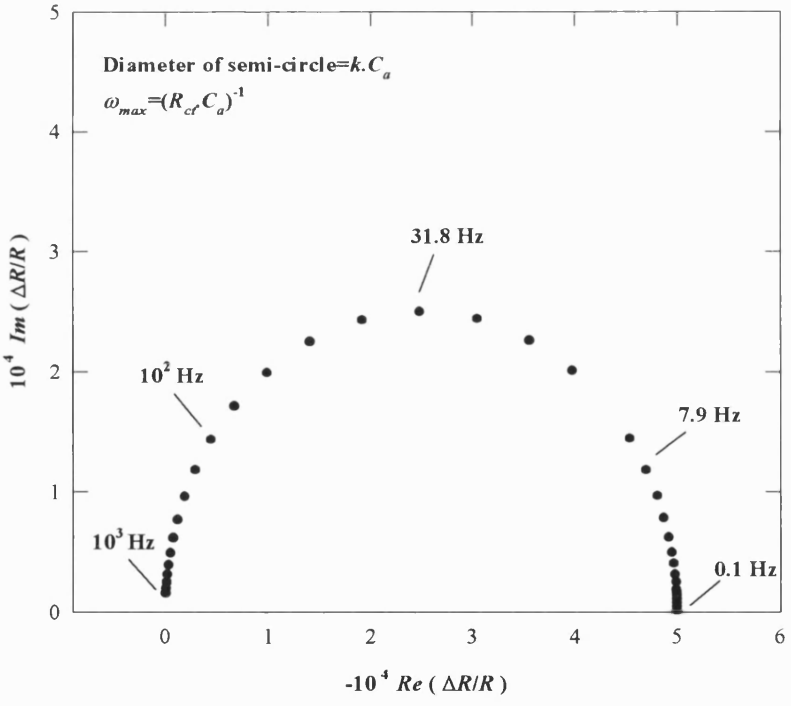

Figure 2.8 : Characteristics for the optical response of a kinetically controlled process. R_{ct}=50Ω; C_a=1x10^{-4}F; k=5.

It follows that direct access to the capacitance C_a and charge transfer resistance R_{ct} of a surface bound redox system is possible from frequency response analysis of the optical response.

2.5 PMR Voltammetry

In PMR voltammetry, the effect of potential on the optical response is studied. PMR voltammetry is directly related to *ac* polarography, where the potential is modulated and *ac* current response, I_{ac}, is measured as a function of Potential, E. It is therefore possible to derive a theoretical relationship between the PMR response and that of *ac* polarography.

From the principles of *ac* polarography [27], for a simple reversible electrode process, $O + ne^- \rightleftharpoons R$:

$$I_{ac} = \frac{E_0}{Z_F} = \frac{n^2F^2A\omega^{1/2}D_0^{1/2}C_0^*}{4RT\cosh^2(a/2)}E_0 \tag{2.62}$$

where : $$a = \frac{nF}{RT}\left(E_{dc} - E^{o'}\right) \tag{2.63}$$

Since : $$\frac{I_{ac}}{E_0} = Y_F$$

$$Y_F = \frac{1}{Z_F} = \frac{n^2F^2A\omega^{1/2}D_0^{1/2}C_0^*}{4RT\cosh^2(a/2)} \tag{2.64}$$

The following theoretical relationships have already been derived for the optical response and corresponding Faradaic impedance :

$$Re\left(\frac{\Delta R}{R}\right) = -k\frac{1}{|Z_F|^2\omega}\left(\frac{1}{\omega}\right)^{1/2}\sigma \tag{2.43}$$

$$Im\left(\frac{\Delta R}{R}\right) = k\frac{1}{|Z_F|^2\omega}\left[R_{ct} + \left(\frac{1}{\omega}\right)^{1/2}\sigma\right] \tag{2.44}$$

where $$k = \left(\frac{4.606\Delta\varepsilon}{nFA\cos\theta}\right)E_0 \tag{2.45}$$

Therefore, substitution of Eq. (2.63) into Eq. (2.43) and Eq. (2.44) gives the following expressions for the theoretical relationship between the *ac* admittance response Y_F, and optical response, $\Delta R/R$, of a simple redox system.

$$Re\left(\frac{\Delta R}{R}\right) = -k\frac{Y_F^2}{\omega}\left(\frac{1}{\omega}\right)^{1/2}\sigma \equiv -k\left[\frac{n^2F^2AD_0^{1/2}C_0^*}{4RT\cosh^2(a/2)}\right]^2\cdot\left(\frac{1}{\omega}\right)^{1/2}\sigma \tag{2.65}$$

$$Im\left(\frac{\Delta R}{R}\right) = k\frac{Y_F^2}{\omega}\left[R_{ct} + \left(\frac{1}{\omega}\right)^{1/2}\sigma\right].\equiv k\left[\frac{n^2F^2AD_0^{1/2}C_0^*}{4RT\cosh^2(a/2)}\right]^2\cdot\left[R_{ct} + \left(\frac{1}{\omega}\right)^{1/2}\sigma\right] \tag{2.66}$$

where provided the *dc* process follows Nernstian behaviour [27] :

$$\sigma = \frac{4RT}{\sqrt{2}n^2F^2AD_0^{1/2}C_0^*}\cosh^2\left(\frac{a}{2}\right) \tag{2.67}$$

$$R_{ct} = \frac{RT}{n^2F^2Ak^oC_0^*} \tag{2.68}$$

where : $E^{o'}$ = formal electrode potential

C_0^* = concentration of the oxidised species

D_0 = diffusion coefficient

k^0 = standard heterogeneous rate constant

The above derivation illustrates the theoretical relationship between optical response in PMR voltammetry and *ac* voltammetry. From the derivation it is shown that the optical response is proportional to $(1/\omega)^{1/2}$. The factor $\cosh^2(a/2)$ also results in a characteristic bell-shaped feature of a PMR voltammogram, which has a maximum PMR response at $a/2=0$ i.e. when E_{dc}=formal standard potential $E^{o'}$. The relationships derived in Eq. (2.65) and Eq. (2.66) therefore enable the simulation of a PMR voltammogram which can then be further used to verify the relationship derived in Eq. (2.22)and Eq. (2.23).

2.6 Conclusions

The theoretical principles discussed demonstrate that PMR is a very powerful technique which can study directly the Faradaic response of a system. Frequency response analysis of the optical response, $\Delta R/R$, for both surface and solution systems, enables the direct measurement of Faradaic impedance at a given frequency without the knowledge of R_Ω or C_{dl}. The technique therefore enables both spectroscopic and kinetic information to be obtained regarding the system under study. The different frequency dependent responses observed for a kinetically controlled surface process and a diffusion controlled solution process, can also be used as a diagnostic to distinguish between the two. The $Fe(CN)_6^{4-}$ / $Fe(CN)_6^{3-}$ redox couple is used as a model solution system in Chapter 4 to verify the PMR theory discussed here.

2.7 References

1. C. Gutiérrez in "Spectroscopic and Diffraction Techniques in Interfacial Electrochemistry" : Kluwer Academic Publishers : Amsterdam (1990)
2. B.O.Seraphin, *Phys. Rev.*, **140A**, 1716 (1965)
3. A. Bewick and A.M. Tuxford, *Faraday Soc. Symp. No.4*, 114 (1970)
4. W. Paatsch, *Surface Science*, **37**, 59 (1973)
5. N. Hara and K. Sugimoto, *J. Electrochem. Soc.*, **126**(8), 1328 (1979)
6. J. Caram, C. Gutiérrez, G. Pimenta and M.I. da Silva Pereira, *J. Electroanal. Chem.*, **344**, 199 (1993)
7. C. Gutiérrez and M.A. Martinez, *J. Electrochem. Soc.*, **131**, 1873 (1986)
8. A.W.B. Aylmer-Kelly, A. Bewick, P.R. Cantrill and A.M. Tuxford, *Discuss., Faraday Soc.*, **56**, 96 (1973)
9. A. Bewick and A.M. Tuxford, *Electroanal. Chem. & Interfacial Electrochem.*, **47**, 255 (1973)
10. J.D.E. McIntyre and W.F.Peck, Jr., *Faraday Discuss., Chem. Soc.*, **56**, 122 (1974)
11. J.A. Caram and C. Gutiérrez, *J. Electroanal. Chem.*, **291**, 289 (1990)
12. J.D.E. McIntyre, *Surface Science*, **37**, 658 (1973)
13. A. Scott Hinman, J.F. McAleer and S. Pons, *J. Electroanal. Chem.*, **154**, 45 (1983)
14. see e.g. D.J. Blackwood and L.M. Peter, *Electrochimica Acta*, **35**, 1073 (1990)
15. R. Adzic, B. Cahan and E. Yeager, *J. Chem. Phys.*, **58**, 1780 (1973)
16. C. Gabrielli , *Electrochimica Acta*, **35**, 1553 (1990)
17. C. Gabrielli, M. Keddam, H. Perrot and R. Torresi, *J. Electroanal. Chem.*, **378**, 85 (1994)

18. R.S. Hutton, M. Kalaji and L.M. Peter, *J. Electroanal. Chem.*, **270**, 429 (1989)

19. M. Kalaji and L.M. Peter, *J. Chem. Soc., Faraday Trans.*, **87**, 853 (1991)

20. T Amemiya, K. Hashimoto and A. Fujishima, *J. Phys. Chem.*, **97**, 4187 (1993)

21. T. Amemiya, K. Hashimoto and A. Fujishima, *J. Phys. Chem.*, **97**, 4192 (1993)

22. T. Amemiya, K. Hashimoto and A. Fujishima, *J. Phys. Chem.*, **97**, 9736 (1993)

23. T. Amemiya, K. Hashimoto and A. Fujishima, *J. Electroanal. Chem.*, **77**, 143 (1994)

24. J.J. Kim, D.A. Tryk, T. Amemiya, K. Hashimoto and A. Fujishima, *J. Electroanal. Chem.*, **435**, 31 (1997)

25. Z.Q. Feng, T. Sagara and K. Niki, *Anal. Chem.*, **67**, 3564 (1995)

26. D. Fermin, Z. Ding, P.-F. Brevet and H.H. Girault, *J. Electroanal. Chem.*, **447**, 125 (1998)

27. A.J. Bard and L.R. Faulkner, "*Electrochemical Methods-Fundamentals and Applications*" Wiley and Sons (1980)

Chapter 3

Chapter 3

Experimental Methodology

3.1 Electrode Preparation

Electrochemical and spectroscopic studies of the ferro-ferricyanide redox couple were carried out at a platinum electrode. Platinum foil (Goodfellow) of 0.25mm thickness was mounted in the end of a cylindrical glass-tube and sealed in glass. A circular mounted Pt electrode of diameter 7.3mm and geometric surface area of 0.419 ± 0.002 cm^2 was used to study the frequency response analysis of the ferro-ferricyanide redox couple. All other experiments were performed at a Pt electrode of dimensions 2.4x6.2x0.25mm and geometric surface area of 0.149 ± 0.002 cm^2. Electrode areas were evaluated using a standard travelling microscope (Beck, London) with an accuracy to within 0.001cm. The glass mounted Pt electrode (2.4x6.2x0.25mm) was also used as the substrate for the electrodeposition of Ru and Ru-Ir anodes.

In order to have a suitable electrode surface at which to perform electrochemical measurements and to electrodeposit films, it is first necessary to achieve a clean, highly polished surface. Pre-treatment of the Pt electrode involved polishing the surface using alumina sheet of grain size diameter 3 micron. Alumina powder (LECO Corporation) of 1.0 micron diameter was then used followed by 0.3 micron diameter, in order to achieve a smooth, mirror finish. Following polishing, the Pt electrode was rinsed thoroughly with Milli-Q H_2O in an ultrasonic bath (Branson Ultrasonics Corporation USA) of working frequency 47kHz ± 6%, in order to remove any alumina powder from the surface. (Milli-Q H_2O was obtained from a Milli RO 6 plus - Milli 185 water purification

system (Millipore) and will be referred to from now on in this way). Further cleaning was performed by rinsing the electrode surface with *conc.* H_2SO_4. The electrode was then rinsed thoroughly with Milli-Q H_2O. The Pt electrode was electrochemically cycled in 0.1M H_2SO_4 over the potential range of -0.30 to +1.20V *vs* SCE, at a sweep-rate=500mV s^{-1} for ~30 minutes, finishing at the cathodic limit. A cyclic voltammogram was then obtained. A well-defined Pt cyclic voltammogram showing the two hydrogen absorption peaks and surface oxidation region, was used as an indicator of a clean surface on which to electrodeposit ruthenium. An example is shown in **Figure 3.1**.

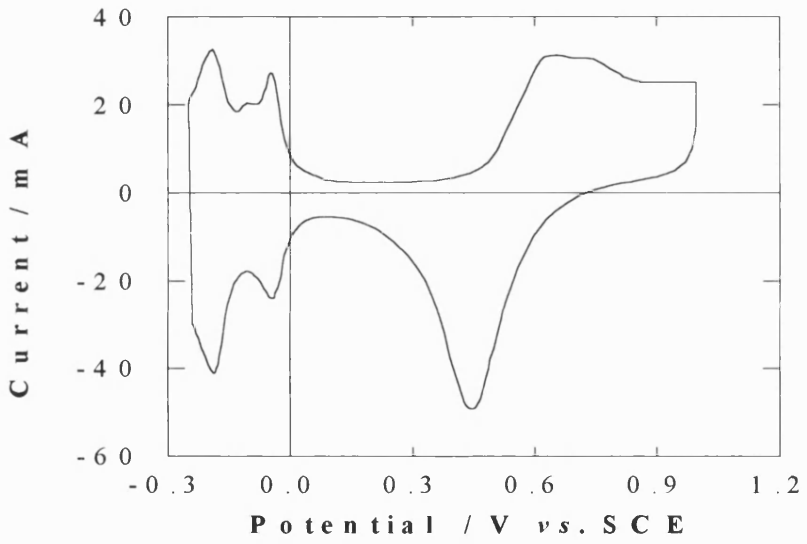

Figure 3.1 : A typical cyclic voltammogram of a Pt electrode in 0.1M H_2SO_4 : Sweep-rate=100mV s^{-1}.

3.2 Electrochemical Cell Designs

3.2.1 The electrodeposition cell

A two-compartment cell design was used for the electrodeposition of the electro-

catalytic films. The electrodeposition cell is illustrated in **Figure 3.2**. The Pt working electrode (W.E.) was immersed in the central water-jacketed cell compartment. A platinum gauze was used as the counter electrode (C.E.) contained in a side-arm compartment. An external thermostatic water-bath circulator (Grant Instruments (Cambridge) Ltd) provided the heated water source for the water-jacketed cell. A 1°C graduated mercury thermometer was used to monitor the temperature of the plating electrolyte and the solution was stirred using a magnetic stirrer. The electrolyte was also continuously stirred during the electrodeposition process.

3.2.2 The electrochemical and spectroscopic cell

A fully sealed glass cell was used for the cyclic voltammetry and PMR spectroscopy experiments. The cell had a three-compartment cell system. The working electrode was positioned in a side quick-fit joint, with two teflon O-rings attached to the glass electrode to provide an air-tight seal at the joint. The face of the working electrode was positioned at the centre of the cylindrical cell ~1mm away from the tip of the Luggin capillary of the reference electrode compartment. The Luggin capillary was used to minimise errors due to potential drop across the electrolyte under current-flow conditions. **Figure 3.3** illustrates the reference electrode compartment used for all measurements. Note that two teflon-O rings were used at the top of the Luggin capillary to ensure an air-tight seal. The counter electrode was contained in a side-arm compartment of the cell. The cell was equipped with three quartz optical windows at 60° angles to each other. This enabled the light beam to strike the Pt electrode through one window at an angle of 60° to the plane of the Pt foil and reflect at an angle of 120° through another window. **Figure 3.4** illustrates the cell system used for these studies.

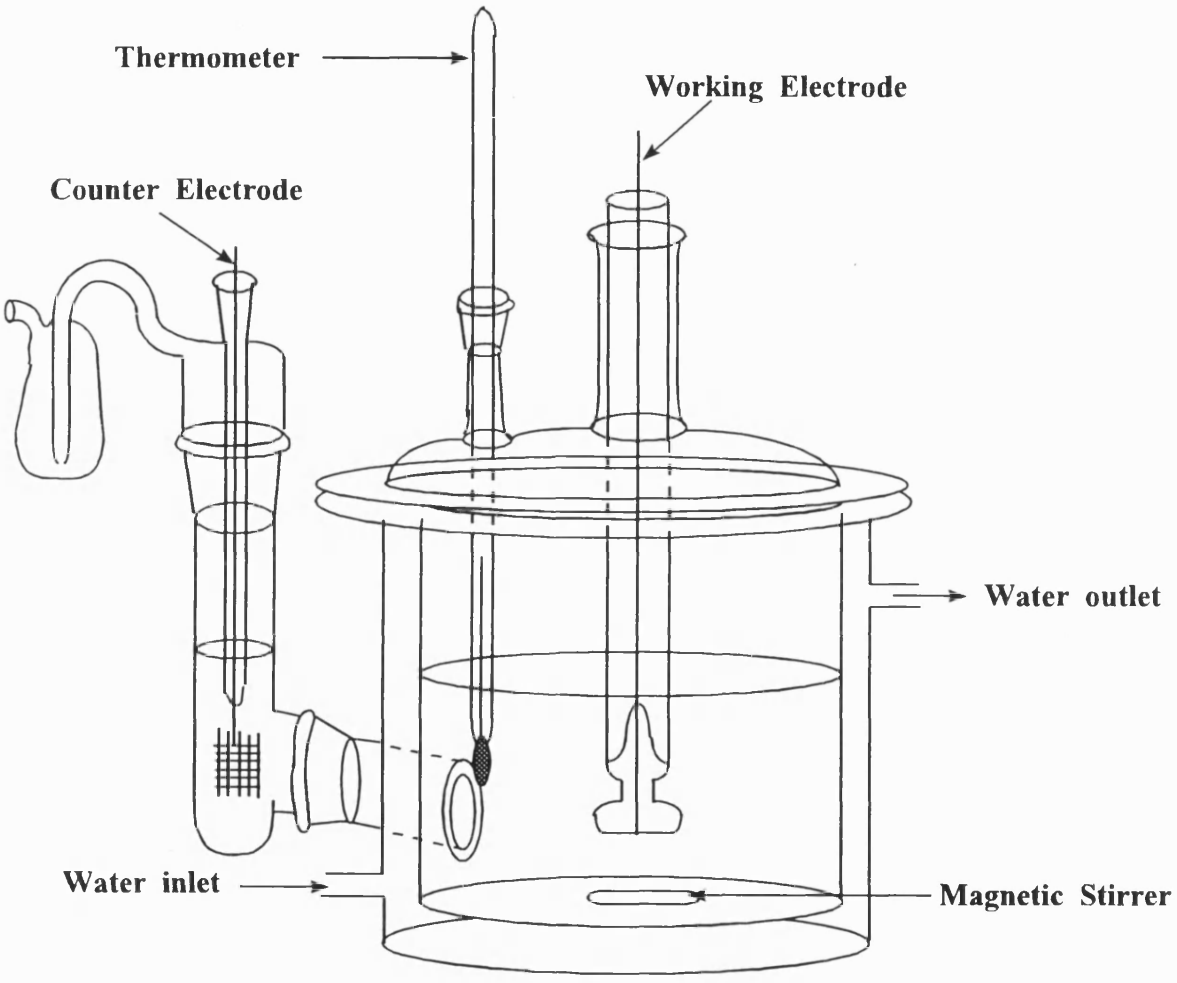

Figure 3.2 : A diagrammatic representation of the electrodeposition cell.

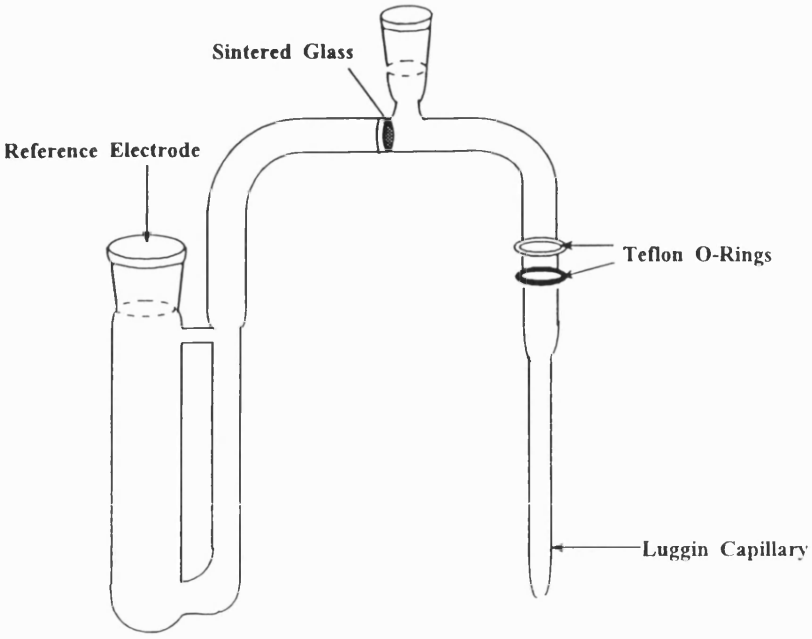

Figure 3.3 : Reference electrode compartment.

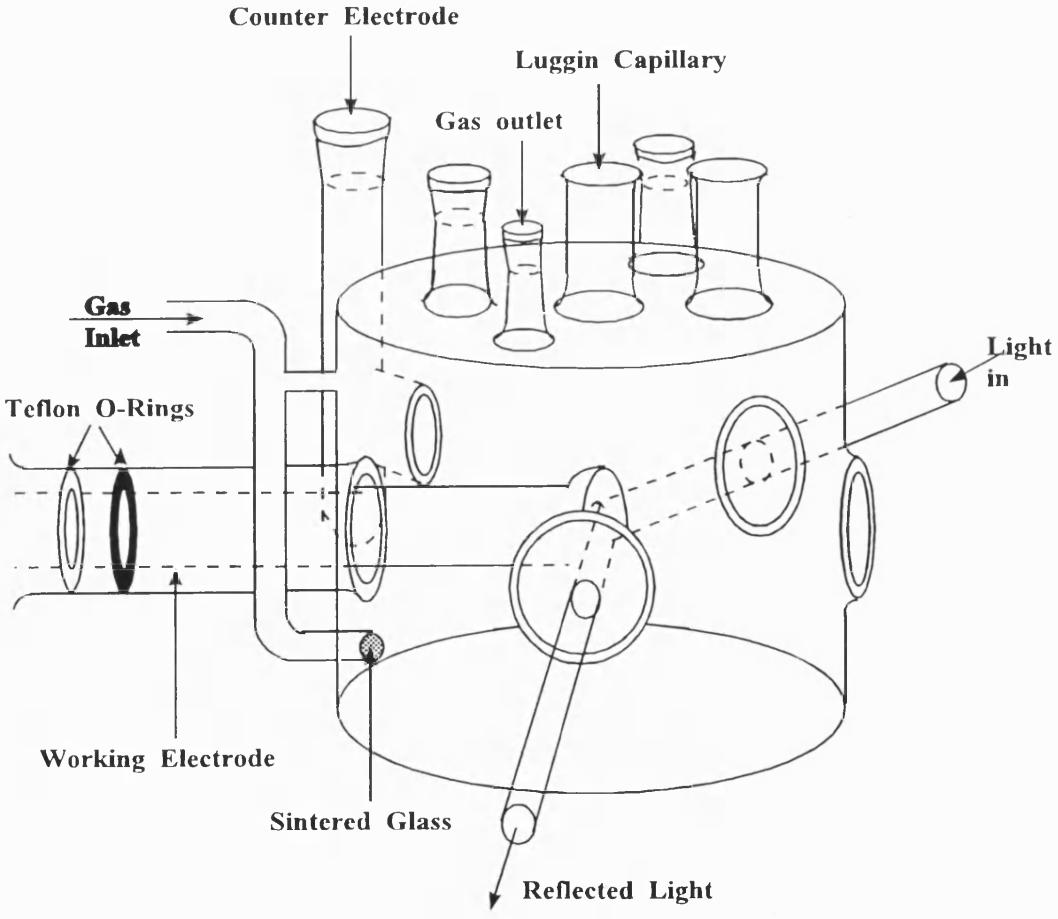

Figure 3.4 : The electrochemical / spectroscopic cell.

3.3 Electrodeposition methods

3.3.1 Electrodeposition of a ruthenium metal film

The ruthenium plating system was adapted from a system designed by Johnson Matthey [1]. A stable nitrido-bridged complex $K_3[Ru_2NCl_8(H_2O)_2]$ was the ruthenium source. A 10g dm^{-3} plating solution was prepared by dissolving 1.00g potassium diaquooctachloronitridodiruthenate (29.77%) in 100ml Milli-Q water. The solution was then adjusted to pH 1.0 by addition of AnalaR grade concentrated hydrochloric acid (37%). 1.00g AnalaR grade ammonium formate (>99%) was then added to obtain a 10g dm^{-3} solution and the pH adjusted to 1.5 by further addition of concentrated hydrochloric acid. The pH was monitored by a H19214 stick pH meter (HANNA Instruments), which was accurate to within ± 0.02.

A simple electrical circuit, incorporating a power supply and resistance in series, was used. An ISO-TECH IPS 302A power supply controlled the voltage and the current was monitored using an ISO-TECH IDM 91 digital voltmeter. Optimum conditions for electrodeposition were at a current density of 8 mA cm^{-2} and temperature=70°C. The following conditions were applied in order to deposit a ruthenium film of ~1 micron thickness. The thickness of the film was based on a 100% efficiency conversion of Ru(IV) to Ru metal.

Current=0.94mA

Voltage=13.5V

Resistance=13,000Ω

Time of electrodeposition=11 minutes

Temperature = 70°C (±1°C)

C.E.=Pt gauze electrode

Prior to electrodeposition, the Pt substrate was pre-treated as described earlier and following electrochemical cleaning, was rinsed with Milli-Q H_2O. The electrode was then transferred immediately to the electrodeposition cell.

Highly reflective, adherent ruthenium metal films were produced by this method. Following electrodeposition, the Ru electrode was immediately washed with Milli-Q H_2O and immersed in H_2O to prevent adsorption of contaminants prior to electrochemical and spectroscopic studies.

3.3.2 Electrodeposition of a ruthenium-iridium alloy film

The electrodeposition of ruthenium-iridium alloy films were performed galvanostatically using a plating bath with 0.2g dm^{-3} $(NH_4)_2RuCl_6$ and 0.8g dm^{-3} $(NH_4)_2IrCl_6$ salts in 0.1M HCl at a current density of ~40mA cm^{-2}. A Ru-Ir alloy film of composition $Ru_{0.4}Ir_{0.6}$ was obtained by this method. A Pt foil was used as the substrate and pre-treated as discussed in Section 3.1. The following conditions were used for the electrodeposition of a film of ~ 1 micron thickness :

Current=5.9mA

Time for electrodeposition=10 minutes

Voltage applied=16.5V

Resistance=2,710Ω

Temperature=70°C (±1°C)

3.4 Instrumentation

3.4.1 Voltammetric studies

Figure 3.5 illustrates schematically the apparatus used for cyclic voltammetry. A

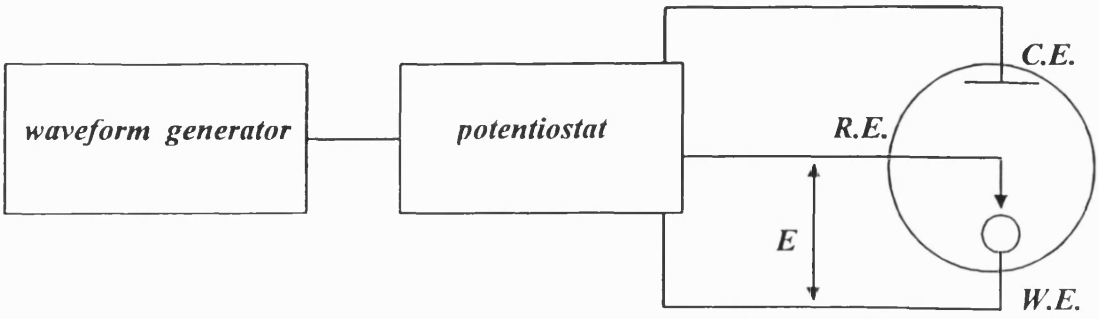

Figure 3.5 : A schematic of the experimental apparatus used for cyclic voltammetry.

home-built potentiostat controlled the potential applied to the electrochemical cell. The potential E between the reference electrode (R.E.) and working electrode was held constant at a value determined by the PPR1 waveform generator (Hi-Tek Instruments). The potential drop between the working electrode and counter electrode was varied by the potentiostat in order to keep the value of E constant. The resultant current flow between the counter electrode and working electrode therefore corresponded to that observed during voltammetric studies. The potential sweep-rate was controlled by the waveform generator. The resultant *i-E* curves were recorded on an XYt chart recorder (Philips PM8271).

In *ac* voltammetry, the same electrical set-up was used as for *dc* voltammetry. In addition, an *ac* sinusoidal signal was superimposed on the *dc* signal. A digital lock-in amplifier (Stanford Research Systems SR830 DSP) applied the *ac* signal to the electrochemical cell via the potentiostat. The current response at the potentiostat was then fed back into the lock-in amplifier, from which the real and imaginary components of the *ac* current response could be recorded on an XYt chart recorder.

3.4.2 Potential modulated reflectance spectroscopy (PMRS)

The PMRS set-up has previously been discussed in Chapter 2 (Section 2.1), but is

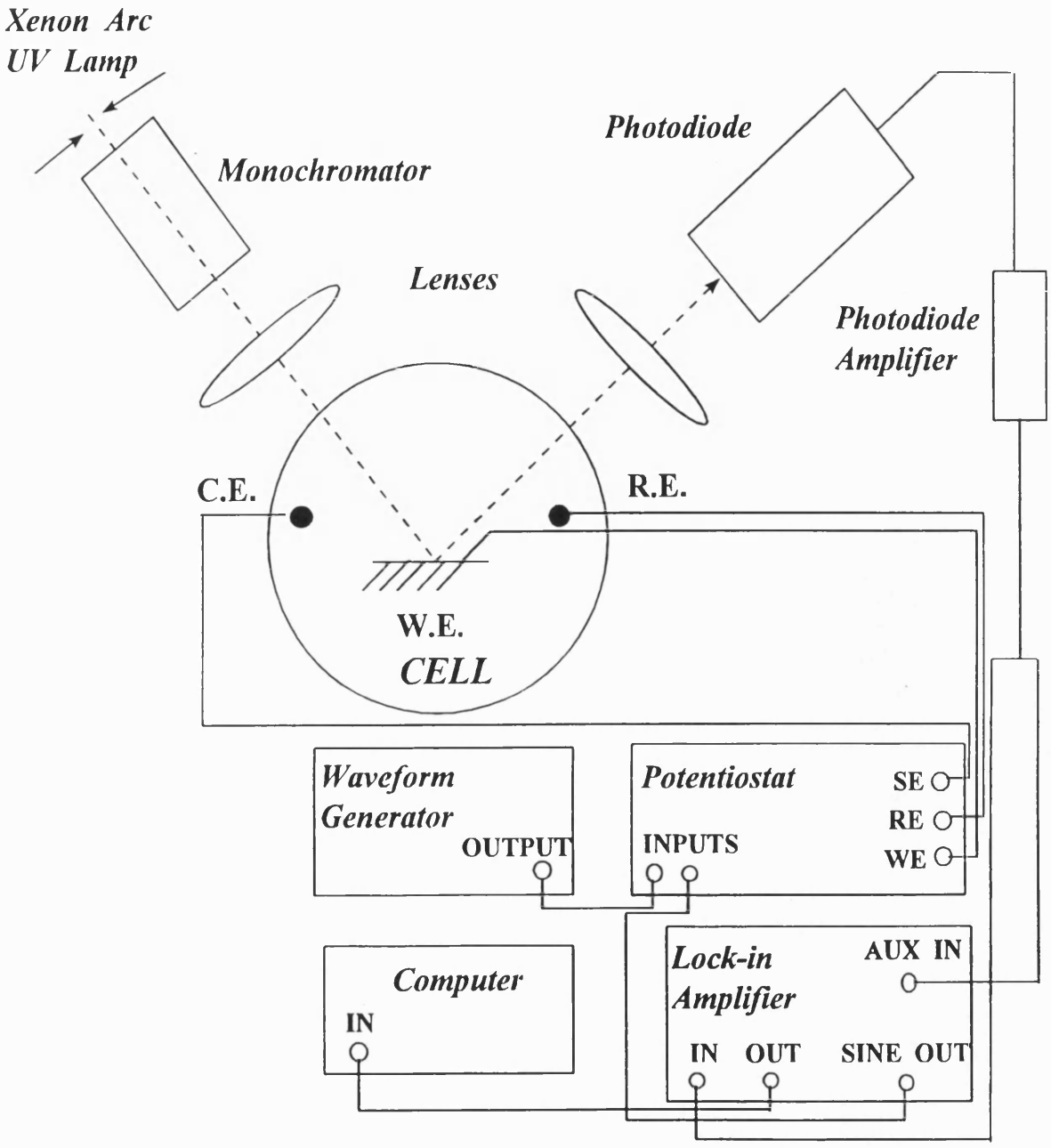

Figure 3.6 : A schematic diagram of the PMR apparatus.

shown here again in **Figure 3.6** for clarity. The unpolarised monochromatic light source incorporated an AMKO grating monochromator, which was connected to a 75 watt xenon arc lamp and power supply. The monochromator was fitted with two plane reflection 1200 lines mm^{-1} gratings (I and II) which were blazed at 500nm and 750nm respectively. As a result, wavelength selectivity over the range 300-1,200nm was possible. Grating I was selected for the wavelength range 300-480nm and grating II for >480nm. A slit-width of 1.5mm, both at the entrance and exit of the monochromator, was used for all experiments.

The reflected monochromatic light beam was focused onto a silicon photodiode with enhanced UV response. The output from the photodiode amplifier was connected to a digital lock-in amplifier which also provided the sinusoidal modulation signal to the potentiostat. The system (monochromator and lock-in amplifier) was controlled by a PC (personal computer) and was capable of resolving $\Delta R/R$ down to 10^{-6}.

3.4.3 UV-Visible spectroscopy

A Perkin-Elmer UV-Vis Spectrometer (Lambda 40) was used to recorded the UV-Visible absorption spectra of $Fe(CN)_6^{4-}$ and $Fe(CN)_6^{3-}$. The spectrometer was controlled by a PC fitted with a UVWinlab computer package. Spectra were recorded at 1nm intervals and at a scan-rate of 480nm min^{-1}.

3.5 Experimental Procedures

For all electrochemical and spectroscopic experiments, the electrolyte solutions were de-gassed by bubbling argon gas through the solution for a minimum of 20 minutes prior to analysis.

3.5.1 PMRS

All wavelength scan measurements were carried out over a set wavelength range of 300-700nm at a selected *dc* potential. A scan-rate of 20nm min^{-1} was used for all experiments and data was collected at 2.5nm intervals. The wavelength scans were obtained following the recording of a cyclic voltammogram of the electrode of interest. The potential was held at the cathodic limit until all the surface oxide was reduced i.e. until no reductive current was observed. The electrode was then swept to the potential of interest at a rate of 13mV s^{-1} and a wavelength scan was immediately recorded. Further spectra were obtained at different *dc* potentials by repeating the above standard procedure. All spectra were recorded by a PC, which also controlled the wavelength scan.

3.5.2 *AC* / PMR voltammetry

All *ac* / PMR voltammograms were recorded over the same potential region as their respective cyclic voltammograms to enable comparison. A scan-rate of 5mV s^{-1} was used for all experiments. The *ac* potential dependent current response was recorded on a X-Y chart recorder. PMR voltammograms were recorded by a PC.

3.5.3 Frequency dependent PMR

The frequency dependent PMR studies were obtained immediately following a PMR wavelength scan at the same potential of interest. The frequency of the *ac* signal applied by the lock-in amplifier was computer controlled and the optical response was recorded at 10 steps / decade. A 30 second time delay was used in between each measurement to allow for stabilisation of the optical response.

3.6 Standard Reagents

Table 3.1 lists the standard reagents used for all electrochemical and spectroscopic studies. All solutions were prepared using Milli-Q H_2O. Glass-ware was cleaned before use with 1:1 *conc.* H_2O_2 : H_2SO_4.

Compound	*Purity*	*Supplier*
Hydrogen peroxide [H_2O_2]	27.5% A.C.S.	Sigma-Aldrich
Hydrochloric acid [HCl]	37% AnalaR	Alfa
Potassium chloride [KCl]	99% A.C.S.	Sigma-Aldrich
Potassium ferricyanide trihydrate[$K_4Fe(CN)_6$].$3H_2O$	99% A.C.S.	Sigma-Aldrich
Potassium ferrocyanide trihydrate [$K_3Fe(CN)_6$].$3H_2O$	99% A.C.S.	Sigma-Aldrich
Potassium fluoride (KF)	99+% A.C.S.	Sigma-Aldrich
Sulphuric acid [H_2SO_4]	97.5+% AnalaR	Sigma-Aldrich
Sodium hydroxide pellets [NaOH]	99.99% Semi-conductor grade	Sigma-Aldrich

Table 3.1 : Standard reagents used for electrochemical and spectroscopic studies.

References

1. Johnson Matthey plc. Chemical Products, Orchard Road, Royston, Hertfordshire, SG8 5HE

2. M. Vukovic, D. Čukman, M. Milun, L.D. Atanasoska and R.T. Atanasoski, *J. Electroanal. Chem.*, **330**, 663 (1992)

3. D. Čukman, M. Vukovic and M. Milun, *J. Electroanal. Chem.*, **389**, 209 (1995)

Chapter 4

Chapter 4

Potential Modulated Reflectance Spectroscopy Analysis of a Model System : Ferro-Ferricyanide Redox Couple

The ferro-ferricyanide redox couple is a well characterised reversible redox system [1-8]. As a result, it has been used in electrochemistry for testing new electrochemical techniques [9-11]. In this work, the ferro-ferricyanide redox couple was used as a model diffusion-controlled system to test the PMRS technique and to verify the theoretical principles discussed in Chapter 2.

4.1 Electrochemical Behaviour of a Reversible System

4.1.1 The principles of cyclic voltammetry

Cyclic voltammetry is an electrochemical technique used to provide mechanistic information about the system under study. A current-potential (*i-E*) profile is recorded and used as an "electrochemical spectrum" to identify the potentials at which electrochemical redox processes occur. The potential at an electrode surface is swept between two limits, E_1 and E_2, at a constant sweep-rate, ν, and then reversed back to E_1, generally at the same sweep-rate.

Let us consider the simple reversible electrode process $O + ne^- \rightleftharpoons R$ where only O is initially present in solution. The concentrations of O and R at the electrode surface are dependent on the potential applied, and the ratio of C_o/C_R is determined by the Nernst equation :

$$E = E^{o'} + \frac{RT}{nF} ln\left(\frac{C_O}{C_R}\right) \qquad (4.1)$$

where C_O=concentration of O

C_R=concentration of R

$E^{o'}$=formal potential

However, reduction of reactant O to product R, can only occur following its transport to the electrode / electrolyte interface. This process is termed the **mass transport** effect and is determined by three factors :

1. diffusion
2. convection
3. migration

For the purpose of this chapter we will limit the discussion to the effect of diffusion.

Diffusion occurs as a result of uneven concentration distributions in the electrolyte and can be predicted mathematically by Fick's laws. Fick's 1st law of diffusion states that :

$$J = -D_c\left(\frac{\partial[C]}{\partial x}\right) \qquad (4.2)$$

where J=diffusional flux

D_c=diffusion coefficient (dependent on the species involved)

C=general term to define the concentration of a species of interest e.g. O

Figure 4.1 illustrates the variation in concentration of *O* with distance *x* from the electrode / electrolyte interface [12].

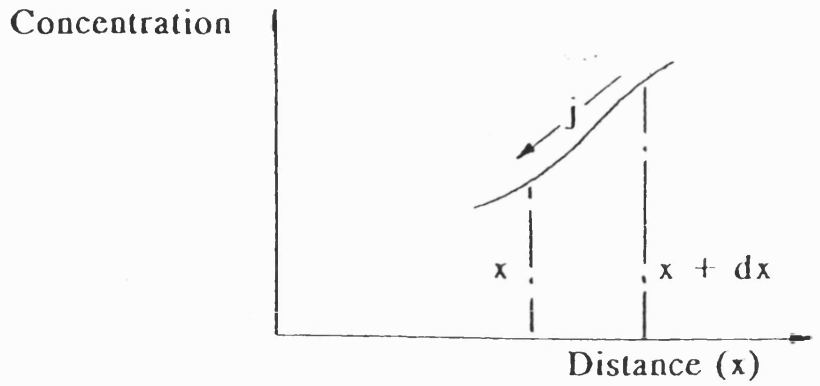

Figure 4.1 : The relationship between concentration of *O* with distance *x* from the electrode / electrolyte interface.

As a result of conversion of *O* to *R*, a lower concentration of *O* exists near the interface than in the bulk solution. This is accompanied by a higher concentration of *R* at the interface in relation to the bulk. Since the concentration of *O* decreases as *x* decreases, the diffusional flux *J* at a given point in the electrolyte is therefore proportional to the concentration gradient $-\frac{\partial[C]}{\partial x}$. The negative sign indicates the movement of reactant *O* from a region of high concentration to one of lower concentration.

Experimentally however, it is more important to consider the change in concentration at the electrode / electrolyte interface as a function of time. Fick's second law takes into account the change in flux of reactant *O* between a distance *x* and *x* + *dx* over time *dt*, as illustrated in **Figure 4.2**. Mass balance lead to the relationship :

$$[C]_{(x,t+dt)}\,Adx - [C]_{(x,t)}\,Adx = J_{(x,t)}\,Adt - J_{(x+dx,t)}\,Adt \qquad (4.3)$$

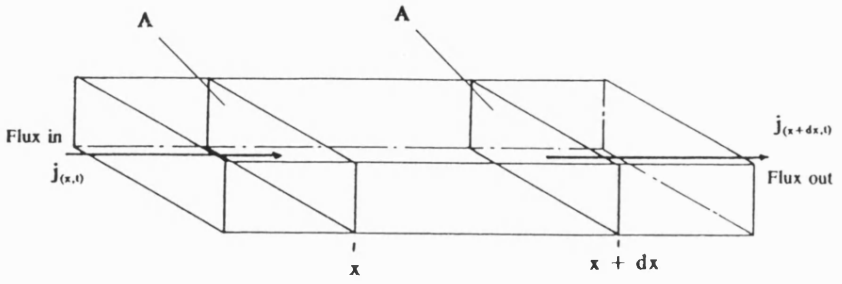

Figure 4.2 : Schematic of the flux of a species into and out of a zone bounded by two planes separated by a distance *dx* [12].

Rearrangement of Eq. (4.3) leads to Fick's 2nd law of diffusion which is defined as :

$$\frac{\partial[C]}{\partial t} = D_c\left(\frac{\partial^2[C]}{\partial x^2}\right) \tag{4.4}$$

The change in concentration with time is simply proportional to the change in the concentration gradient as a function of time.

Let us now consider the current-potential behaviour during a potential sweep between E_1 and E_2 and then back to E_1. **Figure 4.3** illustrates the potential-time profile. Note the sign convention. For a reduction process such as the redox couple $O + e^- \rightleftharpoons R$, the potential decreases in value from E_1 to E_2 i.e. becomes more cathodic. This is in contrast to the ferro-ferricyanide redox couple to be discussed later, which involves an oxidation process.

Figure 4.4 illustrates a typical cyclic voltammogram involving a reversible redox process. As the potential is sweep from E_1 towards E_2 the ratio C_O/C_R decreases as the

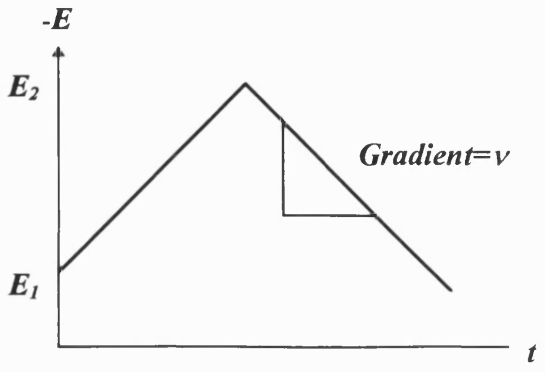

Figure 4.3 : A potential-time profile for cyclic voltammetry.

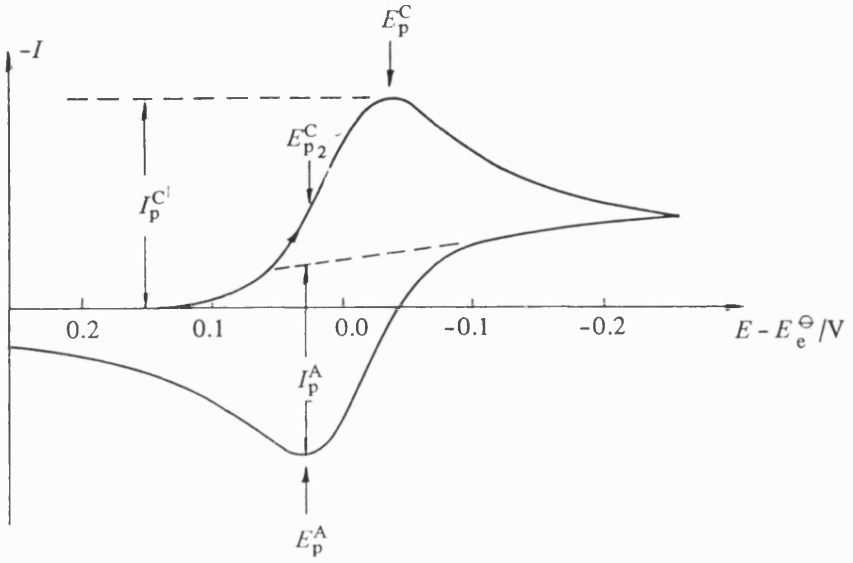

Figure 4.4 : A typical cyclic voltammogram for a reversible process, $O + e^- \rightleftharpoons R$.

surface reactant *O* is reduced to *R*. This is accompanied initially by an increase in the concentration gradient of *O*. The concentration gradient is the driving force for diffusion (according to Fick's 1st law), and as a result, the increasing gradient results in an increase in the current observed with potential. The current reaches a plateau as the concentration of *O* at the surface tends towards zero. At this potential, E_p, the concentration gradients start to decrease as the diffusion layer becomes wider, resulting in an decrease in current up to E_2. At potentials beyond E_p, the current response *i* is α $\frac{1}{\sqrt{t}}$, according to the cottrell equation :

$$i = \frac{nFAD^{1/2}[C]_{bulk}}{\pi^2 t^{1/2}} \qquad (4.5)$$

As the potential is reversed, R continues to be formed at the surface and a cathodic current is therefore still observed until the potential approaches $E^{o'}$. R is then reoxidised back to O and an anodic current is observed. This is accompanied by a decrease in the concentration of R at the surface until R=O. At this point a reverse current peak minimum is observed followed by a fall in current as observed for the forward sweep.

The separation of the anodic (E_p^A) and cathodic (E_P^C) peaks can be used as a diagnostic test for the reversibility of the redox process under study. The difference in potential of E_P and $E_{P/2}$ is also used. A summary of all the diagnostic tests is given in **Table 4.1**.

Diagnostic Tests
$\Delta E_p = E_p^A - E_p^C = 59/n$ mV
$E_P - E_{P/2} = 59/n$ mV
$j_P^A / j_P^C = 1$
$j_P \propto \nu^{1/2}$
E_P is independent of ν
at potentials beyond E_p, $j \propto t^{-1/2}$

Table 4.1 : Diagnostic tests for cyclic voltammograms of reversible redox processes.

4.1.2 The ferro-ferricyanide redox process

The ferro-ferricyanide redox couple has well-defined, reversible electrochemistry as illustrated conventionally in Eq. (4.6).

$$Fe(CN)_6^{3-} + e^- \rightleftharpoons Fe(CN)_6^{4-} \qquad E^o = 0.36V \qquad (4.6)$$

ferricyanide ferrocyanide

In this work, the reversible redox process is in fact studied i.e. oxidation of $[Fe(CN)_6]^{3-}$, to $[Fe(CN)_6]^{4-}$. The same electrochemical principles apply for $R \rightleftharpoons O + e^-$ as for the reverse process previously discussed. A 10^{-2}M solution of $[Fe(CN)_6]^{3-}$ was studied by cyclic voltammetry at a sweep-rate of $50mVs^{-1}$. A typical cyclic voltammogram is illustrated in **Figure 4.6**.

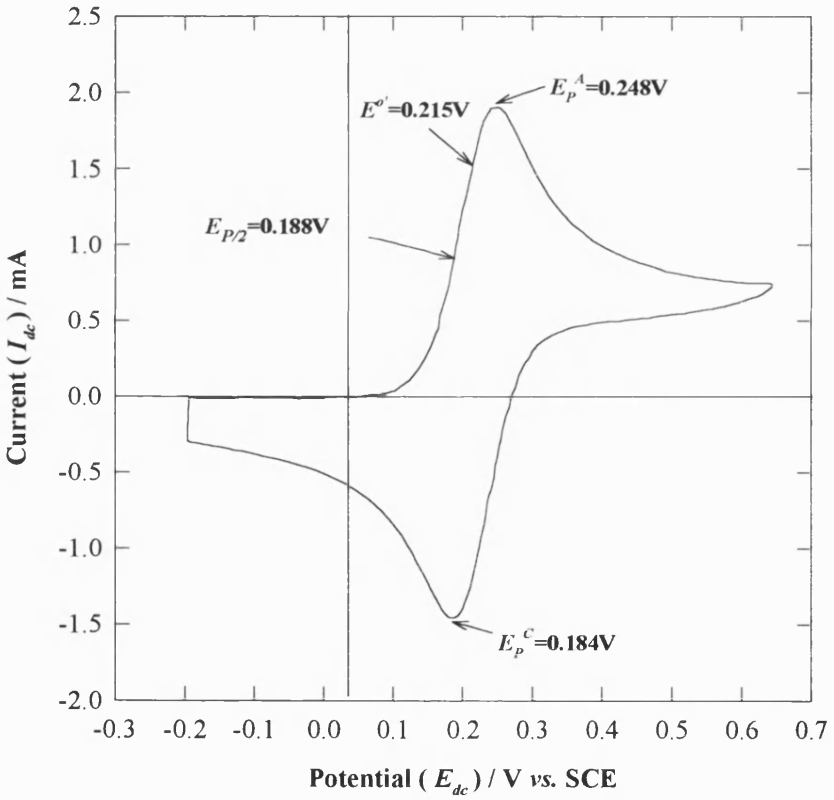

Figure 4.6 : Cyclic voltammogram of 10^{-2}M $[Fe(CN)_6]^{4-}$: Electrolyte=1M KF: Sweep-rate=50mV s^{-1}.

The potential separation of the cathodic and anodic peak, ΔE_p, is 64mV and E_P-$E_{P/2}$ is 60mV. Both values are in good agreement with the diagnostic value of 59mV for a reversible one electron process. The formal potential for the redox process is estimated from the values of E_P^A and E_P^C at $E^{0'}$=0.215V ±0.005V *vs.* SCE. The difference in value between the formal potential and the standard potential value in Eq. (4.6) is due to the dependence of $E^{0'}$ on concentration and nature of the supporting electrolyte [see e.g. 13,14].

4.2 PMR Spectroscopy

The absorption spectra for both $[Fe(CN)_6]^{3-}$ and $[Fe(CN)_6]^{4-}$ are illustrated in **Figure 4.7**. $[Fe(CN)_6]^{4-}$ has an absorption peak maximum at λ=323nm and does not absorb light at λ>400nm. $[Fe(CN)_6]^{3-}$ however has peak maxima at λ=420,303 and 260 nm together with a shoulder at 320nm.

A typical PMR spectrum for the ferro-ferricyanide redox couple is illustrated in **Figure 4.8**. The spectrum was recorded at $E_{dc}=E^{o'}$=0.215V at a frequency of modulation=9.5Hz and amplitude of modulation=26mV rms. Since E_{dc} corresponds to the formal potential for the redox couple, it follows that the PMR spectrum should be equivalent to a difference absorption spectrum of ferrocyanide and ferricyanide, where $C_{[Fe(CN)_6]^{4-}} = C_{[Fe(CN)_6]^{3-}}$. A difference absorption spectrum of 1:1 $[Fe(CN)_6]^{4-}$: $[Fe(CN)_6]^{3-}$ is superimposed on the PMR spectrum for comparison. A Gaussian shaped peak is observed with a maximum at λ=420nm, which is in excellent agreement with the difference spectrum. However, the peak maximum at λ=303nm is not resolved. This is attributed to the presence of $[Fe(CN)_6]^{3-}$ in the electrolyte. As the light beam passes through the electrolyte before reflection at the electrode surface, a large proportion of

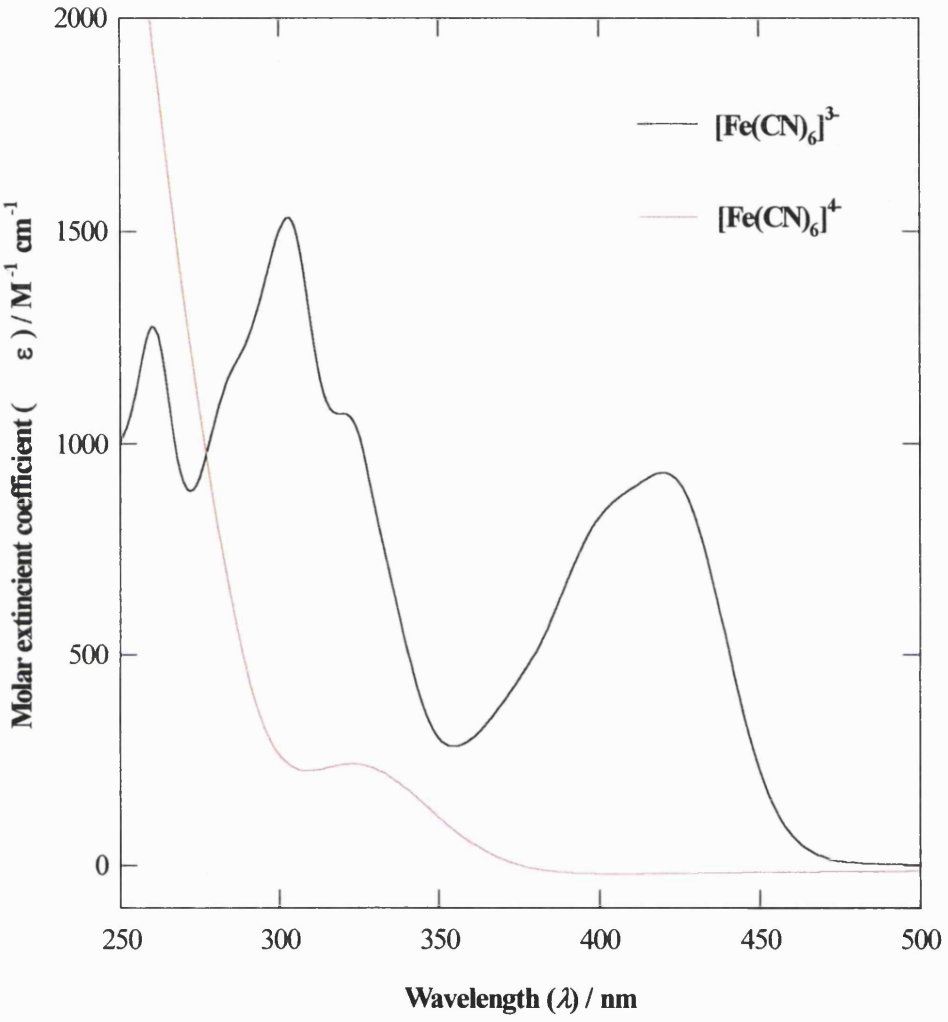

Figure 4.7 : Absorption spectra of $[Fe(CN)_6]^{4-}$ / $[Fe(CN)_6]^{3-}$. $C_{[Fe(CN)_6]^{4-}}$ =10^{-3}M; $C_{[Fe(CN)_6]^{3-}}$ =10^{-3}M; $C_{[KCl]}$=0.5M.

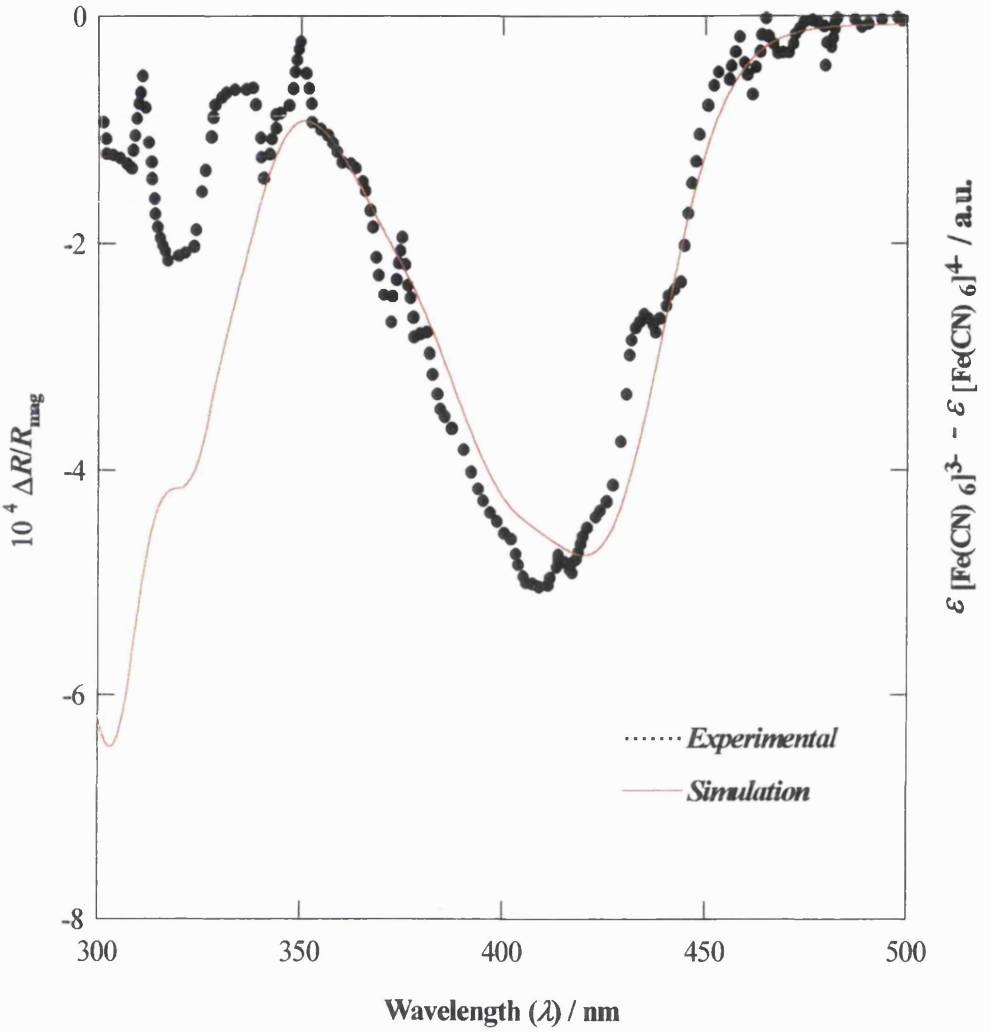

Figure 4.8 : PMR Spectrum of the $[Fe(CN)_6]^{4-}$ / $[Fe(CN)_6]^{4-}$ redox couple at E_{dc}=0.215V *vs.* SCE. $C_{[Fe(CN)_6]^{4-}} = C_{[Fe(CN)_6]^{3-}} = 10^{-3}$M; $C_{[KCl]}$=0.5M; F.M.=9.5Hz, E_o=26mV rms

the light is absorbed by $[Fe(CN)_6]^{3-}$, particularly in the wavelength regions 300-350 and 400-450nm (see absorption spectra in **Figure 4.7**). The intensity of the light beam and hence the value of R is therefore reduced considerably, so that $\Delta R/R$ is the ratio of two very small signals, resulting in a poor signal / noise ratio. This is particularly true in the low wavelength region i.e. 300-350nm where the intensity of the light beam is inherently low. The absorption of light by $[Fe(CN)]_6^{3-}$ over the range 300-350nm therefore prevents the detection of an optical response, which explains the discrepancy observed in **Figure 4.8**.

4.3 The relationship between *ac* and PMR voltammetry

A theoretical relationship has been derived between the *ac* voltammetric response and the potential dependent optical response in PMR voltammetry which is summarised below.

$$Re\left(\frac{\Delta R}{R}\right) = -\left(\frac{4.606\Delta\varepsilon}{nFA\cos\theta}\right) Im\left(\frac{Y_F}{\omega}\right) E_o = -k\frac{|Y_F|^2}{\omega}\left(\frac{1}{\omega}\right)^{1/2}\sigma \tag{4.7}$$

$$Im\left(\frac{\Delta R}{R}\right) = \left(\frac{4.606\Delta\varepsilon}{nFA\cos\theta}\right) Re\left(\frac{Y_F}{\omega}\right) E_o = k\frac{|Y_F|^2}{\omega}\left[R_{ct} + \left(\frac{1}{\omega}\right)^{1/2}\sigma\right] \tag{4.8}$$

where $$Y_F = \frac{n^2F^2A\omega^{1/2}D_o^{1/2}C_o^*}{4RT\cosh^2(a/2)} \tag{4.9}$$

$$k = \left(\frac{4.606\Delta\varepsilon}{nFA\cos\theta}\right) E_o \tag{4.10}$$

$$\sigma = \frac{4RT}{\sqrt{2}n^2F^2AD_o^{1/2}C_o^*}\cosh^2\left(\frac{a}{2}\right) \tag{4.11}$$

$$R_{ct} = \frac{RT}{n^2F^2Ak^oC_o^*} \tag{4.12}$$

$$a = \frac{nF}{RT}(E_{dc} - E^{o'}) \tag{4.13}$$

These derivations indicate that measurement of the PMR response can give direct access to the Faradaic admittance of the system under study and hence enable the evaluation of the kinetic parameters R_{ct} and σ. In this section, experimental results from *ac* voltammetry and PMR voltammetry will be presented to test the theoretical relationships derived.

4.3.1 *AC* voltammetry

The components of the *ac* admittance of the ferro-ferricyanide redox couple were recorded as a function of potential for a solution of 10^{-2}M $[Fe(CN)_6]^{4-}$ in 1M KF. The *ac* modulated signal had a frequency of modulation=9.8Hz and amplitude of modulation=14mV rms. The potential was scanned at 5mV s^{-1}. The potential dependent Faradaic *ac* admittance response is illustrated in **Figure 4.10**.

A typical bell-shaped voltammogram is observed for both the real and imaginary components with peak maxima of E=0.215V±0.005V. They are in excellent agreement with the formal potential $E^{o'}$ for the ferro-ferricyanide redox couple. The peak maximum for $Re(Y_F)$ is larger than $Im(Y_F)$ and a slight narrowing of the voltammogram is observed. This is an effect of the charge transfer resistance, R_{ct}, of the ferro-ferricyanide redox couple. This effect is simulated in **Figure 4.11**. At R_{ct}=0, the two components of the admittance response are equal in size and shape. As R_{ct} increases however, an increase in the $Re(Y_F)$ response and a slight narrowing of the voltammogram is observed. The $Im(Y_F)$ response is not affected by the value of R_{ct}.

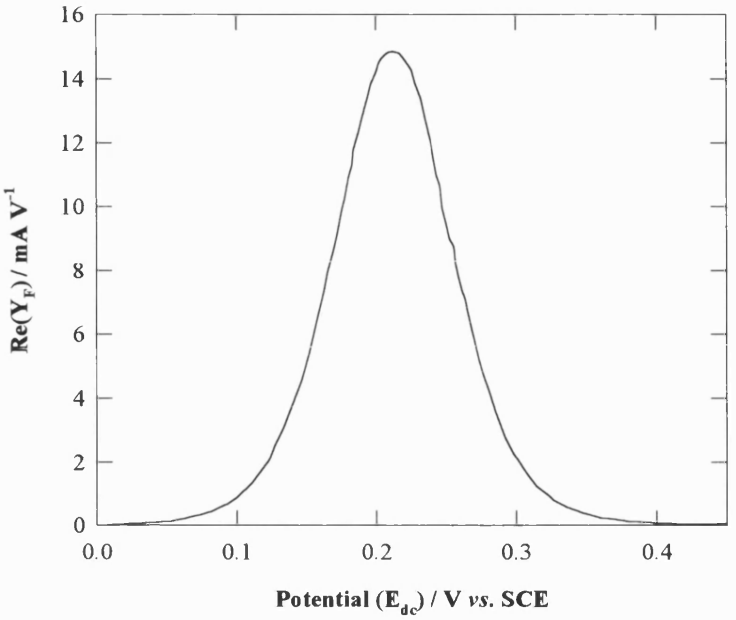

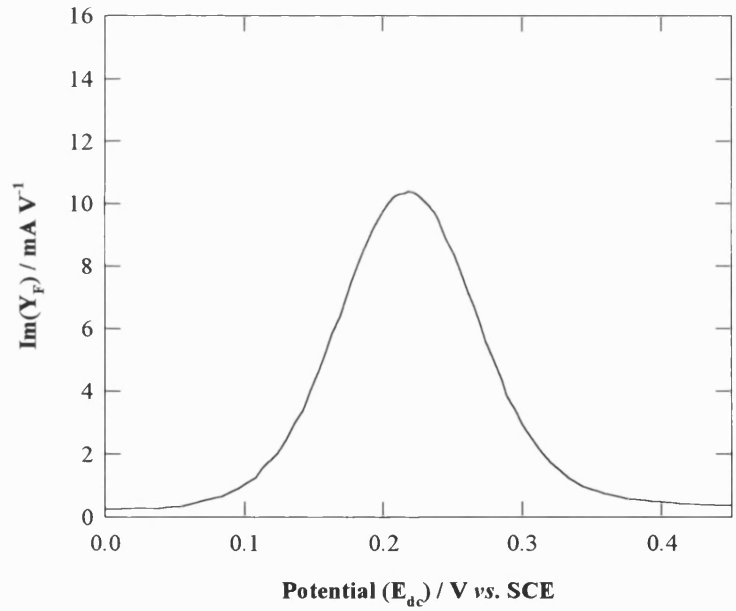

Figure 4.10 : Real and imaginary components of the Faradaic admittance as a function of potential. E_o=14mV rms; F.M.=9.8Hz; Scan-rate=5mVs^{-1}; $C_{[Fe(CN)_6]^{4-}}$ =10^{-2}M; $C_{[KF]}$=1M.

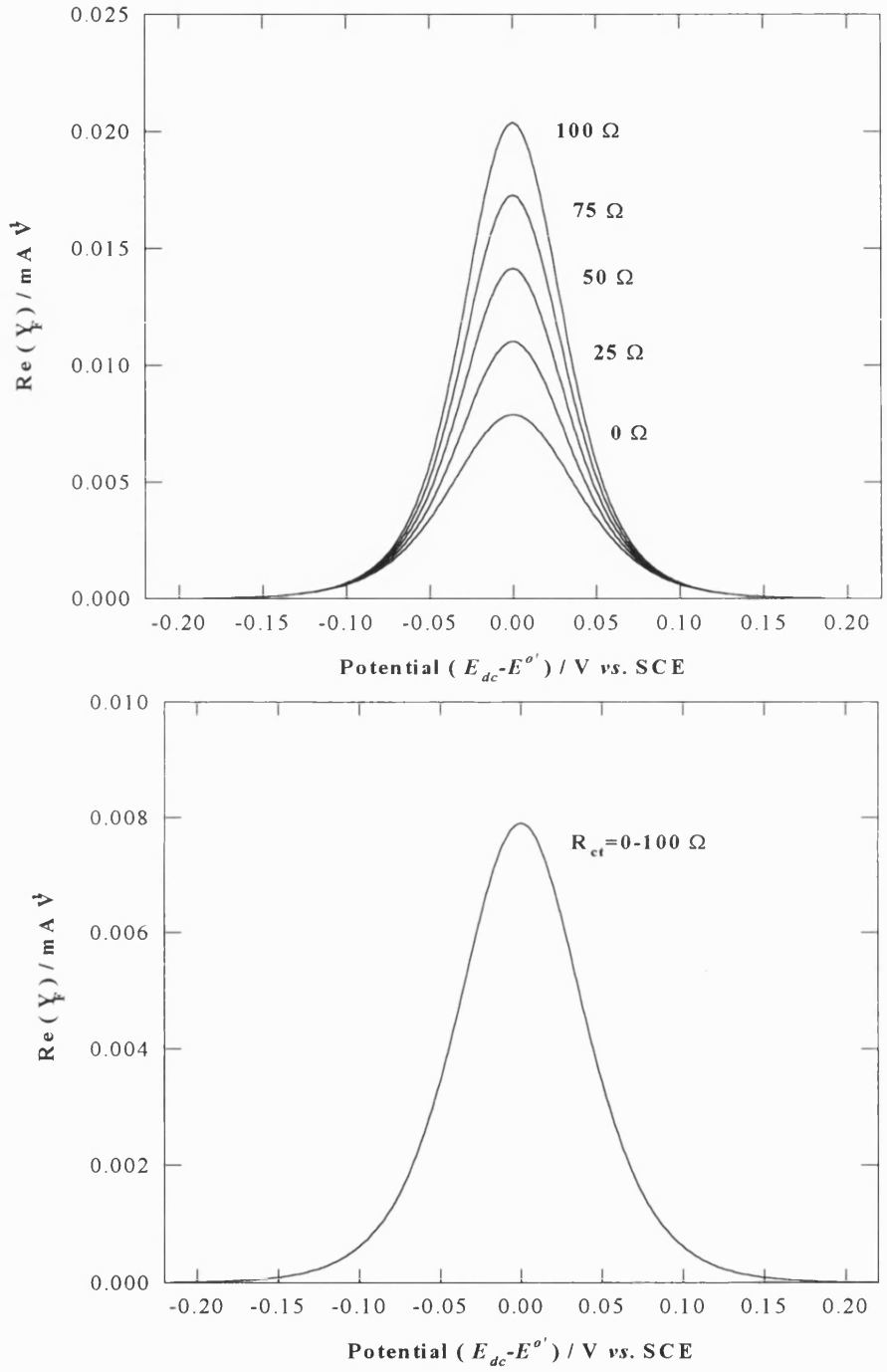

Figure 4.11 : Simulation of the effect of R_{ct} on the Faradaic admittance of the ferro-ferricyanide redox couple. $C_{[Fe(CN)_6]^{4-}}$ =10^{-2}M; $D_{[Fe(CN)_6]^{4-}}$ =6.50x10^{-6}cm^2 s^{-1}; $E^{o'}$=0.215V vs. SCE; E_o=14mV rms; F.M.=9.8Hz.

4.3.2 PMR voltammetry

The potential dependent PMR response of 10^{-2}M $[Fe(CN)_6]^{4-}$ in 1M KF was recorded under the same experimental conditions as for *ac* admittance at λ=440nm. The electrode surface was positioned at the centre of the electrochemical cell during the PMR voltammetry measurements. The problem of light absorption by the electrolyte (see **Figure 4.8**) is no longer applicable for PMR voltammetry since $[Fe(CN)_6]^{3-}$ is not initially present in solution.

From **Figure 4.12** it is seen that the real and imaginary components of the optical response have peak maxima at 0.215±0.005V. This value is in excellent agreement with the formal potential obtained from cyclic voltammetry and the peak maxima observed for the *ac* admittance results. The real and imaginary components of the optical response are opposite in sign, with a negative real component, as predicted by the theory. The imaginary component of the optical response has a larger peak maximum value than the real component. Comparison with the theoretical relationship between optical response and Faradaic response (Eq. (4.7) and Eq. (4.8)) suggests that this is an effect of the charge transfer resistance R_{ct}. Numerical simulation of the effect of R_{ct} on the real and imaginary components of the optical response is illustrated in **Figure 4.13**. This effect parallels that of the potential dependent *ac* admittance response and verifies the proposed theoretical relationships that $-Re\left(\frac{\Delta R}{R}\right) \alpha\ Im(Y_F)$ and $Im\left(\frac{\Delta R}{R}\right) \alpha\ Re(Y_F)$.

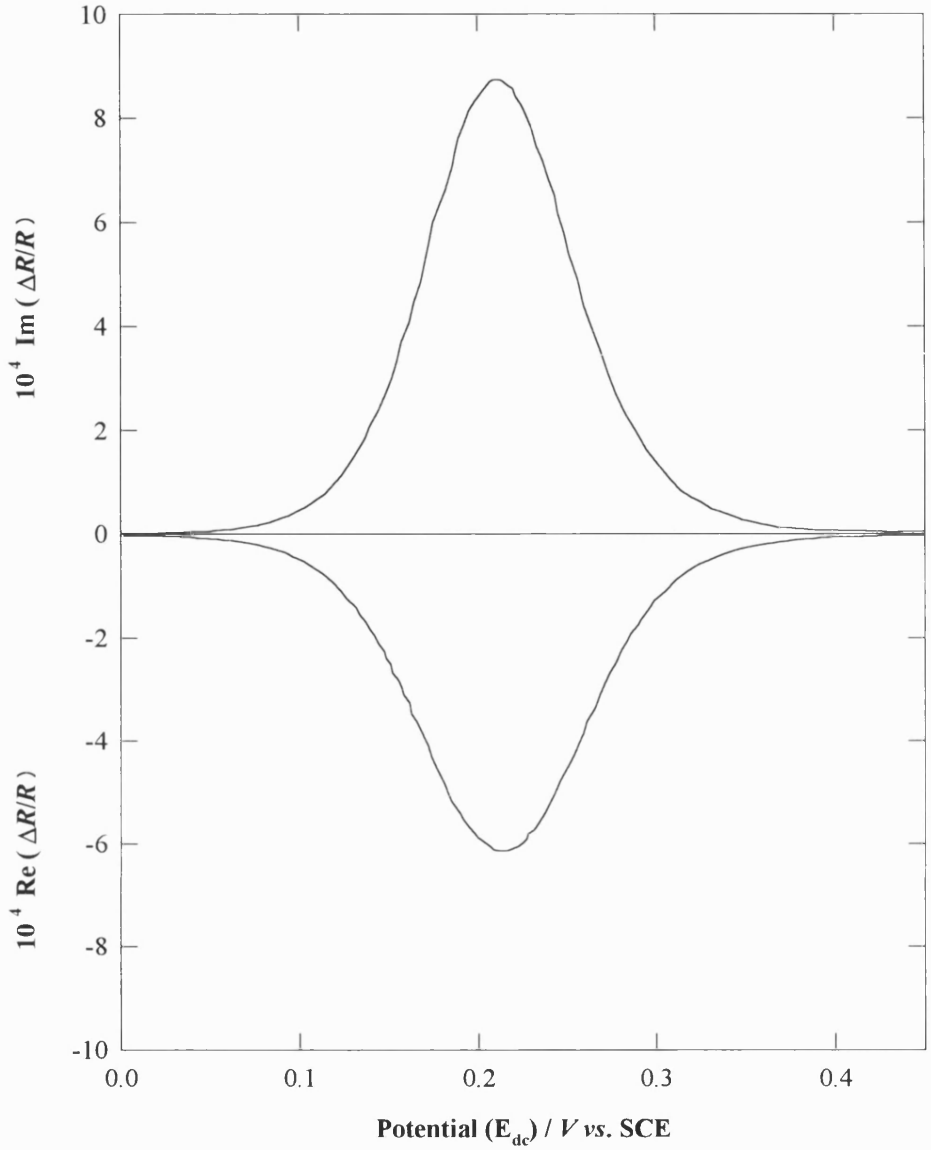

Figure 4.12 : The real and imaginary components of the optical response of the ferro-ferricyanide redox couple. $C_{[Fe(CN)_6]^{4-}}$ =10^{-2}M; $C_{[KF]}$=1M F.M.=9.8Hz, E_o=14mV rms, λ=440nm, Scan-rate=5mVs^{-1}.

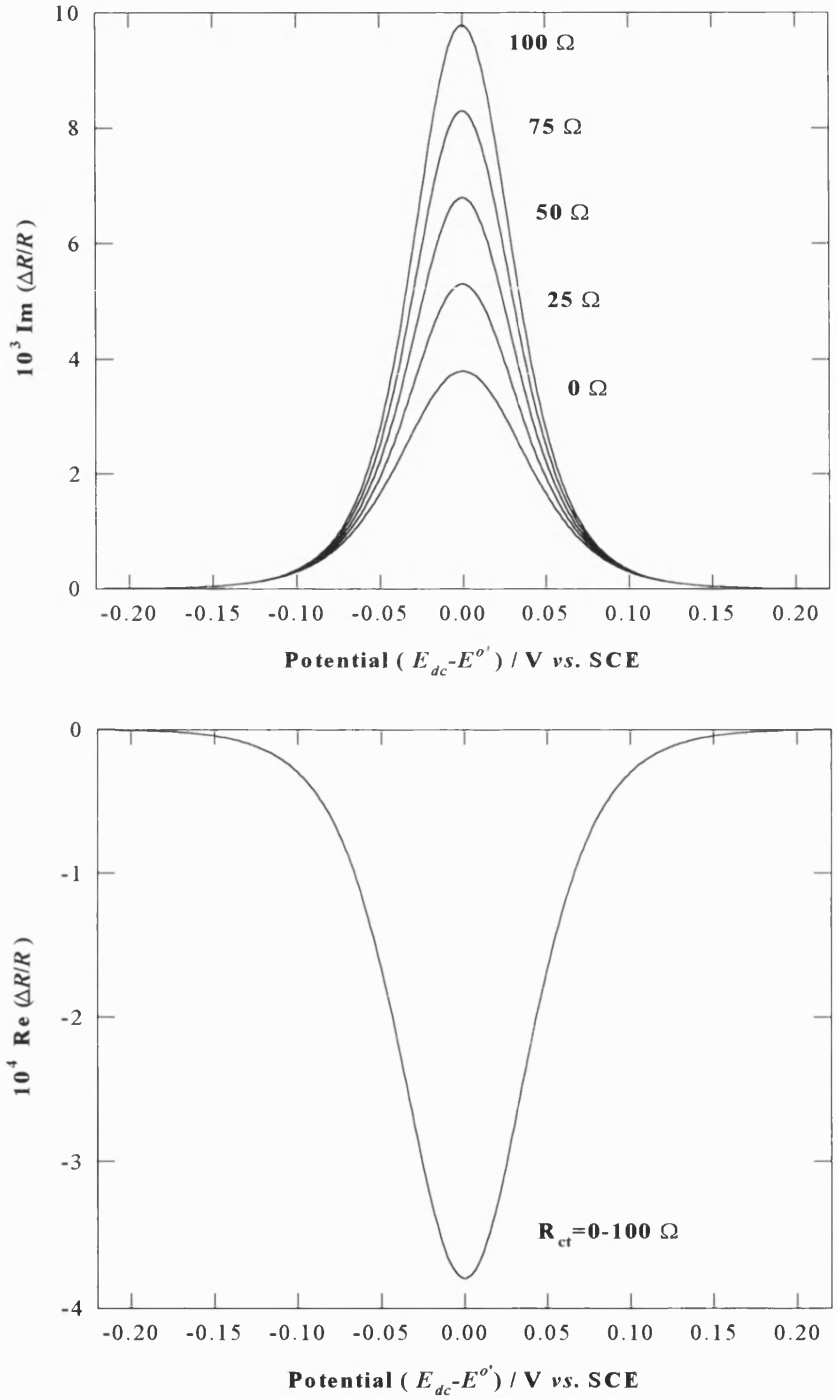

Figure 4.13 : Numerical simulation of the real and imaginary components of the optical response. C_o=10^{-2}M; F.M.=9.8Hz; E_o=14mV rms; ε=525 M^{-1} cm^{-1} (λ=440nm); A=0.149cm^2 ; D_o=6.5x10^{-6} cm^2 s^{-1}.

4.4 Frequency Response Analysis

Experimental results from Electrochemical Impedance Spectroscopy (EIS) and frequency dependent PMRS studies of the ferro-ferricyanide redox couple were used to verify the theoretical relationships derived between Faradaic admittance and the optical response. The kinetic parameters R_{ct} and σ were also determined from the optical response.

For all frequency response analysis studies, an equimolar solution of 10^{-3}M $[Fe(CN)_6]^{4-}/[Fe(CN)_6]^{3-}$ was used in 0.5M KCl electrolyte. Experiments were performed at the formal potential $E^{o'}$=0.215V and at an amplitude of modulation E_o=26mV rms.

4.4.1 Electrochemical Impedance Spectroscopy (EIS)

Figure 4.14 illustrates a typical impedance plot for the ferro-ferricyanide redox couple. A semi-circle is observed at high frequency with a straight line at the lower frequency range. This is in reasonable agreement with the theory for a simple reversible redox process involving soluble species. The intermediate region between the semi-circle and the linear Warburg response is non-ideal. This probably results from frequency dispersion in the double layer capacitance of platinum. The straight line has a slope of gradient 1.2, which is slightly higher than the theoretical value of 1. A theoretical fit of the high frequency semi-circle, as shown in **Figure 4.14b** enabled the resistance of solution, R_Ω to be evaluated. A value of R_Ω=16Ω was obtained, which corresponds to the intercept of the semi-circle of the impedance plot with the x-axis at the high frequency limit. An estimate of R_{ct}, which corresponds to the diameter of the semi-circle, is also possible and a value of R_{ct}=45Ω was obtained. However, this value was not considered to be accurate due to the non-ideal impedance response at intermediate frequency already discussed.

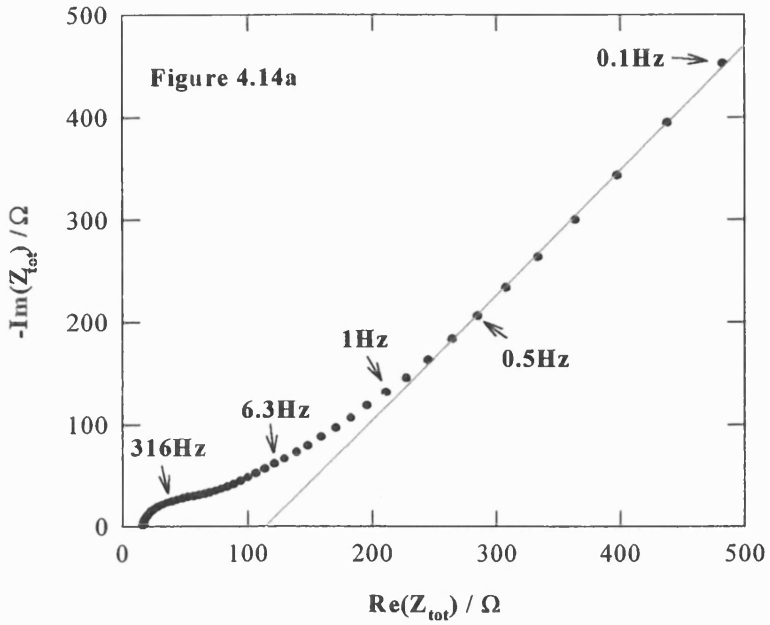

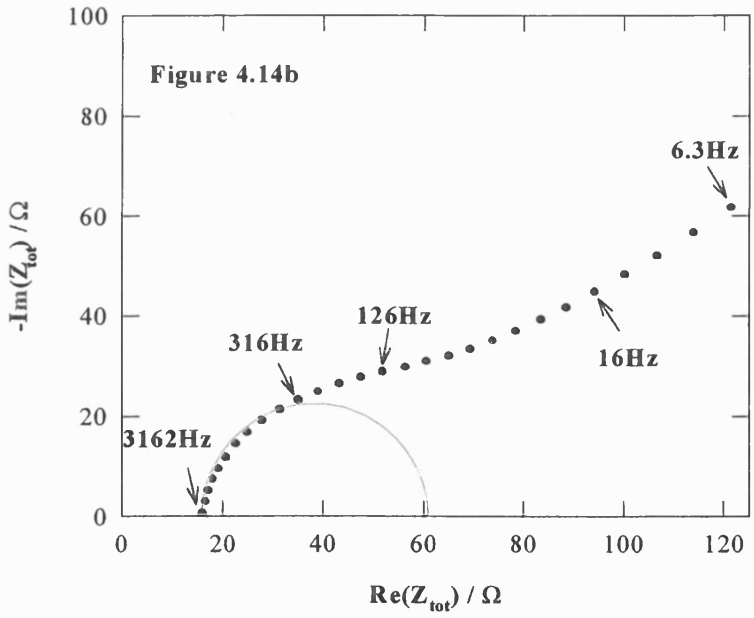

Figure 4.14 : Electrochemical impedance plot of the ferro-ferricyanide redox couple. E_{dc}=0.215V; E_o=26mV rms; $C_{[Fe(CN)_6]^{4-}} = C_{[Fe(CN)_6]^{3-}} = 10^{-3}$M; $C_{[KCl]}$=0.5M.

At the low frequency limit as $\omega \rightarrow 0$, the following relationships apply.

$$Re(Z_{tot})=R_{\Omega}+R_{ct}+\sigma\omega^{-1/2} \quad (4.14)$$

$$Im(Z_{tot})=\sigma\omega^{-1/2}+2\sigma^2C_{dl} \quad (4.15)$$

According to Eq. (4.14), a plot of $Re(Z_{tot})$ *vs* $\omega^{-1/2}$ should yield a straight line plot of gradient σ, with an intercept on the *y*-axis, $c=R_{\Omega}+R_{ct}$. Likewise, a corresponding plot of $-Im(Z_{tot})$ *vs* $\omega^{-1/2}$ should also yield a straight line plot of gradient σ, and intercept on the *y*-axis, $c=2\sigma^2C_{dl}$. The results for the limiting case, $\omega\rightarrow 0$ are illustrated in **Figure 4.15**. The plot of $Re(Z_{tot})$ vs. $\omega^{-1/2}$ yielded values for charge transfer resistance of $R_{ct}=61\Omega$ and $\sigma=325\Omega s^{-1/2}$. Values for the double layer capacitance of $C_{dl}=38\mu F\ cm^{-2}$ and $\sigma=329\Omega s^{-1/2}$ were also obtained from the plot of $Im(Z_{tot})$ *vs.* $\omega^{-1/2}$.

Knowledge of R_{Ω} and C_{dl} enables evaluation of the Faradaic impedance response of the ferro-ferricyanide redox couple. The relationship between Faradaic impedance and frequency is given by

$$Re(Z_F) = R_{ct} + \left(\frac{1}{\omega}\right)^{1/2}\sigma \quad (4.16)$$

$$-Im(Z_F) = \left(\frac{1}{\omega}\right)^{1/2}\sigma \quad (4.17)$$

Evaluation of the real and imaginary components of the Faradaic impedance response directly from the experimental total impedance components therefore enables the relationships discussed in Eq. (4.16) and Eq. (4.17) to be verified. Plots of $Re(Z_F)$ *vs.* $\omega^{-1/2}$ and $-Im(Z_F)$ *vs.* $\omega^{-1/2}$ as illustrated in **Figure 4.16** are linear, from which values for

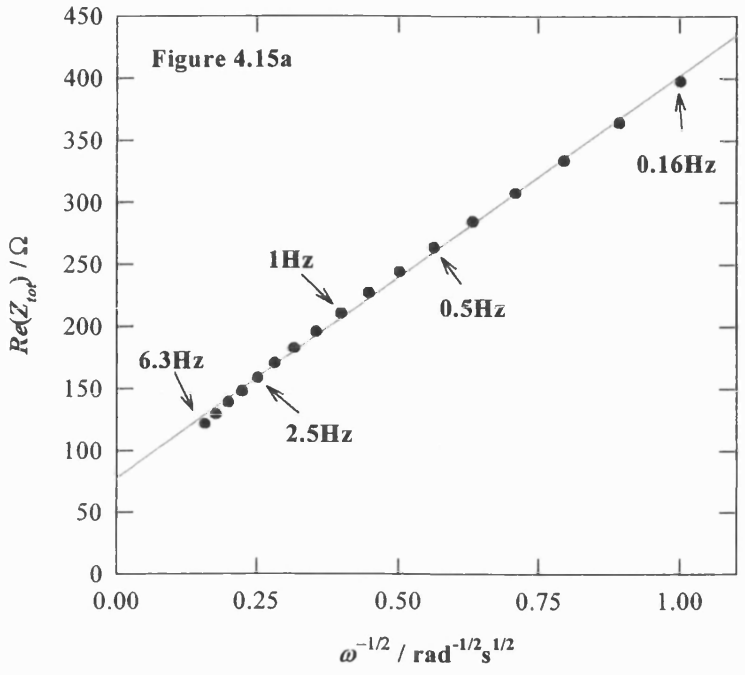

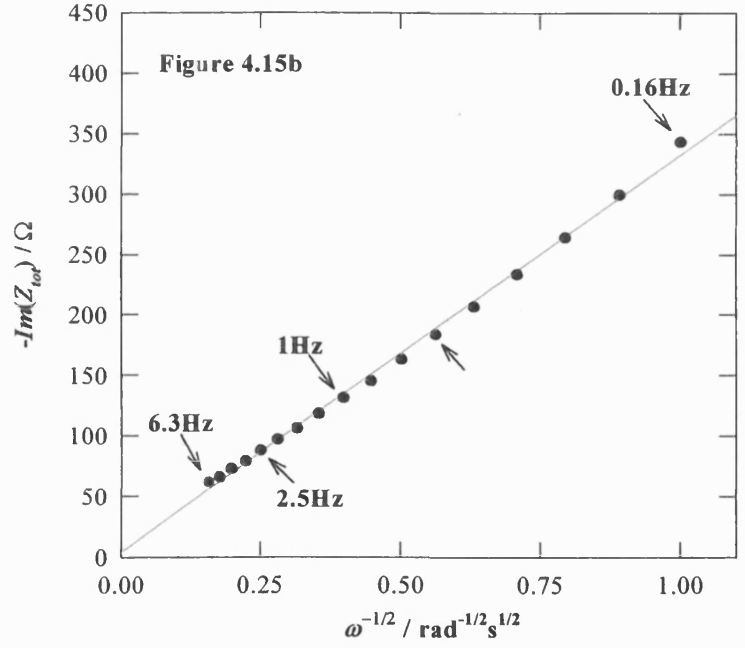

Figure 4.15 : Low frequency impedance response as a function of $\omega^{-1/2}$. E_{dc}=0.215V; E_o=26mV rms; $C_{[Fe(CN)_6]^{4-}} = C_{[Fe(CN)_6]^{3-}} = 10^{-3}$M; $C_{[KCl]}$=0.5M.

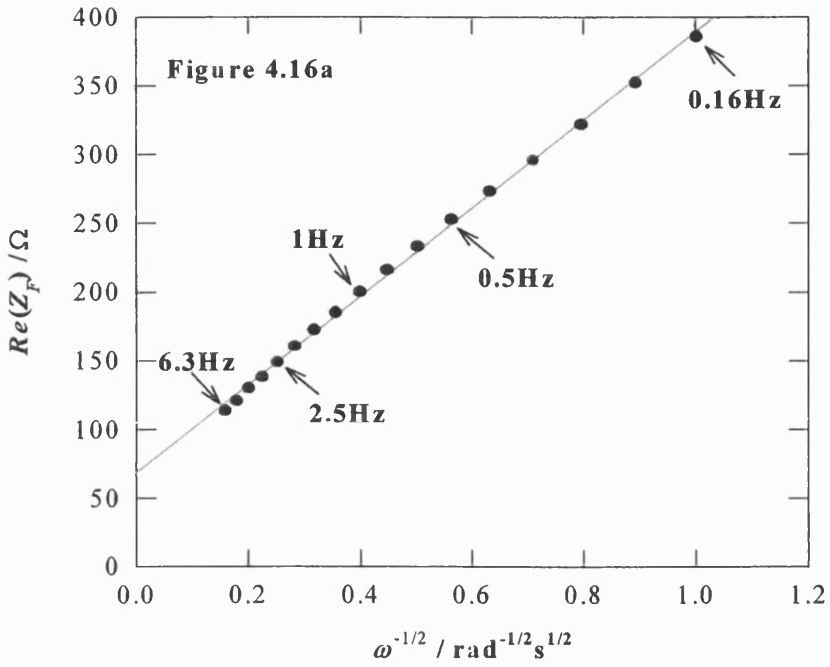

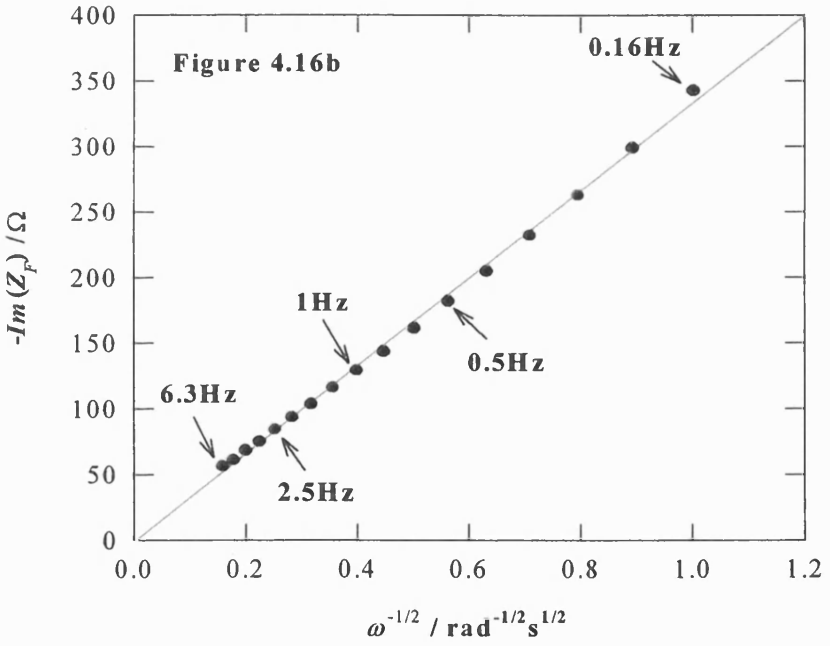

Figure 4.16 : Low frequency Faradaic impedance response as a function of $\omega^{-1/2}$. E_{dc}=0.215V; E_o=26mV rms; $C_{[Fe(CN)_6]^{4-}} = C_{[Fe(CN)_6]^{3-}} = 10^{-3}$M; $C_{[KCl]}$=0.5M; R_Ω=16Ω; C_{dl}=38μF cm^{-2}.

R_{ct}=68Ω and σ=321 and 334Ω $s^{-1/2}$ respectively have been derived. The values of the kinetic parameters obtained are summarised in **Table 4.2**.

$Re(Z_{tot})$ *vs.* $\omega^{-1/2}$	$-Im(Z_{tot})$ *vs.* $\omega^{-1/2}$	$Re(Z_F)$ *vs.* $\omega^{-1/2}$	$-Im(Z_F)$ *vs.* $\omega^{-1/2}$
R_{ct}=61Ω	C_{dl}=38μF cm^{-2}	R_{ct}=68Ω	σ=334Ω $s^{-1/2}$
σ=325Ω $s^{-1/2}$	σ=329Ω $s^{-1/2}$	σ=321Ω $s^{-1/2}$	

Table 4.2 : Kinetic parameters obtained from frequency dependent impedance studies.

The kinetic parameters R_{ct} and σ are defined as :

$$R_{ct} = \frac{RT}{n^2F^2Ak^oC} \tag{4.12}$$

$$\sigma = \frac{RT}{n^2F^2A\sqrt{2}}\left(\frac{1}{D_O^{1/2}C_O^*} + \frac{1}{D_R^{1/2}C_R^*}\right) \tag{4.18}$$

It is therefore possible to derive values for the experimental rate constant k. The average value of R_{ct}=65Ω from **Table 4.2**, yields a value for k=1.0 x10^{-2} cm s^{-1} , where the electrode geometric surface area=0.419cm^2 at T=298K and C_O^*=C_R^*=10^{-3} M. This experimental value can be compared to previous studies by Peter *et al.* [1] on the concentration dependence of cationic component of supporting electrolyte, i.e. KCl, on the experimental rate constant. The authors report a value of k=8.5 x10^{-2} cm s^{-1} for the same concentration of KCl in ultraclean solutions using a gold electrode, where C_O^*=C_R^*=5x10^{-3} M. It has been demonstrated by Peter *et al.*, that reproducibility of rate constant values to within a factor of ten is difficult unless ultraclean conditions are

applied. Our experimental value obtained at a Pt electrode is therefore deemed in excellent agreement with the value reported by Peter.

Using the reported literature values of D_O=6.5x10^{-6} and D_R=7.63x10^{-6} [15], a theoretical value for σ=339Ω s$^{-1/2}$ is also obtained. Our average value of σ=327 Ω s$^{-1/2}$ is therefore in excellent agreement with the theoretical value for our system.

4.4.2 PMRS-Frequency response analysis

According to the PMR theory derived for a diffusion-controlled process, the following relationships exists between the real and imaginary components of the optical response and the kinetic parameters R_{ct} and σ in the low frequency limit.

$$Re\left(\frac{\Delta R}{R}\right) = -\frac{k}{\sigma}\left(\frac{1}{\omega}\right)^{1/2} \tag{4.19}$$

$$Im\left(\frac{\Delta R}{R}\right) = \frac{k.R_{ct}}{2\sigma^2} + \frac{k}{\sigma}\left(\frac{1}{\omega}\right)^{1/2} \tag{4.20}$$

$$Im\left(\frac{\Delta R}{R}\right) = -Re\left(\frac{\Delta R}{R}\right) + \frac{k.R_{ct}}{2\sigma^2} \tag{4.21}$$

$$k = \left(\frac{4.606\Delta\varepsilon}{nFA\cos\theta}\right)E_o \tag{4.10}$$

Therefore a plot of $-Re\left(\frac{\Delta R}{R}\right) vs. Im\left(\frac{\Delta R}{R}\right)$ as a function of ω should yield a straight line plot of gradient=1 and intercept on the y-axis=$\frac{k.R_{ct}}{2\sigma^2}$ at the low frequency limit, whereas $Re\left(\frac{\Delta R}{R}\right)$ and $Im\left(\frac{\Delta R}{R}\right)$ should tend to zero at the high frequency limit. The

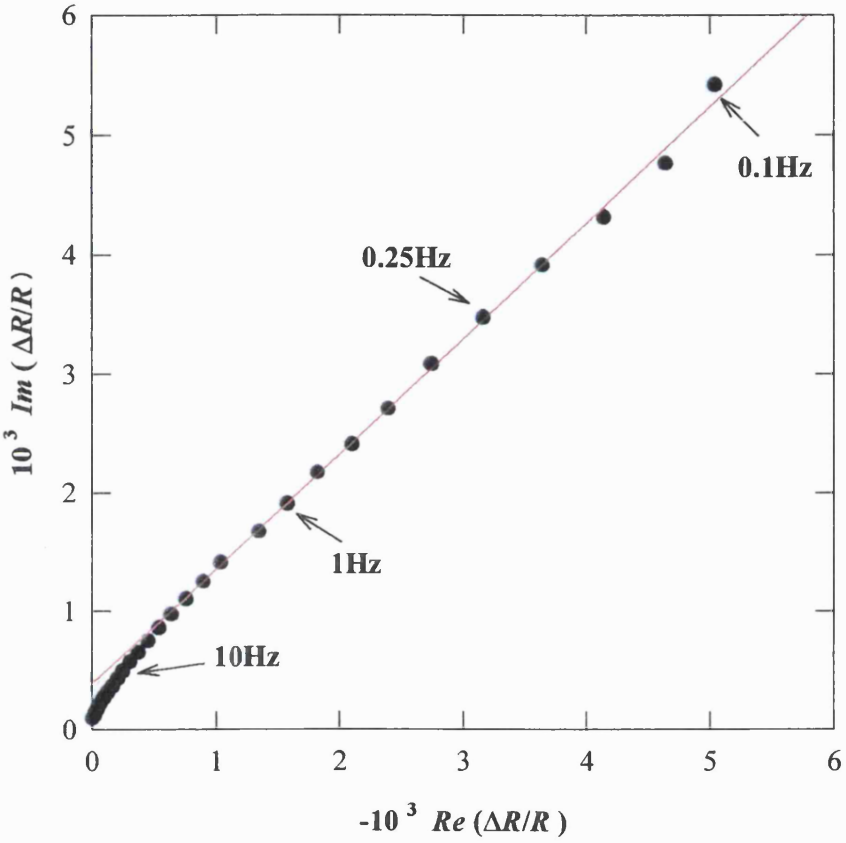

Figure 4.17 : Frequency dependent optical response of the ferro-ferricyanide redox couple. E_{dc}=0.215V; E_o=26mV rms; $C_{[Fe(CN)_6]^{4-}} = C_{[Fe(CN)_6]^{3-}} = 10^{-3}$M; $C_{[KCl]}$=0.5M.

experimental results for the ferro-ferricyanide redox couple in **Figure 4.17** are in excellent agreement with the theory. A linear regression fit of the low frequency optical response gives a slope of gradient=0.97 and intercept=$3.8\text{x}10^{-4}$. According to the realtionship given in Eq. (4.20), the intercept=$\frac{k.R_{ct}}{2\sigma^2}$. Use of the average R_{ct} and σ values obtained by EIS, therefore yields a value for the optical constant, k=1.25. This value can be compared to the numerical value obtained from the relationship in Eq. (4.10), $k=\left(\frac{4.606\Delta\varepsilon}{nFA\cos\theta}\right)E_o$=3.905, where A=0.419cm^2, $\Delta\varepsilon$=923 M^{-1} cm^{-1} and θ=45°. It is clear from Eq. (4.20) that the value of R_{ct} influences that of the optical constant, k. It has also been shown that the experimental rate constant evaluated from EIS is lower than that reported in the literature. It follows therefore, that the accompanying increase in R_{ct} from ideal ultraclean conditions, results in the lower optical constant, k reported here.

The bending of the slope at the high frequency limit is due to the finite value of R_{ct}. A numerical simulation of the optical response is illustrated in **Figure 4.18** to demonstrate the effect of R_{ct}. $Re\left(\frac{\Delta R}{R}\right)$ and $Im\left(\frac{\Delta R}{R}\right)$ over the frequency range 0.1-100 Hz were calculated according to Eq. (4.19) and (4.20). The theoretical value for σ=339 Ω s$^{-1/2}$, as calculated from Eq. (4.18), was used together with k=3.905 for the numerical simulation. The theoretical frequency dependent optical response is shown for R_{ct}=0 and R_{ct}=100 Ω. The influence of R_{ct} is such that the bending of the frequency dependent optical response increases and is accompanied by a decrease in the frequency range of linearity.

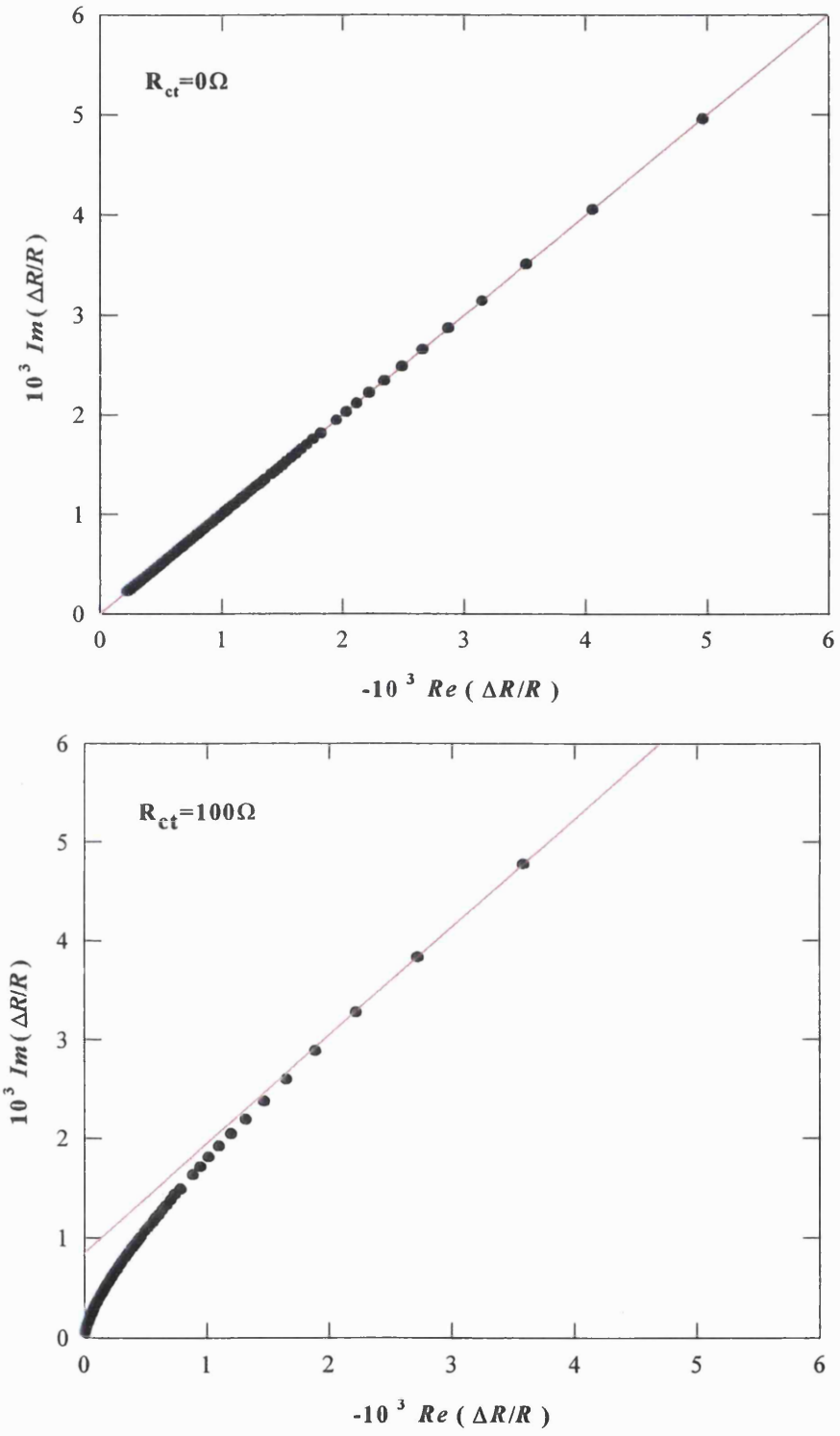

Figure 4.18 : Numerical simulation of the frequency dependent optical response : The effect of R_{ct}. R_{ct}=100Ω; σ=339Ω $s^{-1/2}$; ε=923M^{-1} cm^{-1}; A=0.419cm^2 (k=3.905).

4.4.3 Relationship between Faradaic impedance and the optical response

Knowledge of the experimental optical response and Faradaic impedance of the ferro-ferricyanide redox couple enables the theoretical relationship between the two to be verified. Rearrangement of the theoretical derivations in Eq. (4.7) and Eq. (4.8) gives

$$\frac{-Re\left(\frac{\Delta R}{R}\right)}{Im(Y_F)} = \left(\frac{4.606\Delta\varepsilon}{nFA\cos\theta}\right)\left(\frac{1}{\omega}\right)E_o \tag{4.22}$$

$$\frac{\mathrm{Im}\left(\frac{\Delta R}{R}\right)}{\mathrm{Re}(Y_F)} = \left(\frac{4.606\Delta\varepsilon}{nFA\cos\theta}\right)\left(\frac{1}{\omega}\right)E_0 \tag{4.23}$$

It follows that a plot of $\frac{-Re\left(\frac{\Delta R}{R}\right)}{Im(Y_F)}$ or $\frac{Im\left(\frac{\Delta R}{R}\right)}{Re(Y_F)}$ *vs.* ω^{-1} should give a straight line of gradient=k, which passes through the origin. **Figure 4.19** illustrates the relationship between the Faradaic admittance response (as derived from the experimental Faradaic impedance response) and optical response of the ferro-ferricyanide redox couple. Straight line plots are observed for both relations which pass through the origin, thus supporting the derived theoretical relationship. An average gradient of k=3.09 is obtained. For $\Delta\varepsilon$=932, E_o=26mV rms and θ=45°, the calculated value for k corresponds to 3.91. The value of k obtained from the relationships defined in Eq. (4.22) and Eq. (4.23) is in good agreement and therefore supports the theoretical relationship derived between an optical and Faradaic response. Discrepancies between the two values are attributed to possible errors in the evaluation of the geometric surface area of the electrode, and also in the angle of incidence of the light beam.

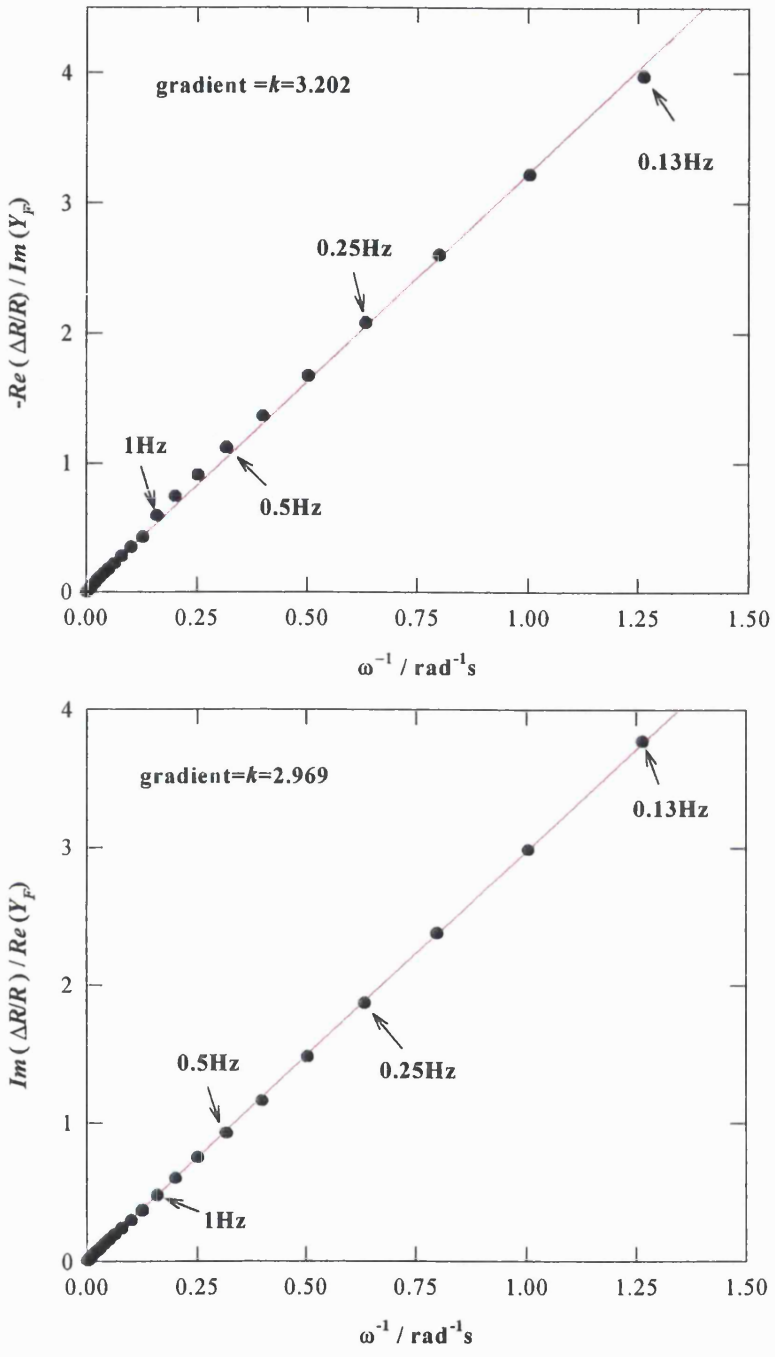

Figure 4.19 : Relationship between the optical response and Faradaic admittance of the ferro-ferricyanide redox couple. E_{dc}=0.215V; E_o=26mV rms; $C_{[Fe(CN)_6]^{4-}} = C_{[Fe(CN)_6]^{3-}} = 10^{-3}$M; $C_{[KCl]}$=0.5M.

Furthermore, evaluation of the kinetic parameters R_{ct} and σ is also possible. According to the theoretical relationships :

$$Re\left(\frac{\Delta R}{R}\right) = -k\frac{1}{|Z_F|^2\omega}\left(\frac{1}{\omega}\right)^{1/2}\sigma \tag{4.24}$$

$$Im\left(\frac{\Delta R}{R}\right) = k\frac{1}{|Z_F|^2\omega}\left[R_{ct} + \left(\frac{1}{\omega}\right)^{1/2}\sigma\right] \tag{4.25}$$

a plot of $-Re\left(\frac{\Delta R}{R}\right)\left(\frac{|Z_F|^2}{k}\right)$ *vs.* $\left(\frac{1}{\omega}\right)^{3/2}$ should give a straight line plot of slope=σ that passes through the origin. This relationship is confirmed in **Figure 4.20**. A slope of σ=350 Ω $s^{-1/2}$ was obtained. The value for σ is in excellent agreement with the values obtained by EIS.

The charge transfer coefficient R_{ct} can be evaluated by division of Eq. (4.24) by Eq. (4.25). This gives the following relationship :

$$-\frac{Im\left(\frac{\Delta R}{R}\right)}{Re\left(\frac{\Delta R}{R}\right)} = \frac{R_{ct}}{\sigma}\omega^{1/2} + 1 \tag{4.26}$$

A plot of $-\frac{Im\left(\frac{\Delta R}{R}\right)}{Re\left(\frac{\Delta R}{R}\right)}$ *vs.* $\omega^{1/2}$ should give a straight line plot of slope=$\frac{R_{ct}}{\sigma}$ and an intercept at the *y*-axis=1. This relationship is illustrated in **Figure 4.21**. A straight line plot is obtained which has a gradient=0.155 and intercept=0.90. Using σ=350Ω$s^{-1/2}$

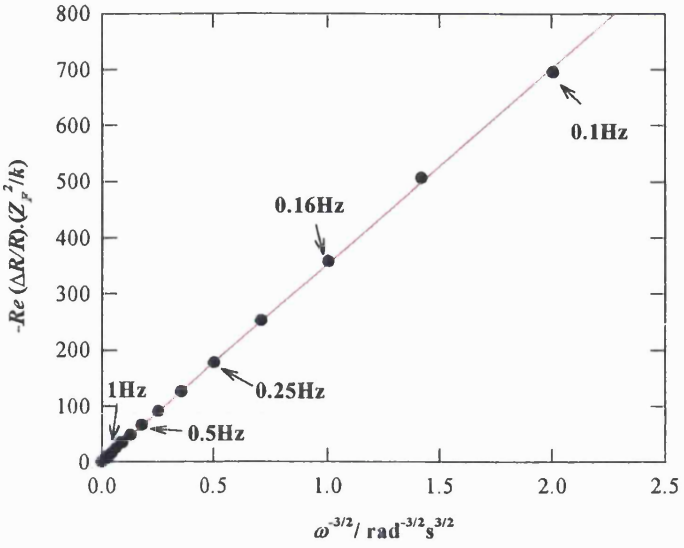

Figure 4.20 : Relationship between the optical response $Re(\Delta R/R)$ and Faradaic admittance Y_F. E_{dc}=0.215V; E_o=26mV rms; $C_{[Fe(CN)_6]^{4-}} = C_{[Fe(CN)_6]^{3-}} = 10^{-3}$M; $C_{[KCl]}$=0.5M.

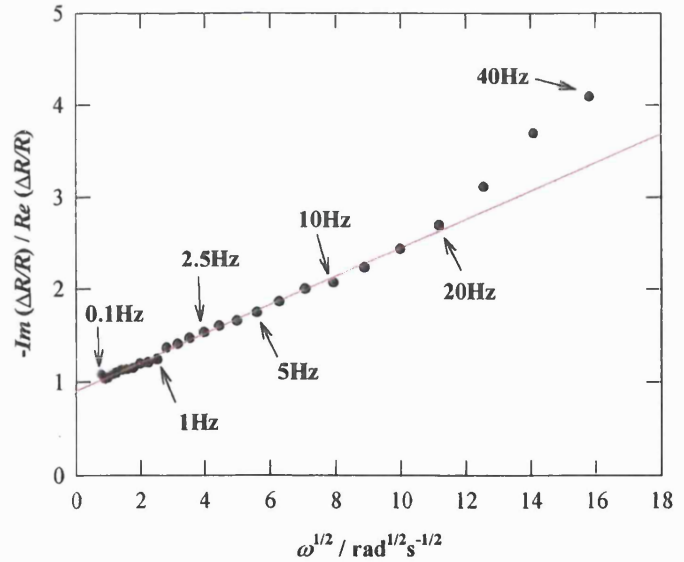

Figure 4.21 : Relationship between real and imaginary optical response. E_{dc}=0.215V; E_o=26mV rms; $C_{[Fe(CN)_6]^{4-}} = C_{[Fe(CN)_6]^{3-}} = 10^{-3}$M; $C_{[KCl]}$=0.5M.

obtained from the previous plot, this gives a value of R_{ct}=54Ω. Linear regression was performed up to 20Hz. The value for R_{ct} yields a value for the experimental rate constant, k=1.2 x10^{-2} cm s^{-1} which is in excellent agreement with the value obtained by impedance spectroscopy of 1.0 x10^{-2} cm s^{-1} (see section 4.4.1).

4.5 Discussion and Conclusions

The PMR study of the ferro-ferricyanide redox couple has enabled for the first time, the derived theoretical expression for the PMR optical response to be verified. The theory was based on an equivalent circuit for a reversible, diffusion-controlled process. As a result, a direct relationship between Faradaic admittance and frequency dependent optical response has been established.

The frequency dependent optical response has been correctly modelled for a diffusion controlled process. The complex plot of $Re\left(\frac{\Delta R}{R}\right)$ *vs.* $Im\left(\frac{\Delta R}{R}\right)$ for the ferro-ferricyanide redox couple resulted in a characteristic straight line, which can be used as a diagnostic for a diffusion-controlled process. The evaluation of kinetic parameters such as R_{ct} and σ has demonstrated that the frequency dependent optical response of a redox system is valuable as a complementary technique to impedance spectroscopy.

References

1. L.M. Peter, W. Dürr, P. Bindra and H. Gerischer, *J. Electroanal. Chem.*, **71**, 31 (1976)
2. M. Fleischmann, P.P. Graves and J. Robinson, *J. Electroanal. Chem.*, **182**, 87 (1985)
3. S. Pons, M. Datta, J.F. McAleer and A.S. Hinman, *J. Electroanal. Chem.*, **160**, 369 (1984)
4. P.A. Christensen, A. Hamnett and P.R. Trevellick, *J. Electroanal. Chem.*, **242**, 23 (1988)
5. H. Baltruschat, F. Lu, D. Song, S.K. Lewis, D.C. Zapien, D.G. Frank, G.N. Salaita and A.T. Hubbard, *J. Electroanal. Chem.*, **234**, 229 (1987)
6. K. Kumimatsu, Y. Shigematsu, K. Uosaki and H. Kita, *J. Electroanal. Chem.*, **262**, 195 (1989)
7. K. Winkler, *J. Electroanal. Chem.*, **388**, 151 (1995)
8. C. Beriet and D. Pletcher, *J. Electroanal. Chem.*, **361**(1-2), 93 (1993)
9. Z.H. Wang, M. Zhao and D.A. Scherson, *Anal. Chem.*, **66**(130), 1993 (1994)
10. Z.H. Wang, M. Zhao and D.A. Scherson, *Anal. Chem.*, **66**(24), 4560 (1994)
11. C.M. Pharr and P.R. Griffiths, *Anal. Chem.*, **69**(22), 4665 (1997)
12. A.C. Fisher, "*Electrode Dynamics*", Oxford Chemistry Series, Oxford Science Publications, p.14 (1996)
13. Southampton Electrochemistry Group, "Instrumental Methods in Electrochemistry", Ellis-Horwood, Chichester (1985)
14. A.J. Bard and L.R. Faulkner, "*Electrochemical Methods, Fundamentals and Applications*", Wiley & Sons, New York (1980)

15. M. Von. Stackelberg, M. Pilgrim and V. Toome, *Z. Elektrochem.*, **57**, 342 (1953)

Chapter 5

Chapter 5

Electrochemical and Spectroscopic Studies of the Anodic Behaviour of Ruthenium

5.1 Introduction

Ruthenium, a platinum group metal exhibits electrochemical behaviour which is markedly different to that of platinum, the most familiar platinum group metal. The electrochemistry of Ru is characterised by its strong affinity for oxygen, low overpotential for oxygen evolution and corrosive properties under highly anodic potentials [1-6].

Ru anodes have mainly been studied by cyclic voltammetry [7-11]. As a result of these studies, several mechanisms have been proposed for the electrochemistry of Ru between hydrogen and oxygen evolution. One such study by Lam *et al.*, [12] involved the electrochemistry of Ru-oxy species in alkali media using cyclic voltammetry, as an indirect method of characterising the surface reactions of Ru anode at different potentials. The authors suggested the following processes for the electrochemistry of Ru in alkali media which is consistent with other proposals [13-15].

$$2Ru + 3H_2O \rightleftharpoons Ru_2O_3 + 6H^+ + 6e^- \qquad E^o = 0.497 - 0.0591\ pH \qquad (5.1)$$

$$Ru_2O_3 + 2(OH^-) \rightleftharpoons 2RuO_2 + H_2O + 2e^- \qquad E^o = 0.696 - 0.0591\ pH \qquad (5.2)$$

$$RuO_2 + 4(OH^-) \rightleftharpoons RuO_4^{2-} + 2H_2O + 2e^- \qquad E^o = 1.764 - 0.1182pH + 0.295\log RuO_4^{2-} \qquad (5.3)$$

$$RuO_4^{2-} \rightleftharpoons RuO_4^- + e^- \qquad E^o = 0.349V \qquad (5.4)$$

$$RuO_4^- \rightleftharpoons RuO_4 + e^- \qquad E^o = 0.749V \qquad (5.5)$$

The proposed processes were based solely on available thermodynamic data and no direct identification of the proposed species involved was obtained.

This work uses the technique of PMRS, where electrochemical and spectroscopic information are combined, to provide unequivocal identification of the species involved in the electrochemistry of ruthenium.

5.2 Electrochemical and Spectroscopic study of Ru anodes in alkali media

5.2.1 Cyclic voltammetry

The cyclic voltammetric behaviour of Ru anodes is complex due to the strong affinity of Ru for oxygen [1]. Whereas a clearly defined voltammogram can be obtained for Pt at 100mV s^{-1}, Ru anodes demonstrate very broad cyclic voltammograms which are comparable to thermally prepared RuO_2 [4]. This observation is due to the strong affinity of Ru for oxygen and results in the formation of an oxide layer during the anodic sweep, which is not fully reduced during the cathodic sweep. Continuous multicycling of the Ru anode therefore results in the formation of a thick hydrous oxide overlayer [16,17] which prevents observation of the underlying electrochemistry of ruthenium.

This work is aimed at studying the electrochemistry of Ru anodes. The build-up of an oxide film at the anode by multicycling must be avoided. The study of Ru anodes at a slow sweep-rate allows the reduction of the anodic film during the cathodic sweep. This prevents oxide build-up and enables the electrochemistry of Ru metal to be observed. Throughout this chapter, all electrochemical and spectroscopic potential scans were performed at sweep-rates of 5-13mVs^{-1}.

A family of cyclic voltammograms of ruthenium in 0.1M NaOH at a sweep-rate of 13mV s^{-1} is shown in **Figure 5.1** . The anodic limit was increased progressively on each sweep and the electrode was held at the cathodic limit for approximately 1 minute to

allow complete reduction of the Ru surface between each sweep. This step-wise procedure enabled the stripping of the oxide layer during the cathodic sweep to be monitored more closely. Continuous multicycling was avoided in order to prevent formation of a thick hydrous oxide overlayer [16,17].

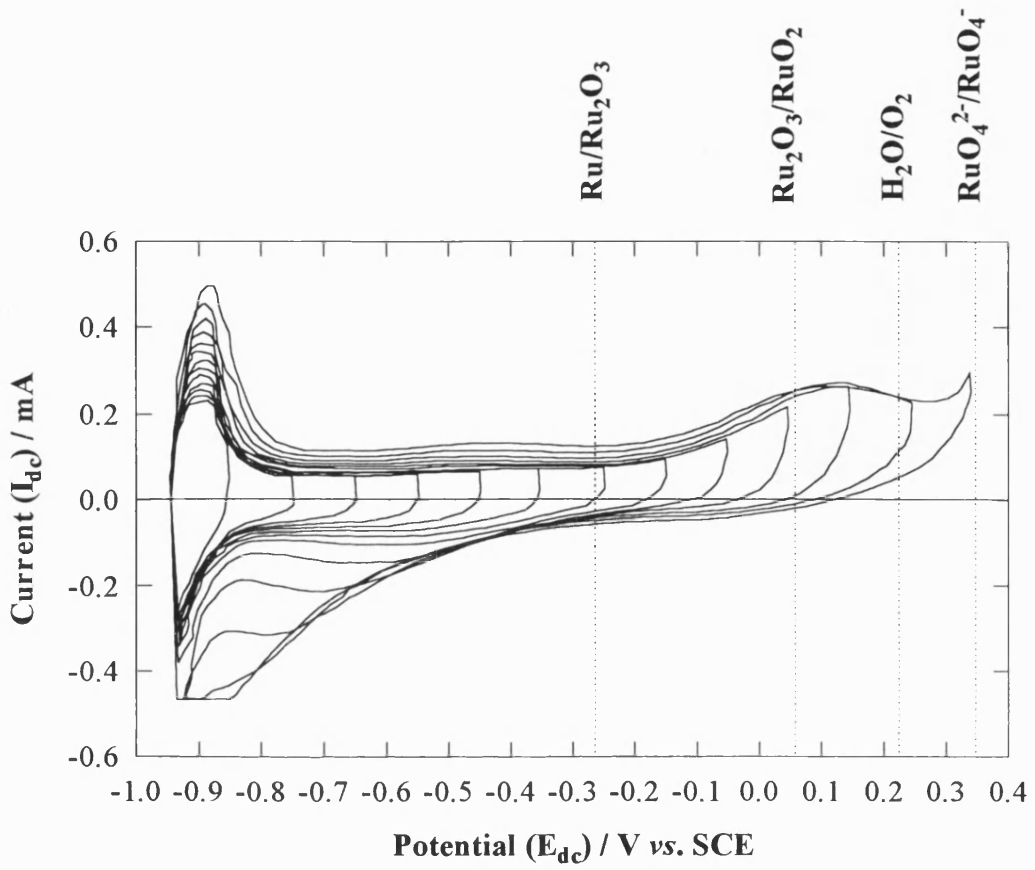

Figure 5.1 : Family of cyclic voltammograms for ruthenium in 0.1M NaOH. Scan-rate=13mV s^{-1}. The calculated equilibrium potentials for several relevant electrochemical processes are shown.

The shape of the family of voltammograms agrees well with the work of Hädzi-Jordanov *et al.* [10] who carried out a detailed study on the growth of oxide films on electrodeposited ruthenium electrodes. The cyclic voltammogram has several key

features which are consistent with previous work in this area [7-11].

1. A hydrogen adsorption and desorption region is resolved between -0.95 and -0.80V.

2. A broad surface oxidation region between -0.75 and -0.25V.

3. A pronounced surface oxidation peak between -0.20 and 0.30V.

4. Oxygen evolution occurs at >0.35V.

5. Hysteresis between oxide formation and reduction is indicative of irreversible oxide film formation.

Equilibrium potentials for a number of relevant reactions (calculated from data in [21] for pH=12.9 and expressed *vs.* SCE) are listed below. The Pourbaix diagram for Ru is also illustrated in **Figure 5.2**.

$$Ru_2O_3 + 6H^+ + 6e^- \rightleftharpoons 2Ru + 3H_2O \qquad E=0.265V \qquad (5.6)$$

$$2RuO_2 + 2H^+ + 2e^- \rightleftharpoons Ru_2O_3 + H_2O \qquad E=0.066V \qquad (5.7)$$

$$RuO_4^{2-} + 4H^+ + 2e^- \rightleftharpoons RuO_2 + 2H_2O \qquad E=0.239V + 0.0295\log[RuO_4^{2-}]V \qquad (5.8)$$

$$RuO_4^- + 4H^+ + 3e^- \rightleftharpoons RuO_2 + 2H_2O \qquad E=0.275\ V + 0.0197\log[RuO_4^-]V \qquad (5.9)$$

$$RuO_4^- + e^- \rightleftharpoons RuO_4^{2-} \qquad E=0.349\ V + 0.059\log[RuO_4^-/RuO_4^{2-}]V \qquad (5.10)$$

$$RuO_4 + 4H^+ + 4e^- \rightleftharpoons RuO_2 + 2H_2O \qquad E=0.384\ V \qquad (5.11)$$

$$RuO_4 + e^- \rightleftharpoons RuO_4^- \qquad E=0.709 - 0.059\log[RuO_4^-]V \qquad (5.12)$$

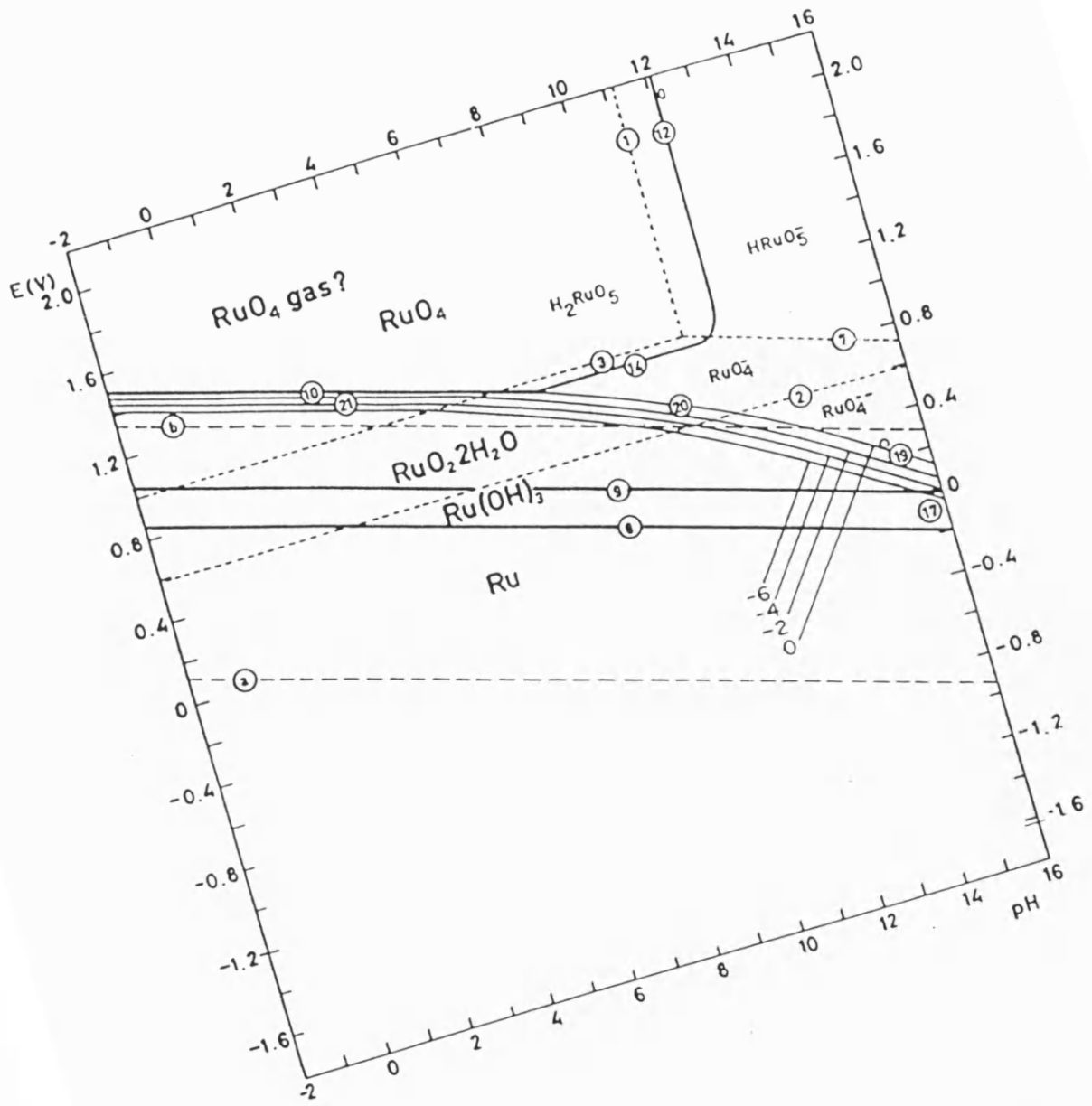

Figure 5.2 : Potential-pH diagram for the Ru-H_2O system at 25°C [18].

The equilibrium potentials of reactions 5.6, 5.7 and 5.10 are shown in **Figure 5.1** in order to identify the potential regions in which the corresponding transformations are thermodynamically feasible. Uncertainties exist as to the exact surface oxide process that occurs between -0.75 and-0.25V. It has been attributed to the oxidation of hydrogen adsorbed on ruthenium and possible adsorption of O / OH^- on the ruthenium surface [7]. Hysteresis in the voltammogram does suggest rearrangement of the surface oxide layer to a more stable structure as the anodic potential is increased. This effect supports the proposal [12-14] that an oxide of intermediate stoichiometry e.g. Ru_2O_3 is formed which is then oxidised further to RuO_2. It should be noted however, that Ru_2O_3 has not been identified in the anodic film.

The irreversible transformation of the surface oxide at potentials more positive than -0.2 V corresponds to the growth of RuO_2 [10]. The corrosion of the RuO_2 layer to form RuO_4^{2-} and RuO_4^- is not evident in the voltammogram since it is masked by the onset of oxygen evolution.

5.2.2 PMR Spectroscopy

PMR spectra were recorded using unpolarized light in the wavelength region between 300 and 600nm at constant potential. The *ac* modulation frequency was 9.5Hz and the amplitude was 50mV rms. In order to ensure reproducible surface conditions, the following protocol was used. The ruthenium plated electrode was first cycled twice at 13 mV s^{-1} between -0.95 and +0.35V *vs.* SCE and then held at the cathodic limit until no reduction current was observed. The potential was then swept at 13mVs^{-1} to the final constant potential at which PMR spectra were recorded.

In order to fully interpret the PMR spectra obtained for Ru, it is first necessary to look at the UV-Vis absorption data available for Ru-oxy species that could be involved

in the electrochemistry of Ru. **Figure 5.3** presents absorption spectra taken from the data reported by Connick and Hurley for several higher valent ruthenium species in alkali media [19]. In addition to the characteristic absorbance peaks for RuO_4^{2-} [Ru(VI)], RuO_4^- [Ru(VII)] and RuO_4 [Ru(VIII)], the spectra indicate that the RuO_4^{2-} / RuO_4^- couple should exhibit an isosbestic point at 415nm. **Table 5.1** summarises the spectroscopic information available for a range of Ru-oxy species.

PMR spectra were recorded for ruthenium in 0.1M NaOH at a series of potentials in the range 0.30 - 0.40V, the region where appearance and interconversion of RuO_4^{2-} and RuO_4^- is expected according to **Figure 5.2**. The PMR spectra obtained at 0.30, 0.35 and 0.40V are illustrated in **Figure 5.4**. Note that the spectra are bipolar, as expected for a difference spectrum arising from the modulation of the concentration of two species that absorb in the same wavelength region. The real and imaginary components of the $\Delta R/R$ signal were recorded, and it is the imaginary component of the $\Delta R/R$ signal which is shown here. It is interesting to note that the real component of the $\Delta R/R$ signal has the same features and sign as the imaginary component for all potentials. This is in contrast to the PMR response of the ferro-ferricyanide redox couple, which was used to model the PMR theory of a solution process. In that study (see Chapter 4), the real and imaginary components were opposite in sign. This suggests that the electrode process is more complex than the simple reversible redox process discussed in the theory. See Section 5.2.4 for a discussion of the frequency dependence of $\Delta R/R$ for this system.

The spectrum recorded at 0.30V exhibits a peak at 470nm that corresponds well to the peak in the absorption spectrum of RuO_4^{2-} [Ru(VI)] (*cf.* **Figure 5.3**). Two smaller peaks of equal magnitude and opposite sign can be seen at 385 and 320nm, and these can be assigned to RuO_4^- [Ru(VII)]. These peaks are more clearly defined in the spectrum recorded at 0.35V. The zero crossing point in the spectra is at 420nm, which

corresponds to the isosbestic point expected for the RuO_4^- / RuO_4^{2-} system on the basis of the absorption spectra reported by Connick and Hurley [19] and shown in **Figure 5.3**. The three peaks are also clearly defined in the PMR spectrum recorded at 0.40V, although the peak at 470nm is now smaller and the isosbestic point has shifted to 430nm.

The PMR data shown in **Figure 5.4** have been fitted to difference spectra calculated from the absorbance data of Connick and Hurley. The fact that the crossover point in the PMR spectrum is potential dependent was taken as evidence that mass balance does not apply to the concentration of RuO_4^{2-} and RuO_4^-. This is not unexpected since the system is clearly more complicated than a two component redox couple due to the generation of higher valent species by oxidation of the RuO_2 system. It was therefore assumed that the concentrations of the two oxyanion species could be varied independently to generate a fit. The results show that satisfactory agreement is obtained at all three potential values and that the shift in the crossover point is modelled correctly. The cause of the deviation at short wavelengths at more anodic potentials is not clear at this stage. However, it is not due to RuO_4 formation, since this should increase the response, not decrease it.

The electrochemistry of Ru in the potential region -0.75 - 0.25V where surface oxidation is prominent was also studied using PMR spectroscopy. No meaningful spectra were obtained.

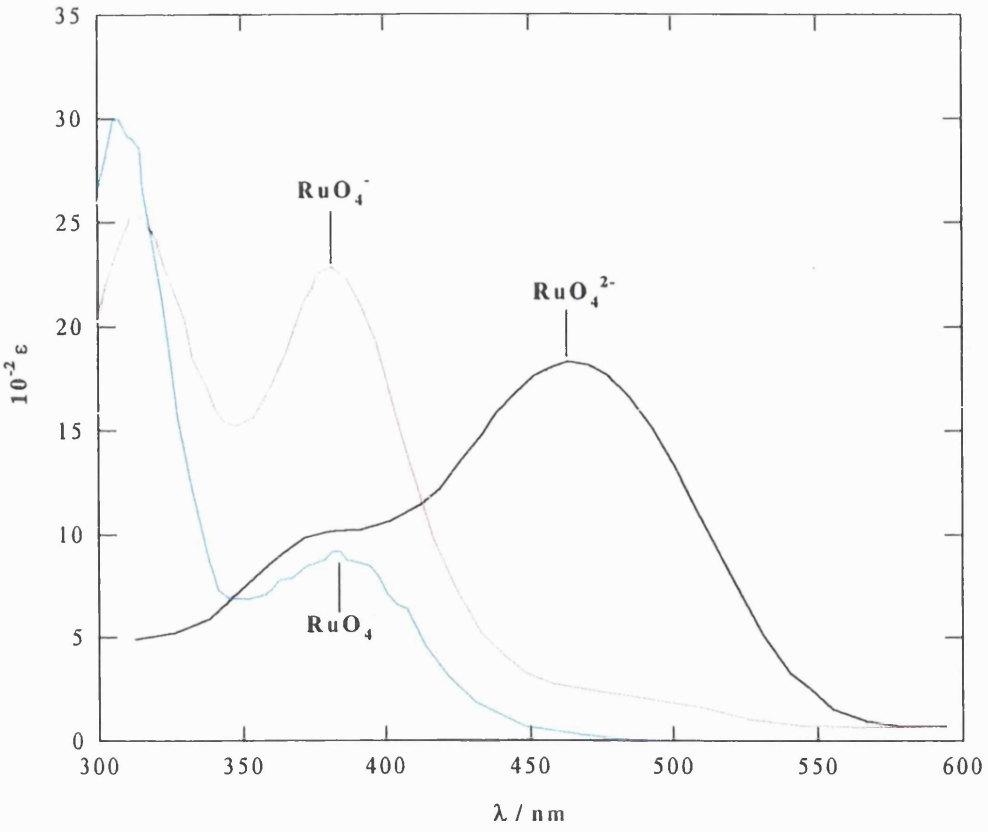

Figure 5.3 : Absorption spectra for ruthenium-oxy species (data taken from Ref. 19).

Ru-oxy species	*Peak maxima in absorption spectra*	*Reference*
Ru_2O_3 [Ru(III)]	No data available	
RuO_2 [Ru(IV)]	No data available	
RuO_4^{2-} [Ru(VI)]	470nm, shoulder peak at 385nm	[19-21]
RuO_4^- [Ru(VII)]	317, 385nm	[19-21]
RuO_4 [Ru(VIII)]	250, 308, 385nm	[17,22]

Table 5.1 : Summary of spectroscopic information for various Ru-oxy species.

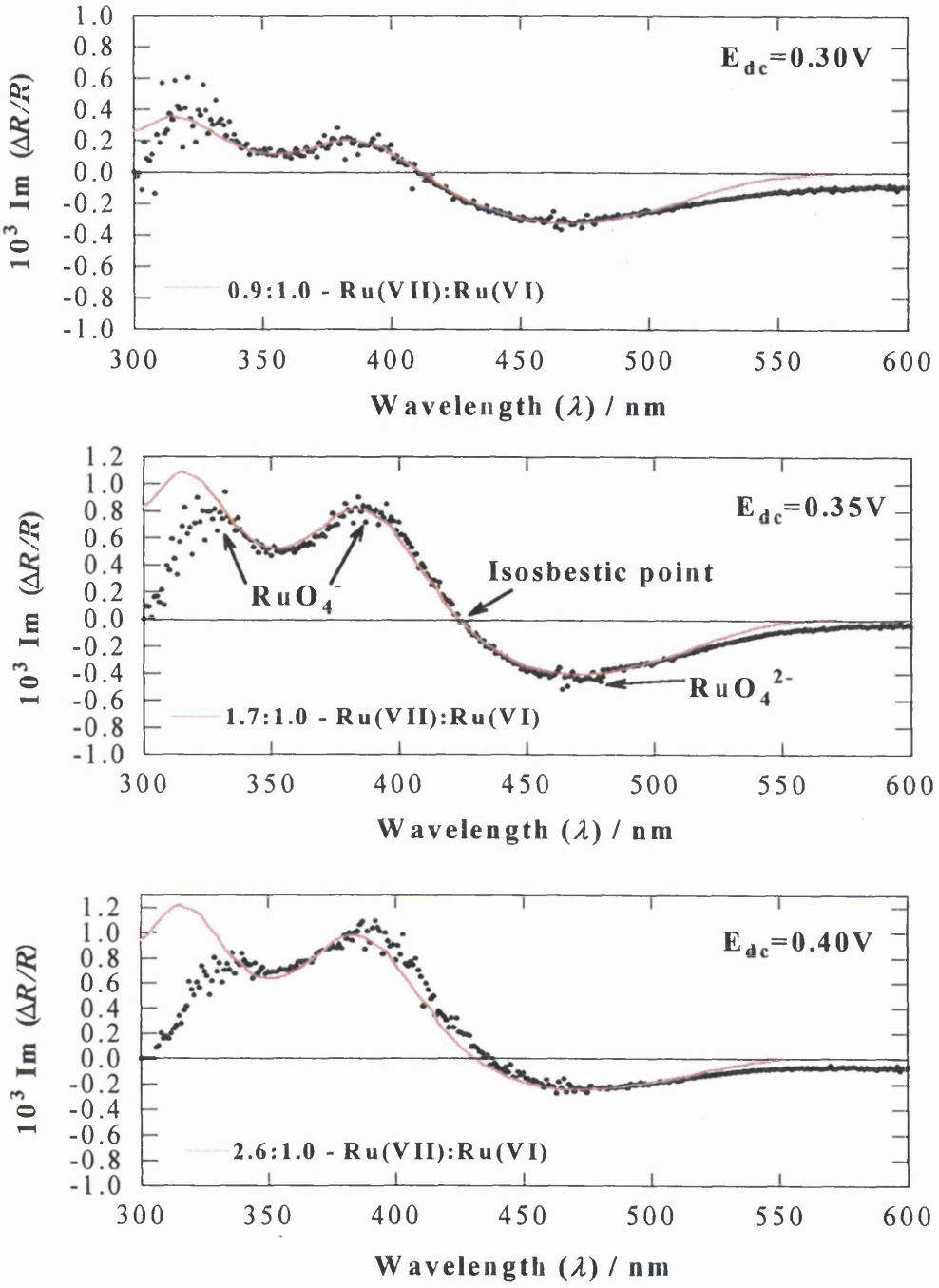

Figure 5.4 : PMR spectra recorded at potentials close to the RuO_4^- / RuO_4^{2-} equilibrium potential. Modulation frequency=9.5Hz; E_o=50mV rms; scan-rate=20nm/min. The solid lines are difference spectra calculated from the absorption spectra in **Figure 5.3** for different concentration ratios $[RuO_4^{2-}]$ / $[RuO_4^-]$.

5.2.3 PMR voltammetry

The PMR voltammetric response at fixed wavelengths was recorded as the electrode potential was scanned slowly over the entire window between hydrogen and oxygen evolution. The wavelengths were chosen to correspond to the peak maxima observed in the PMR spectra. This PMR voltammetry technique allows monitoring of the appearance (positive change in $Im(\Delta R/R)$) and disappearance (negative change in $Im(\Delta R/R)$) of a species of interest. Three wavelengths were chosen to correspond to the main peaks in the absorption spectra of RuO_4^{2-} and RuO_4^-. **Figure 5.5** presents the results. The scan at 470nm is expected to reveal the appearance and consumption of RuO_4^{2-} at potentials close to the reversible potential (0.35 V). The broad positive peak at 0.15 V indicates that RuO_4^{2-} is formed by oxidation of the RuO_2 layer on the ruthenium electrode. The negative peak at 0.35 V corresponds to the disappearance of RuO_4^{2-} as it is oxidised to RuO_4^-. The scans at 385 and 320nm are expected to pinpoint the potential region in which RuO_4^- is formed. As expected, the negative peak in the scan performed at 470nm is matched by positive peaks in the scans at 385 and 320nm. It can be seen that the intensities of the peaks observed in the potentiodynamic experiments are not identical to those seen under steady state conditions. This is attributed to the build up of corrosion species near the electrode.

The scans also show that $\Delta R/R$ peaks occur at -0.45 and 0.15V as well as in the region of the RuO_4^- / RuO_4^{2-} redox couple. According to the thermodynamic data [18], RuO_2 and higher valent ruthenium species are unstable in the region where the first peak is seen in the potentiodynamic scan. Attempts were made to record PMR spectra at -0.45 and 0.15 V in order to provide further information about the species responsible for the PMR response. Surprisingly it proved impossible to obtain spectra, since the PMR signal disappeared when the potential scan was interrupted. This interesting result

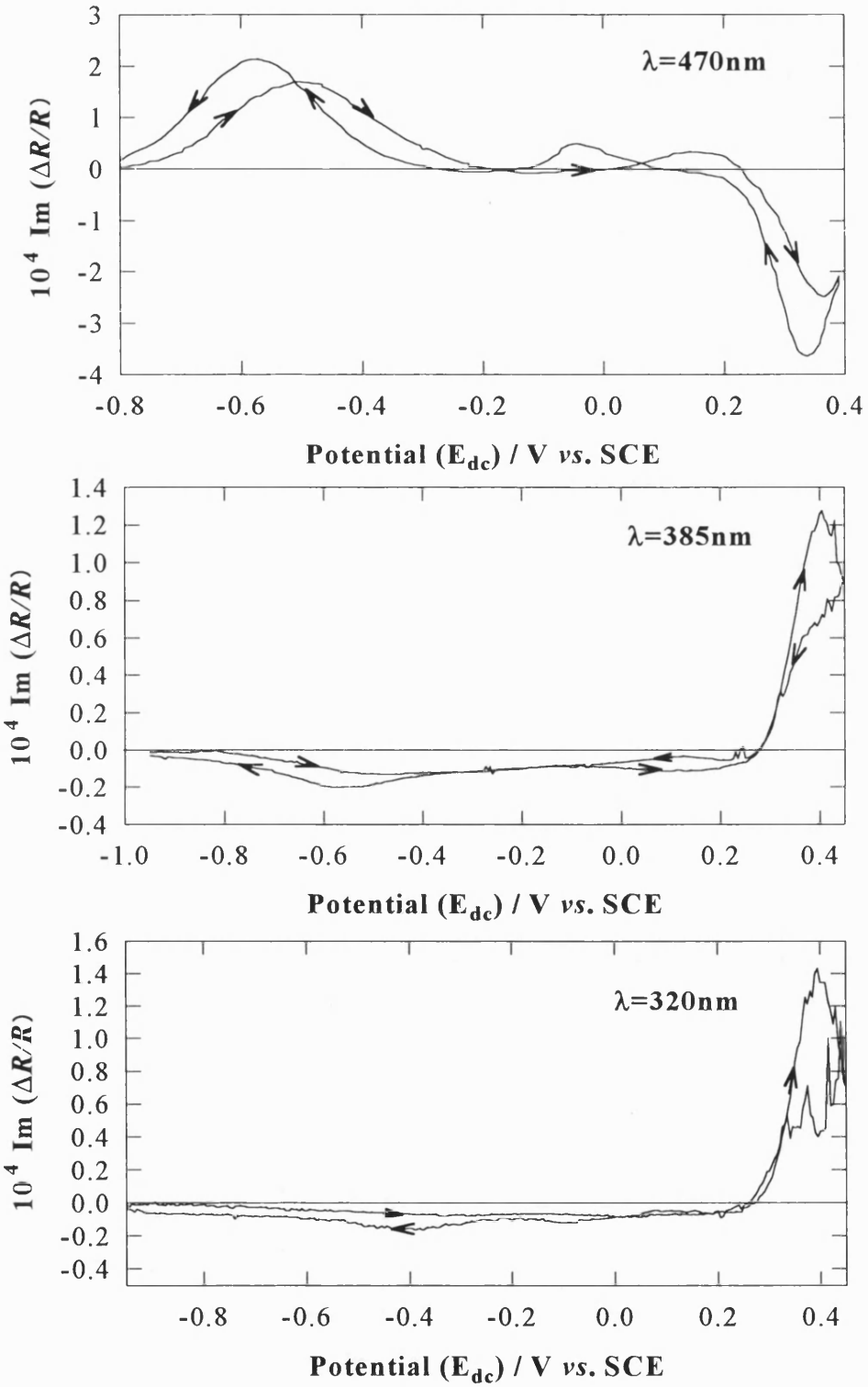

Figure 5.5 : Potentiodynamic PMR scans at 470, 385 and 320nm. Scan-rate=5mVs^{-1}.

suggests that the potentiodynamic PMR peaks at -0.45 and 0.15V are associated with irreversible surface oxidation processes such as the formation of a non-stoichiometric RuO_{2-x}.

However, the presence of a potential dependent optical response during the reverse sweep contradicts this. The optical response recorded at λ=470nm was obtained following potential cycling for ~30 minutes, due to poor signal / noise ratio during the initial potential cycle. It is therefore proposed that the PMR peaks observed at -0.45 and 0.15V are associated with a porous oxide layer (grown as a result of continuous multicycling), which exhibits electrochemical reversibility. The potential dependent optical responses recorded at λ=385 and 320nm were obtained during the first potential cycle and therefore represent the electrochemical behaviour of Ru metal.

5.2.4 Frequency response analysis

Frequency response analysis of the optical response of Ru anodes in alkali media was performed at E_{dc}=0.35V. The potential corresponds to the formal potential of the $[RuO_4^{2-}]$ / $[RuO_4^{-}]$ redox couple, which was identified by PMR spectroscopy and PMR voltammetry. Measurements were performed over the frequency range 0.1-100 Hz at a modulation amplitude of 10mV rms. Wavelength values of λ=470 and 385nm were selected to correspond to the detection of RuO_4^{2-} and RuO_4^{-} respectively. **Figure 5.6** illustrates the frequency dependent response of an Ru anode at λ=470nm.

The real and imaginary components of the optical response are opposite in sign, as predicted by the PMR theory for a diffusion-controlled process and observed for the ferro-ferricyanide model system. By convention, the formation of an optically absorbing redox species at the electrode-electrolyte interface results in a negative value for

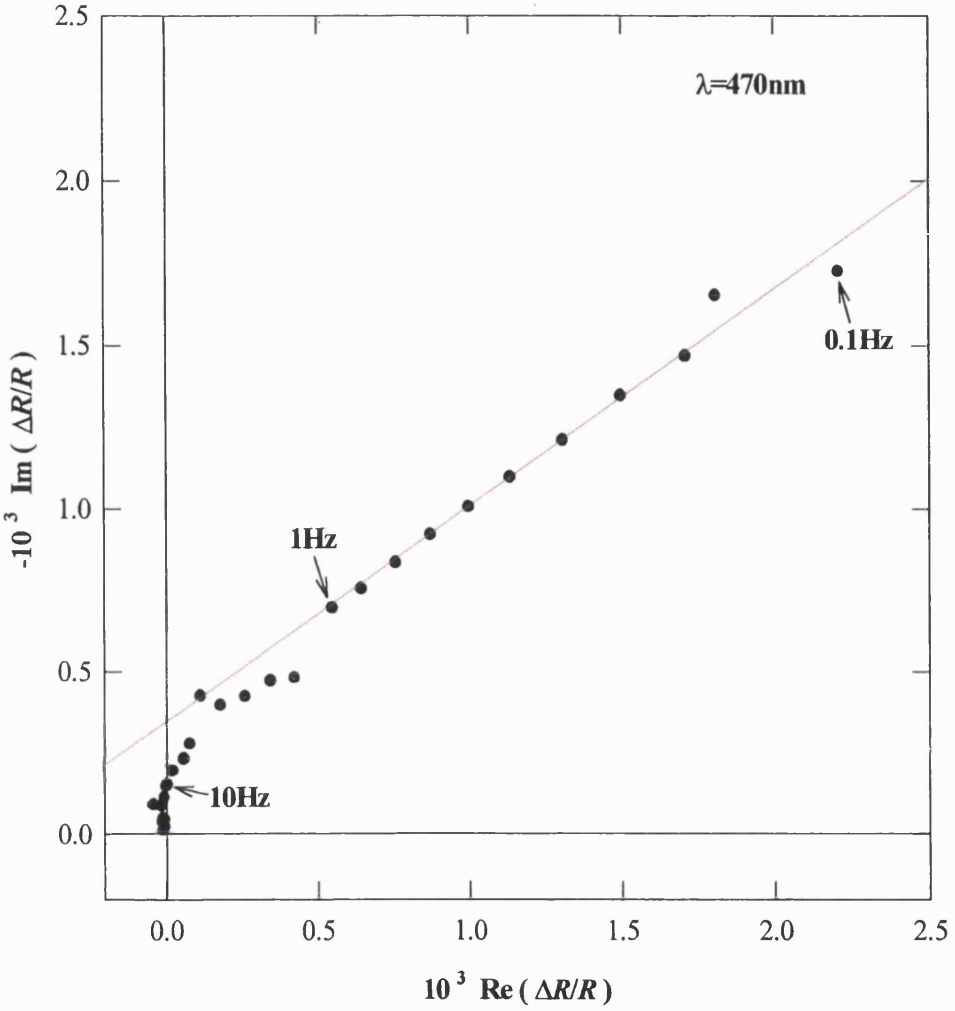

Figure 5.6 : Frequency dependent optical response of an Ru anode during O_2-evolution in alkali media : Detection of RuO_4^{2-}. E_{dc}=0.35V: E_o=10mV rms; λ=470nm $C_{[NaOH]}$=0.1M.

$Re\left(\frac{\Delta R}{R}\right)$ and a positive value for $Im\left(\frac{\Delta R}{R}\right)$ (refer to Chapter 2 for details). The signs of the frequency dependent optical response at λ=470nm are opposite to this, and therefore correspond to removal of RuO_4^{2-} at the electrode-electrolyte interface.

A linear relationship is observed between the real and imaginary components of the frequency dependent optical response in the low frequency range 0.1-1Hz. This is characteristic of a diffusion-controlled process (as observed for the frequency dependent optical response of the ferro-ferricyanide redox couple) and indicates that RuO_4^{2-} is present as a solution species. Linear regression over the same frequency range yields a straight line of slope=0.66 and intercept=$3.4x10^{-4}$. The optical response attenuates with an increase in frequency, as expected for a diffusion-controlled process, which is accompanied by bending of the optical complex plot at the high frequency limit. The observed bending is a characteristic effect of the charge transfer resistance, R_{ct} (see Section 4.4.2 for details).

Figure 5.7 illustrates the frequency dependent optical response of an Ru anode at E_{dc}=0.35V and λ=385nm. A linear relationship is again observed between the two components of the frequency dependent optical response in the low frequency range (0.1-1Hz). The signs of the two components of the optical response correspond to the formation of RuO_4^- at the electrode-electrolyte interface. Linear regression over the frequency range 0.1-1Hz yields a straight line of slope=1.58 and intercept=$3.73x10^{-3}$. The characteristic straight line optical complex plot confirms that RuO_4^- is also present as a solution species.

A simple diffusion-controlled process, such as the ferro-ferricyanide redox couple studied in Chapter 4 has a characteristic straight line optical complex plot of slope=1. Frequency response analysis of the PMR response at Ru anodes at λ=385 and 470nm

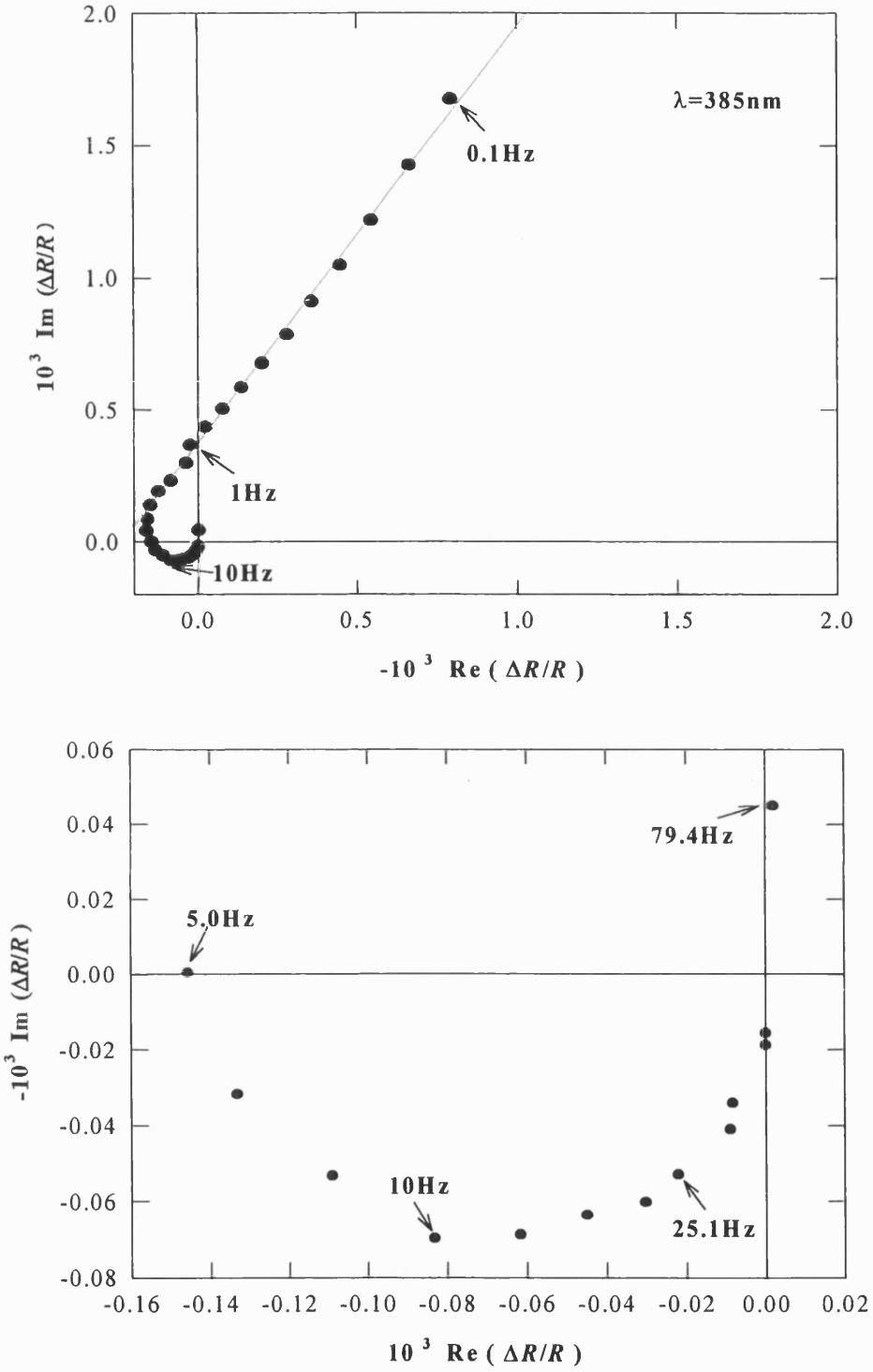

Figure 5.7 : Frequency dependent optical response of Ru anodes during O_2-evolution in alkali media : Detection of RuO_4^-. E_{dc}=0.35V; E_o=10mV rms; λ=385nm; $C_{[NaOH]}$=0.1M.

shows a deviation of the linear regression slope from unity. This suggests that the electrochemistry at the Ru anode is more complicated than the reversible redox couple $RuO_4^{2-} \rightleftharpoons RuO_4^-$.

It is proposed that instability of RuO_4^- in 0.1M NaOH (pH ~12.9) [23] results in oxidation of H_2O and liberation of O_2 to give RuO_4^{2-}. The proposed mechanism is summarised in Eq. (5.13).

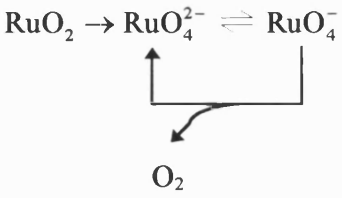

(5.13)

It should be noted that, since the reversible $RuO_4^{2-} \rightleftharpoons RuO_4^-$ redox couple is complicated by a further chemical reaction discussed above, it is not possible to extract kinetic information regarding the diffusion-controlled redox process, from the frequency dependent PMR response.

Frequency response analysis of the PMR response of Ru anodes at λ=385nm also indicates a semi-circular optical response at higher frequencies (5-100Hz), which is characteristic of a surface process. The components of the optical response are opposite in sign to the diffusion-controlled process observed in the low frequency range. The result suggests that the low frequency, diffusion controlled solution process, involving the $RuO_4^{2-} \rightleftharpoons RuO_4^-$ redox couple, is combined with a high frequency, kinetically controlled surface process. The signs of the components of the optical response correspond to a decrease in absorbance (increase in reflectance) as a result of a surface redox process. In effect, the frequency dependent optical response at λ=385nm is simply a combination of a low frequency diffusion-controlled process with a higher

frequency surface redox process. This results in a region between 1-10Hz where the real and imaginary components of the optical response have the same sign, which explains the unexpected sign change observed during PMR spectroscopy measurements (see section 5.2.2 for details)

It is proposed that the detected surface process is due to a possible change in stoichiometry of RuO_{2-x} to $RuO_{2-x+\delta x}$. This is supported by the work of Rishpon and Gottesfeld who have reported on the change in stoichiometry of anodically grown Ru oxide films using ellipsometry and *ac* impedance measurements [24]. They describe the change in stoichiometry in terms of a "double ejection" process involving the ejection of electrons and protons as illustrated in Eq. (5.14).

$$RuO_x \text{-}nH_2O + ye^- + yH^+ \rightleftharpoons RuO_{x-y}(OH)_y \text{-}H_2O \qquad (5.14)$$

The authors report an increase in reflectance of an Ru oxide film with a corresponding increase in potential over the region between H_2 and O_2-evolution.

The identification of a surface redox process by frequency response analysis, also leads us to suggest that the discrepancy observed between the experimental PMR spectra and the difference absorption spectra in the UV region (300-330nm) (see **Figure 5.4**) is attributed to the formation of non-stoichiometric RuO_{2-x+dx}.

5.3 Electrochemical and Spectroscopic studies of Ru anodes in acid media

Electrochemical and spectroscopic studies of an Ru anodes in acid media (0.1M H_2SO_4) are presented. The discussion is limited to cyclic voltammetry and PMR spectroscopy.

5.3.1 Cyclic voltammetry

Figure 5.8 illustrates a typical cyclic voltammogram obtained for Ru in 0.1M H_2SO_4 at a scan-rate of $13mVs^{-1}$. The shape of the voltammogram is similar to the one shown in **Figure 5.1** for alkali media and, as expected, the peaks are shifted to more positive potentials by the change in pH. However, observation of the Pourbaix diagram (**Figure 5.2**) and available thermodynamic data [18] indicate that RuO_4^{2-} and RuO_4^{-} are not expected to be stable in acid solution. Instead, RuO_4 is expected to be the only stable product of the oxidation of RuO_2.

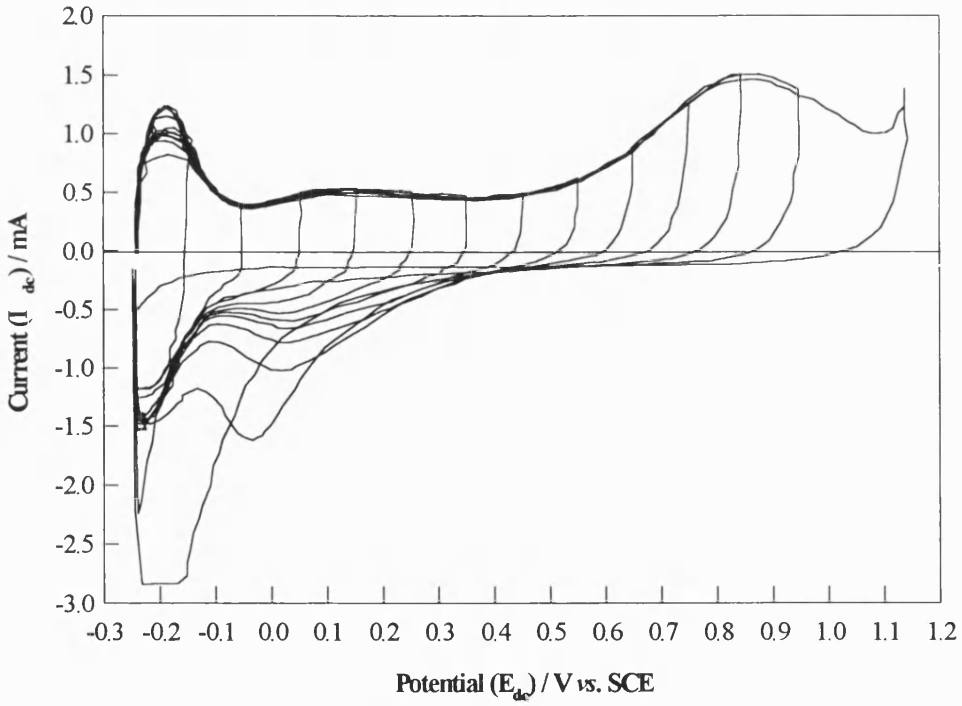

Figure 5.8 : A typical cyclic voltammogram of an Ru anode in acid media. $C_{[H_2SO_4]} = 0.1M$; scan-rate=$13mVs^{-1}$.

5.3.2 PMR Spectroscopy

No stationary state PMR response was obtained at potentials more negative than 1.1 V *vs.* SCE. The PMR spectrum measured at 1.15 V at the onset of O_2-evolution is illustrated in **Figure 5.9**. The spectrum is monopolar and exhibits well defined peaks at 320nm and 385nm. As the figure illustrates, the experimental PMR data fit well to the absorption spectrum of RuO_4 [19]. It is concluded that RuO_4 is the only detectable product in the potential region. This result supports a previous study by Bewick *et al.* who identified RuO_4 in acid media by *In-situ* IR spectroscopy (SNIRTIRS) [25].

5.4 Discussion and Conclusions

Potential modulated reflectance spectroscopy (PMRS) has been used to study the anodic oxidation of ruthenium. Although the cyclic voltammograms of ruthenium in alkali media are broad and relatively featureless, PMRS allows identification of soluble RuO_4^{2-} [Ru(VI)] and RuO_4^- [Ru(VII)] species formed at the onset of oxygen evolution. The PMR spectra exhibit an isosbestic point that is attributed to the $RuO_4^{2-} \rightleftharpoons RuO_4^-$ redox couple. The peaks in the PMR spectra correlate well with reported λ_{max} values of RuO_4^{2-} at 470nm and RuO_4^- at 385nm and 315nm. The PMR spectra can be fitted to a difference spectrum calculated from the absorption spectra of the two species. PMR studies of ruthenium dissolution in acid solutions indicate that RuO_4 is the only identifiable corrosion product formed in the oxygen evolution region in this case.

Frequency response analysis has shown that the diffusion-controlled response, which corresponds to the formation of RuO_4^-, is complicated by a surface redox process. The high frequency optical response is attributed to a change in the non-stoichiometry of a surface oxide e.g. $RuO_{2-x} \rightleftharpoons RuO_{2-x+\delta x}$. Use of a flow-cell design [26] will enable

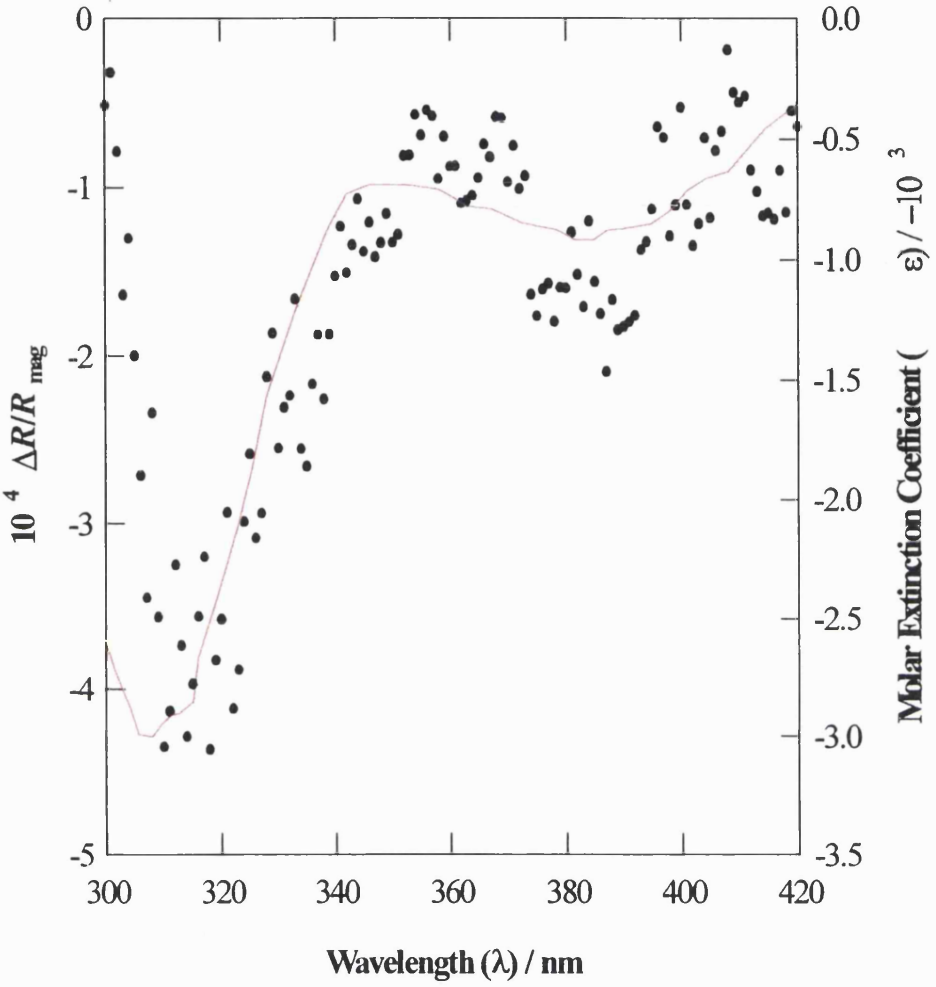

Figure 5.9 : PMR spectrum of an Ru anode during O_2-evolution in acid media. $C_{[H_2SO_4]} = 0.1$M; scan-rate=5mVs^{-1}.

deconvolution of the solution and surface processes by detection of the $RuO_4^{2-} \rightleftharpoons RuO_4^-$ redox couple down-stream of the Ru anode surface.

The results show that PMR spectroscopy is a powerful *in-situ* technique for the identification of corrosion products formed at the ruthenium / electrolyte interface. The use of frequency dependent PMR has shown that it is possible to distinguish between a surface and solution redox process that occur concurrently at the electrode-electrolyte interface, by selecting an appropriate frequency value. It follows that the interpretation of PMR spectra cannot be fully achieved without the support of frequency response analysis.

References

1. M.L.B. Rao, A. Damjanovic and J.O'M. Bockris, *J. Phys. Chem.*, **67**, 2508 (1963)
2. S. Trasatti and G. Buzzanca, *J. Electroanal. Interfacial Electrochem.*, **29**, App. 1 (1971)
3. J. Llopis and M. Vazques, *Electrochimica Acta.*, **11**, 633 (1966)
4. D. Galizzioli, F. Tantardini and S. Trasatti, *J. Appl. Electrochem.*, **4**, 57 (1974)
5. C. Iwakura, K. Kirao and H. Tamura, *Electrochimica Acta*, **22**, 329 (1977)
6. L.D. Burke and T.O. O'Meara, *J. Chem. Soc., F. T. 1*, **68**, 839 (1972)
7. S. Hädzi-Jordanov, H. Angerstein-Kozlowska and B.E. Conway, *J. Electroanal. & Interfacial Electrochem.*, **60**, 359 (1975)
8. L.D. Burke and J.K. Mulcahy, *J. Electroanal. & Interfacial Electrochem.*, **73**, 207 (1976)
9. K. Kinoshita and P.N. Ross, *J. Electroanal & Interfacial Electrochem.*, **78**, 313 (1976)
10. S. Hädzi-Jordanov, H. Angerstein-Kozlowska, M. Vukovic and B.E. Conway, *J. Electrochem. Soc.*, **125**(9), 1471 (1978)
11. S. Hädzi-Jordanov, H. Angerstein-Kozlowska, M. Vukovic and B.E. Conway, *J. Phys. Chem.*, **81**(24), 2271 (1977)
12. K.W. Lam, K.E. Johnson and D.G. Lee, *J. Electrochem. Soc.*, **76**, 1069 (1978)
13. L.D. Burke, O.J. Murphy, J.F. O'Neill and S. Venkatesan, *J. Chem. Soc., F.T. 1*, **73**, 1659 (1977)
14. L.D. Burke and D.P. Whelan, *J. Electroanal. Chem.*, **103**, 179 (1979)
15. M.E.G. Lyons and L.D. Burke, *J. Chem. Soc., F.T. 1*, **83**, 299 (1987)
16. M. Vukovic, H. Angerstein-Kozlowska, M. Vukovic and B.E. Conway, *J. Appl. Electrochem.*, **12**, 193 (1982)

17. V. Birss, R. Meyers, H. Angerstein-Kozlowska and B.E. Conway, *J. Electrochem. Soc.*, **131**, 1502 (1984)

18. M.Pourbaix, "*Atlas of Electrochemical Equilibria in Aqueous Solutions*", Pergamon, London (1966). p.343

19. R.E. Connick and C.R. Hurley, *J. Am. Chem. Soc.*, **74**, 5012 (1952)

20. G.A. Stoner, *Anal. Chem.*, **27**, 1186 (1955)

21. R.P. Larsen and L.E. Ross, *Anal. Chem.*, **41**, 176 (1959)

22. G.B. Barton, *Spectrochimica Acta*, **19**, 1619 (1963)

23. J.F. Llopis and I.M. Tordesillas, "*Encyclopedia of Electrochemistry of the Elements*" Ch.8

24. J. Rishpon and S. Gottesfeld, *J. Electrochem. Soc.*, **131**(8), 1960 (1984)

25. A. Bewick, C. Gutiérrez and G. Larramona, *J. Electroanal. Chem.*, **332**, 155 (1992)

26. see e.g. J. O'M. Bockris and B. Yang, *J. Electroanal. Chem.*, **252**, 209 (1988)

Chapter 6

Chapter 6

Electrochemical and Spectroscopic Studies of the Anodic Behaviour of Ruthenium-Iridium Alloys

6.1 An Introduction to Ru-Ir mixed oxide anodes

The electrochemistry and electrocatalytic performance of Ru / RuO_2 anodes during O_2 evolution has been studied extensively [1]. However, the corrosion of Ru / RuO_2 anodes during O_2 evolution in both acid and alkali media [2-4] has led to the development of mixed anode systems which improve stability whilst maintaining electrocatalytic performance (see Section 1.2.2 and references therein). A ruthenium-iridium mixed oxide is one such anode that has been studied as an electrocatalyst for O_2 and Cl_2 evolution [5-11].

6.1.1 A review of iridium electrochemistry

The electrochemistry of iridium oxide anodes has been widely studied due to their high stability and electrocatalytic activity towards O_2 and Cl_2 evolution [12-16]. The accompanying electrochromic effect at iridium oxide films has also attracted interest [14,17-21].

The anodic behaviour of iridium has been mainly studied by cyclic voltammetry. These studies have established a distinction between monolayer formation and growth of a multilayer oxide [16,22,23]. The formation and reduction of a monolayer of oxide during potential cycling has been reported to exhibit hysteresis [22] and this behaviour is therefore comparable to Ru anodes [24]. In contrast, electrochemical cycling of iridium

films results in the growth of an oxide film which is not reduced during cathodic reduction. The oxide film demonstrates reversible behaviour [16,24]. It is proposed that oxide growth occurs as a result of continual monolayer oxide formation at the metal / oxide interface beneath the oxide film [22]. The reversible electrochemistry observed at Ir anodes, following electrochemical cycling, is attributed to redox processes within the oxide film. An example of a cyclic voltammogram of an Ir anode is given in **Figure 6.1**.

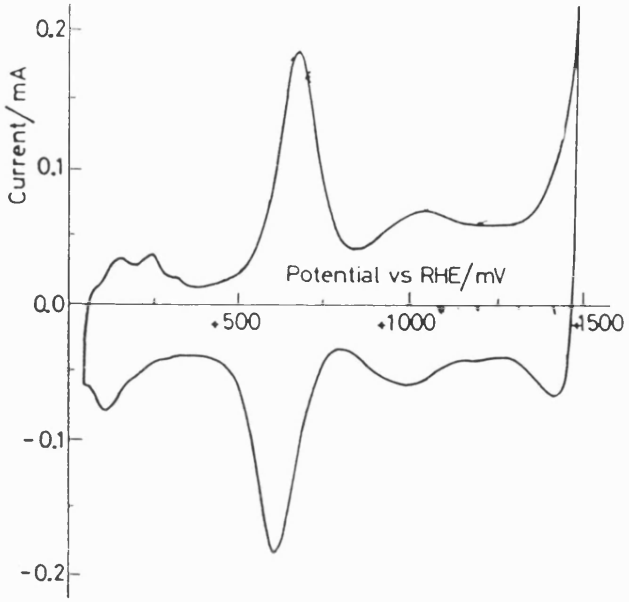

Figure 6.1 : A typical cyclic voltammogram of an anodic Ir oxide film (AIROF) grown electrochemically on Ir in alkali media. $C_{[NaOH]}$=0.1M; v=20mVs^{-1} [25].

The main reversible peak observed during potential cycling at 0.7V *vs.* RHE has been attributed to the Ir(III) $\rightleftharpoons$ Ir(IV) redox couple. The redox process is also accompanied by a change in colour of the oxide film from transparent to blue-black. The term, an electrochromic effect, is used to describe the change in colouration of an electrode surface as a result of a change in potential. The electrochromic effect observed for iridium oxide films has been attributed to proton and electron transfer across the

metal-electrolyte interface [14,17-21]. Gottesfeld *et al.* have proposed the following mechanism for the reversible redox process [17].

$$\underset{\text{(transparent)}}{\mathrm{Ir(OH)_n}} \rightleftharpoons \underset{\text{(coloured)}}{\mathrm{IrO_x(OH)_{n-x}}} + x\mathrm{H^+} + xe^- \qquad (6.1)$$

The electrochromic effect can be understood more clearly if we consider the band structure of IrO_2. **Figure 6.2** illustrates a simplified band structure of IrO_2 [26].

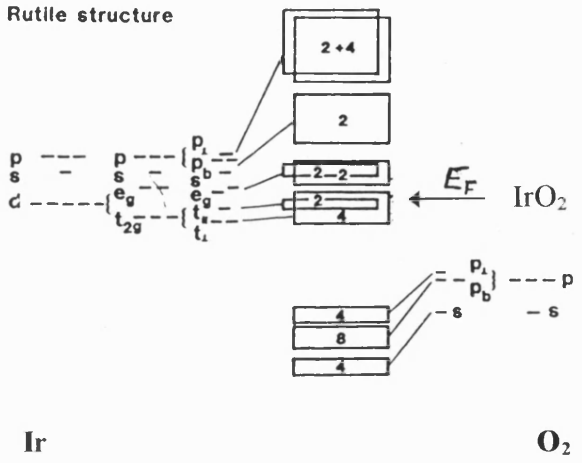

Figure 6.2 : Schematic band structure of the rutile form of IrO_2. The numbers in the bands denote maximum electron occupancy [26].

IrO_2 has the rutile structure. In this structure, each metal atom is surrounded by six oxygen atoms in an octahedral array. This results in crystal field splitting of the d-band into two components, e_g (doubly degenerate) and t_{2g} (triply degenerate) as illustrated in **Figure 6.2**. It follows that the 5 d electrons of IrO_2 will exist in the Ir t_{2g} band. Since the position of the Fermi level E_F is determined by the occupancy of the d-electrons in the bands [27], it follows that E_F will exist within the Ir t_{2g} band. IrO_2 should therefore possess metallic conductivity, where Ir t_{2g} and O 2p constitute the conduction and

valence bands respectively. Band gap energy values within the range 3.2-3.5eV have been reported [28-29].

Glarum and Marshall [30] report an increase in conductivity of the oxide film on iridium from $<10^{-2}\Omega^{-1}$ cm^{-2} to $>10^{2}\Omega^{-1}$ cm^{-2} as the potential is scanned to switch the film between the transparent and coloured forms. These observations suggest that the conductivity is a function of the oxidation state of the oxide film. The change in conductivity of the oxide film from an insulating state, Ir(III) to a conducting state, Ir(IV) can be explained by the band structure proposed for noble metal oxides [26]. **Figure 6.3** illustrates the change in band structure, and hence conductivity, as a function of oxidation state of the Ir oxide film and is based on the model reported in **Figure 6.2**.

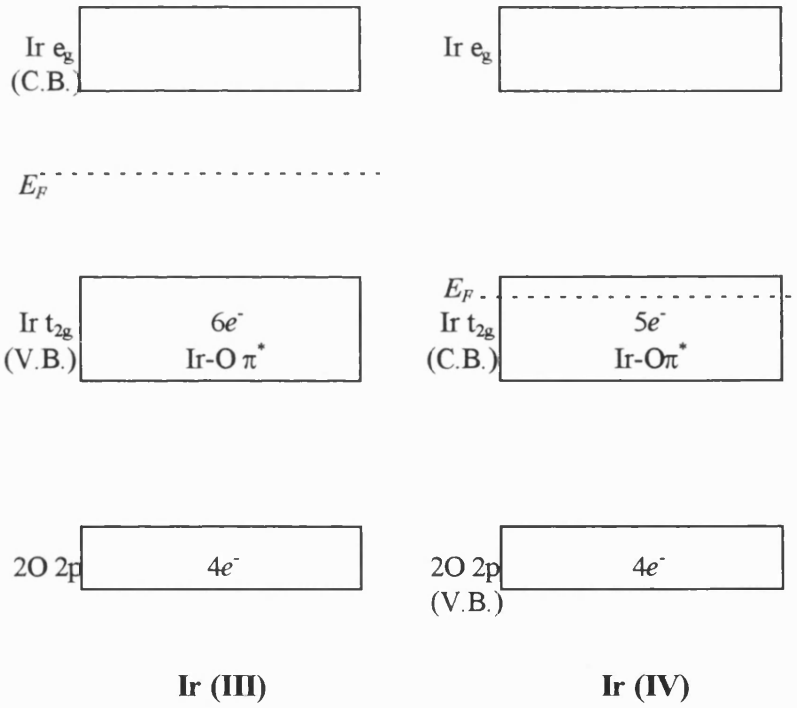

Figure 6.3 : Change in band structure as a function of oxidation of Ir oxide films. The model is based on the band structure reported in Ref. [26].

In the case of Ir(III), the Fermi level exists in the gap between the t_{2g} and e_g bands, which is characteristic of a semi-conductor. The t_{2g} and e_g bands correspond to the valence and conduction band respectively. Following oxidation of the iridium film to Ir(IV), the Fermi level is lowered into the t_{2g} band which now exists as the conduction band. The presence of the Fermi level in the middle of a conduction band induces metallic conductivity in the film as reported by Glarum and Marshall [30].

XPS studies have also provided an insight into the anodic behaviour of iridium oxide films [31]. Kötz *et al.* have reported a constant Ir : O ratio over the potential range 0.0V - 1.25V vs. SCE for iridium oxide films formed by the electrochemical cycling in acid media of sputtered Ir anodes. Deconvoluted O 1s levels have been identified which indicate the presence of a surface Ir-oxyhydroxide, the structure of which is dependent on potential. The spectra indicate that an increase in potential results in a reduction of hydroxide species, which is accompanied by an increase in oxide species at the iridium oxide surface. Based on these findings, the authors proposed the following mechanism for O_2-evolution. The preceding electrochromic process is also shown in **Figure 6.4**.

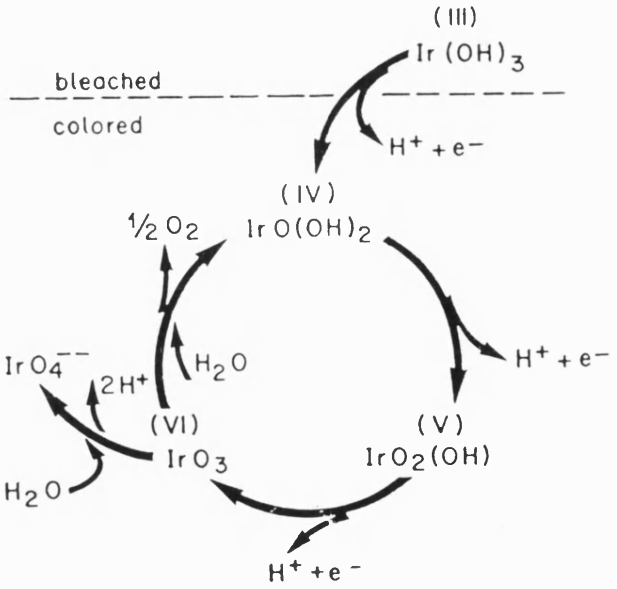

Figure 6.4 : Model for charge storage and O_2-evolution at iridium anodes [31].

6.1.2 Electrochemistry of Ru-Ir mixed oxides

The use of iridium as a stabilizer in Ru-Ir anodes has proved highly effective. Several authors have reported an increase in stability during O_2-evolution in acid media [5-7,9,32]. However, the disadvantage of this mixed oxide system has been the reported decrease in electrocatalytic performance. This has been identified by an increase in Tafel slope and overpotential for O_2-evolution [6,7]. A linear correlation between the O_2-evolution overpotential and the composition of $Ru_xIr_{1-x}O_2$ has been observed [6].

XPS has been used to characterise the surface of Ru-Ir alloys and Ru-Ir mixed oxides during O_2-evolution [6,7]. The Ru 3d XPS spectrum indicates that oxidation of Ru metal at the surface of Ru-Ir alloys is inhibited by the presence of iridium [6]. In contrast, the oxidation of iridium is enhanced. XPS-valence spectra of Ru-Ir mixed oxide anodes prepared by reactive sputtering indicated the presence of a common electronic *d*-band between Ru and Ir, where the electrons on IrO_2 sites are shared with RuO_2 sites [7]. It is proposed that the common band prevents oxidation of the RuO_2 sites to oxidation state VIII, which is the case for Ru / RuO_2 anodes. This would then limit the formation of RuO_4 and therefore reduce corrosion.

No *in-situ* spectroscopic studies have been reported on the anodic behaviour of Ru-Ir mixed alloy or mixed oxide systems. It is clear that there is still a lack of understand regarding the stabilising effect of iridium in the mixed oxide. This study of an Ru-Ir mixed alloy by PMRS therefore provides the first *in-situ* evidence of the oxidation state of the anode surface during potential cycling and under conditions of O_2 evolution. This chapter presents PMRS results for the anodic behaviour of an electrodeposited Ru-Ir alloy [32] in alkali media.

6.2 Electrochemical and spectroscopic studies of an Ru-Ir alloy

6.2.1 Cyclic voltammetry

Cyclic voltammetry was performed using an electrodeposited Ru-Ir alloy of stoichiometry $Ru_{0.4}Ir_{0.6}$, in 0.1M NaOH [32] (refer to section 3.3.2 for details). A typical cyclic voltammogram is illustrated in **Figure 6.5**. During the first cycle, a hydrogen adsorption/desorption region is observed between -0.95 and -0.8V. A small reversible peak is seen at E=-0.36V. A very broad surface oxidation peak is also observed over the potential range -0.1 - 0.40V. Electrochemical cycling results in the growth of the reversible peak. This is accompanied by broadening of the broad surface oxidation peak.

The reversible peak observed at E=-0.36V is characteristic of the electrochemistry of Ir [22-24]. In fact, the position of the reversible peak is in good agreement with the reversible peak observed by Gutiérrez *et al.* [25] at 0.34V *vs.* SCE for an anodic iridium oxide film (AIROF) at pH 13. The pseudocapacitance of the reversible peak was evaluated as C_F=47.3mF cm^{-2}.

The broad surface charge region shows partial irreversibility, which is indicative of incomplete reduction of the surface oxide during the cathodic sweep. This indicates an increase in the charge storage capacity of the oxide film, which is related to the growth of the oxide film.

6.2.2 PMR spectroscopy

The anodic behaviour of Ru-Ir alloys was studied by PMR spectroscopy over the potential range -0.80 - 0.40V. All spectra were recorded at a modulation amplitude=10mV rms and frequency=1Hz. **Figure 6.6** illustrates the spectrum recorded at E_{dc}=-0.40V. This corresponds to the region where the reversible redox peak was observed during cyclic voltammetry. The spectrum has a peak maximum at λ=330nm

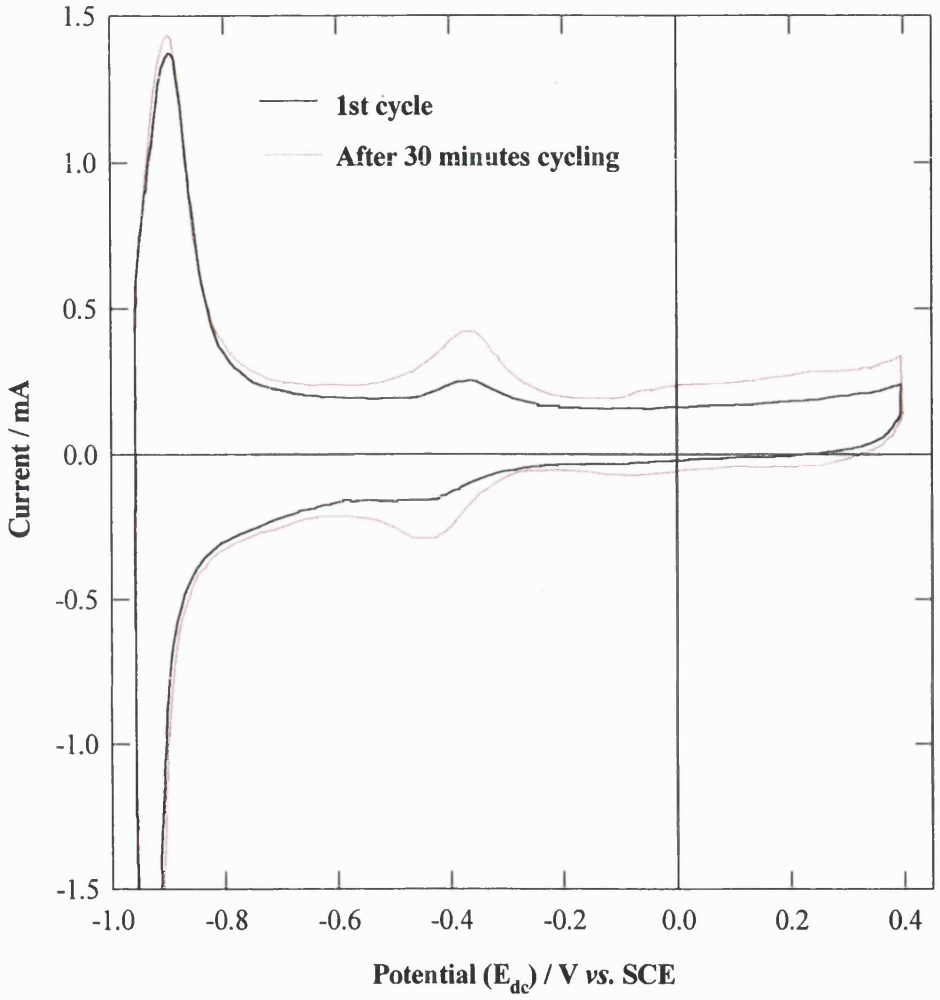

Figure 6.5 : Cyclic voltammogram of Ru-Ir alloy in 0.1M NaOH. Sweep-rate=13mVs^{-1}

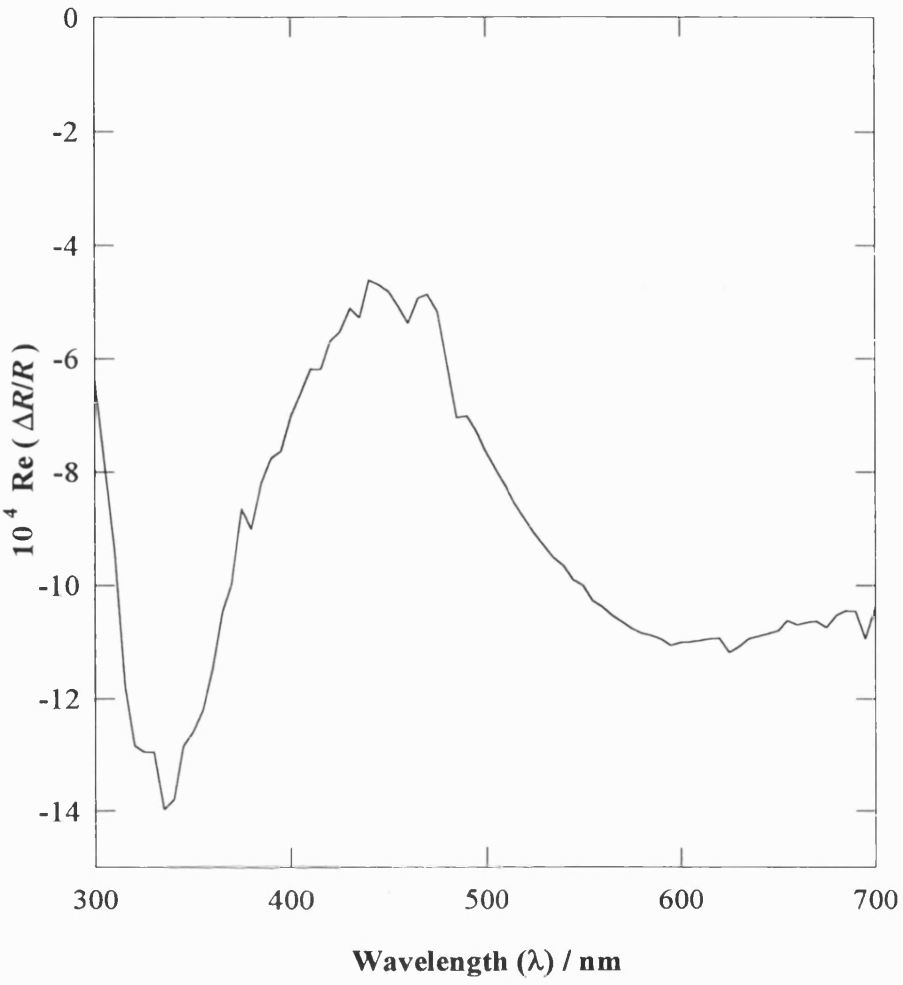

Figure 6.6 : PMR spectrum of an Ru-Ir alloy in 0.1M NaOH. E_{dc}=-0.40V; E_o=10mV rms; modulation frequency=1Hz.

and a broad peak at λ=600nm. A minimum occurs at λ=445nm.

The electrochemistry of a Ru-Ir appears to be dominated by Ir. In order to interpret the spectra correctly, it is therefore necessary to review the optical data available for possible Ir-oxy species formed during potential cycling. Several optical studies have been carried out at IrO_2 [17,25,28,33]. Reflectivity studies single crystal

IrO_2 have been carried out by Goel *et al.* [28] over the wavelength range 130-1200m. The authors derived the real and imaginary components of the complex optical dielectric constant, ε' and ε'' from the experimental reflectivity data. The resultant spectra have several features that are of interest. A peak maximum was observed at 309nm together with a shoulder peak at 610nm. A minimum in the spectrum was present at 459nm. These features are consistent with the PMR spectrum recorded at E_{dc}=-0.40V. A PMRS study of AIROFs by Gutiérrez *et al.*, [25] showed similar features which are consistent with those reported here for a Ru-Ir alloy. Their PMR spectrum recorded at E_{dc}=-0.34V, which corresponds to the reversible peak, had peak maxima at 260-300nm and 580-610nm. A peak minimum was also observed at ~460nm.

The absorption spectrum of IrO_2 films formed by reactive sputtering (SIROFs) is reported to have a maximum at 610nm [33]. A minimum in the spectrum at 465nm is also observed. Similar features have been observed for an anodically grown iridium oxide film by the same author. Gottesfeld *et al.* [17] have obtained differential spectra for an iridium oxide film following conversion from a transparent to coloured state. The authors reported peak maxima at 280nm and 610nm which they attributed to O(2p) $\rightarrow$ Ir 5d(e_g) interband charge transfer and Ir 5d(e_g)$\rightarrow$ Ir 5d(e_g) intraband transitions within the t_{2g} band, respectively (see **Figure 6.3** for details).

It is concluded that the PMR spectrum at -0.40V corresponds to the formation of Ir (IV), probably in the form of an oxyhydroxide. It follows that the reversible redox peak produced at E=0.36V during cyclic voltammetry corresponds to the Ir(III) $\rightleftharpoons$ Ir(IV) redox couple. This redox process is accompanied by an electrochromic effect. The minimum in the PMR spectrum at 450nm corresponds to the blue wavelength region, which supports the change in colouration from transparent to blue during the redox process.

Figure 6.7 illustrates the PMR spectra obtained for a Ru-Ir alloy at the more anodic potentials of 0.00V, 0.20V and 0.40V. A peak maximum is observed at λ=400nm for E_{dc}=0.00V. An increase in potential to E_{dc}=0.20V is also accompanied by a shift in the peak maximum to λ=450nm. A change in sign of the optical response

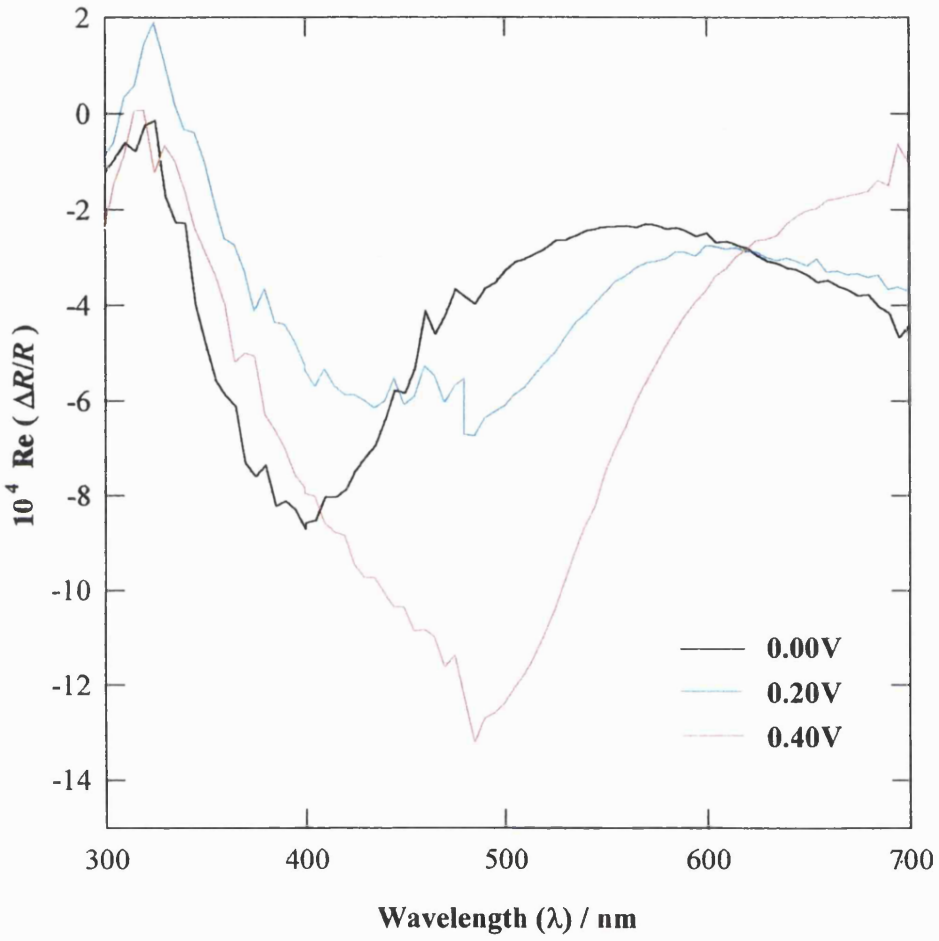

Figure 6.7 : PMR spectra of a Ru-Ir alloy in alkali media. E_{dc}=0.00, 0.20 & 0.40V; E_o=10mV rms; modulation frequency=1Hz; $C_{[NaOH]}$=0.1M.

between 310 and 335nm is also observed at E_{dc}=0.20V. At E_{dc}=0.40V, a further shift in peak maximum to λ=485nm is observed. Direct interpretation of these peaks has not

been possible due to a lack of optical data for Ir-oxy species in this potential region. However, it should be noted that all the features observed are similar to those reported by Gutiérrez *et al.*, who carried out a PMR study of AIROFs. This therefore supports the view that the surface electrochemistry of Ru-Ir alloys is dominated by Ir. It is also important to note that the PMR features observed for Ru anodes at E_{dc}=0.40V, corresponding to the corrosion products RuO_4^{2-} and RuO_4^-, are not observed for the Ru-Ir alloy.

6.2.3 PMR voltammetry

PMR voltammograms were recorded over the potential range -0.95 - 0.40V. Wavelength values were selected to correspond to the peak maxima observed in the PMR spectra. **Figure 6.8** and **Figure 6.9** illustrates the PMR voltammograms obtained at λ=320nm and 600nm, which correspond to Ir(IV). The real and imaginary components of the optical voltammetric response are shown for comparison. At λ=320nm, a peak maximum is observed for the forward scan at -0.300 ± 0.005V, together with a peak maximum at 0.370 ± 0.005V for the reverse scan. The PMR voltammograms recorded at λ=600nm have peak maxima at 0.300V ± 0.005V and 0.370V ± 0.005V for the forward and reverse scans respectively. The real and imaginary components are opposite in sign, as predicted by the theory for a surface film process and of the correct sign to support the formation of Ir(IV) at the reversible peak at E_{dc}=-0.36V. It is interesting to note that a real optical response is detected under potentiodynamic conditions over the potential range 0.00 - 0.40V that is not observed in the imaginary optical response.

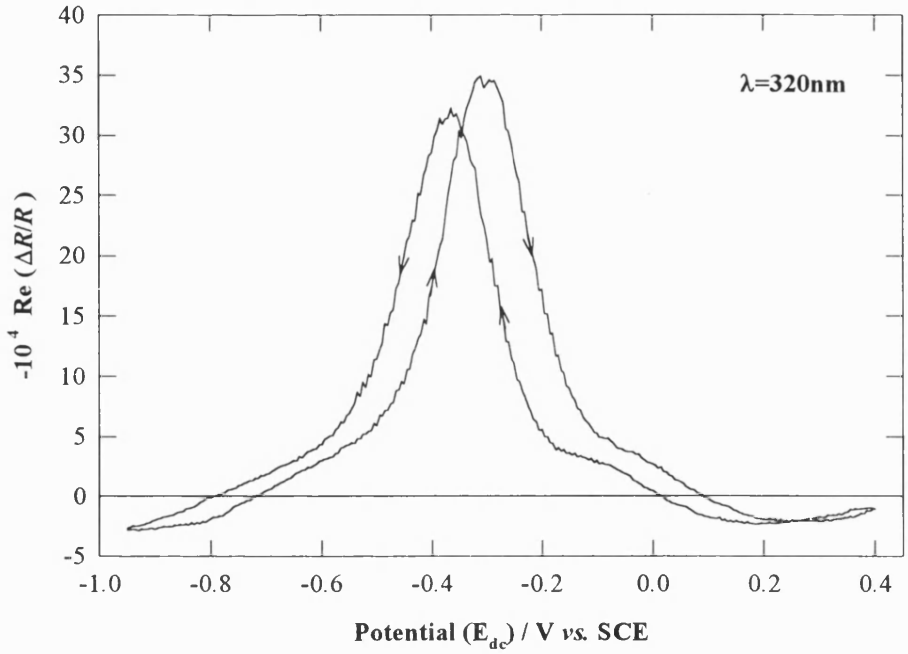

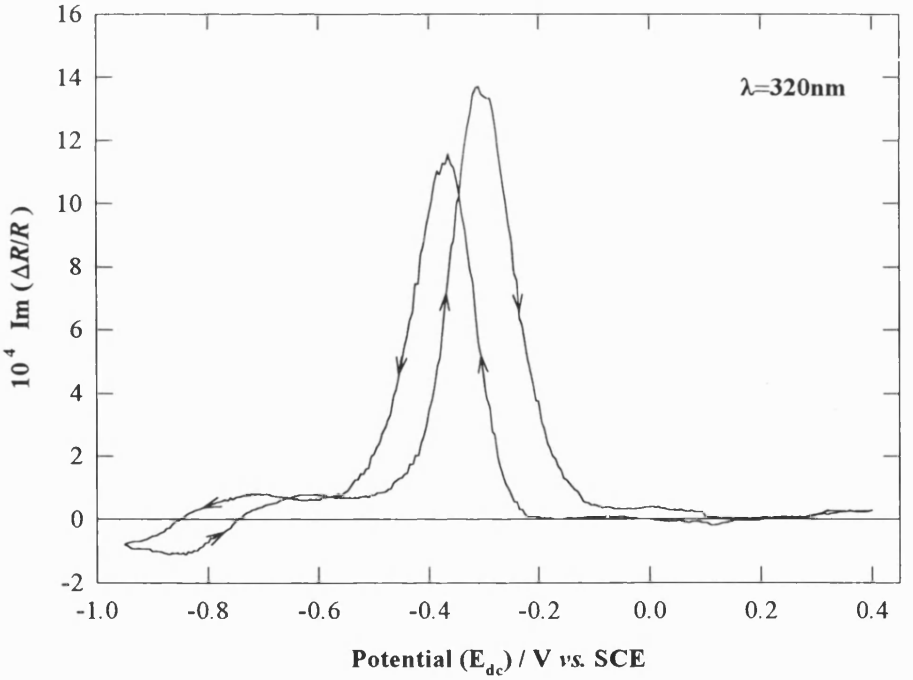

Figure 6.8 : PMR voltammogram of an Ru-Ir alloy in alkali media. λ=320nm; E_o=10mV rms, modulation frequency=1Hz; $C_{[NaOH]}$=0.1M.

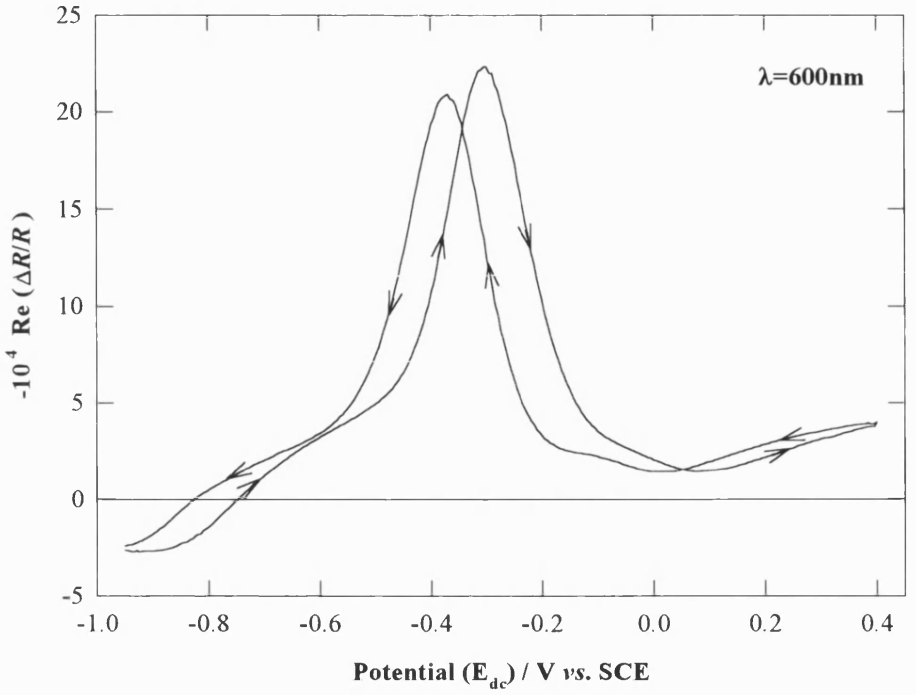

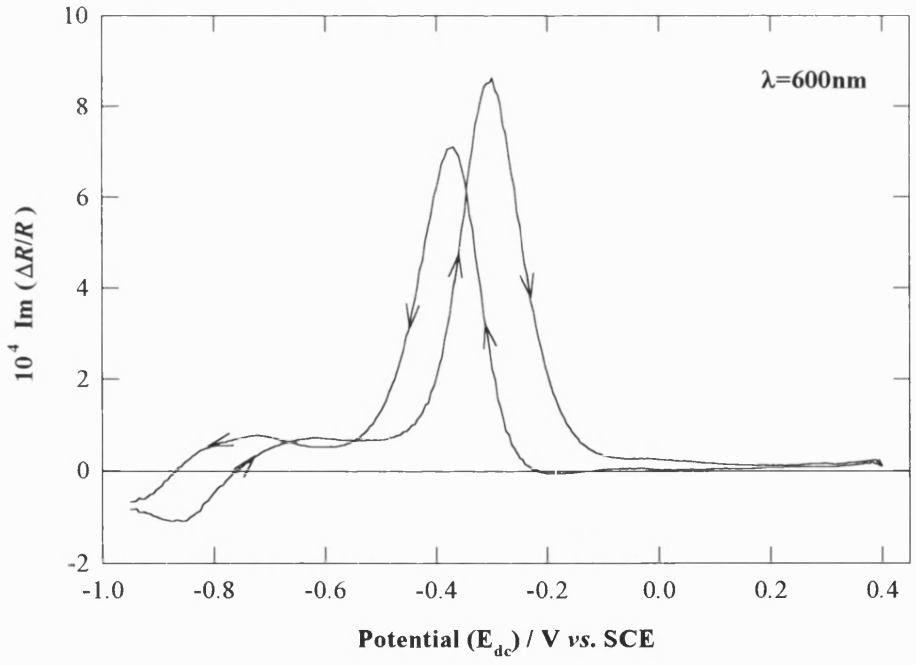

Figure 6.9 : : PMR voltammogram of an Ru-Ir alloy in alkali media. λ=600nm; E_o=10mV rms, modulation frequency=1Hz; $C_{[NaOH]}$=0.1M.

PMR voltammograms were also recorded at λ=400nm and 500nm. These values correspond to the iridium oxide films formed in the broad potential range -0.10 - 0.40V. **Figure 6.10** illustrates the PMR voltammogram obtained at λ=400nm. The real and imaginary components of the potential dependent optical response are again shown for comparison.

Some interesting features observed at this wavelength were not obtained at λ=320 / 600nm. The PMR voltammogram at λ=400nm shows a second PMR peak at E_{dc}=0.030 ± 0.005V together with the previously discussed electrochromic peak at E_{dc}=0.300 ± 0.005V. This suggests that a further Faradaic process occurs following the electrochromic process which coincides with the charge storage region observed in cyclic voltammetry. A background optical response is also observed over the potential range -0.2 - 0.40V for the real component which is not observed for the imaginary component. This observation suggests that at a modulation frequency=1Hz, the capacitance of the surface film C_a associated with the charge storage process dominates the optical response.

Figure 6.11 illustrates the potential dependent optical response recorded at λ=500nm. The electrochromic process is again clearly defined at E_{dc}=-0.310 ± 0.005V. The real component of the potential dependent optical response also exhibits a broader peak at E_{dc}=0.400 ± 0.005V, together with a shoulder at ~ 0.10V. The broad peak is in excellent agreement with the PMR spectrum recorded at 0.40V (see **Figure 6.7**), which has a peak maximum at λ=485nm. The shoulder can be attributed to the potential dependent optical response observed in the same potential region at λ=400nm (see **Figure 6.10**). The difference in response of the real and imaginary optical responses over the potential range -0.2 - 0.40V can again be attributed to dominance of the real optical response by the capacitance of the oxide film C_a.

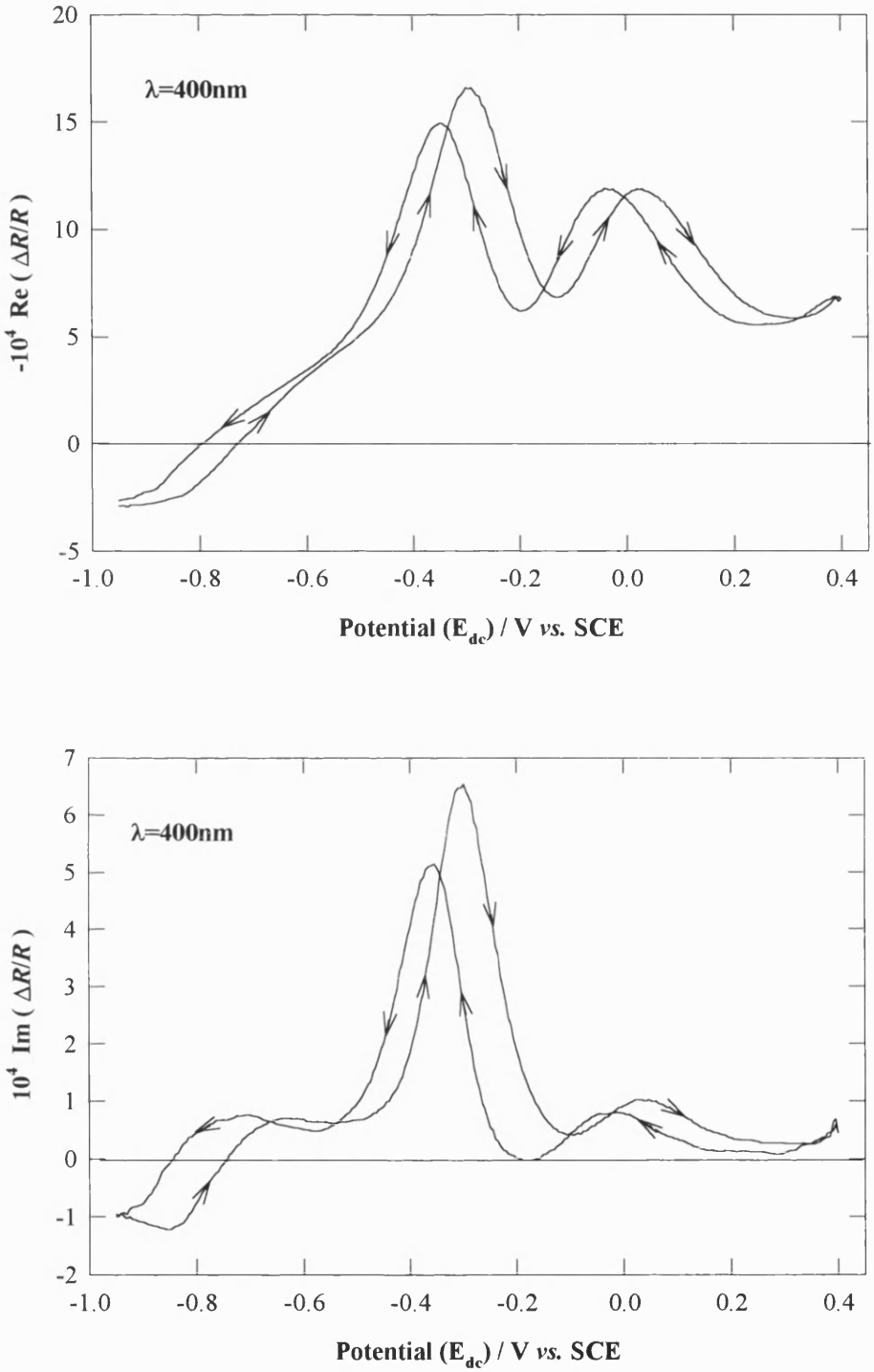

Figure 6.10 : PMR voltammogram of an Ru-Ir alloy in alkali media. λ=400nm, E_o=10mV rms, modulation frequency=1Hz; $C_{[NaOH]}$=0.1M.

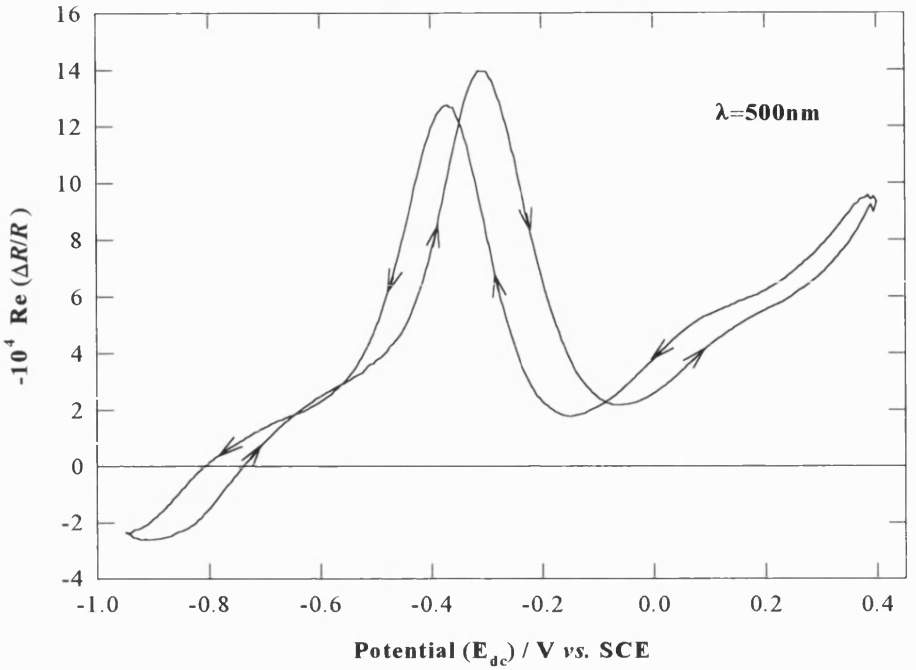

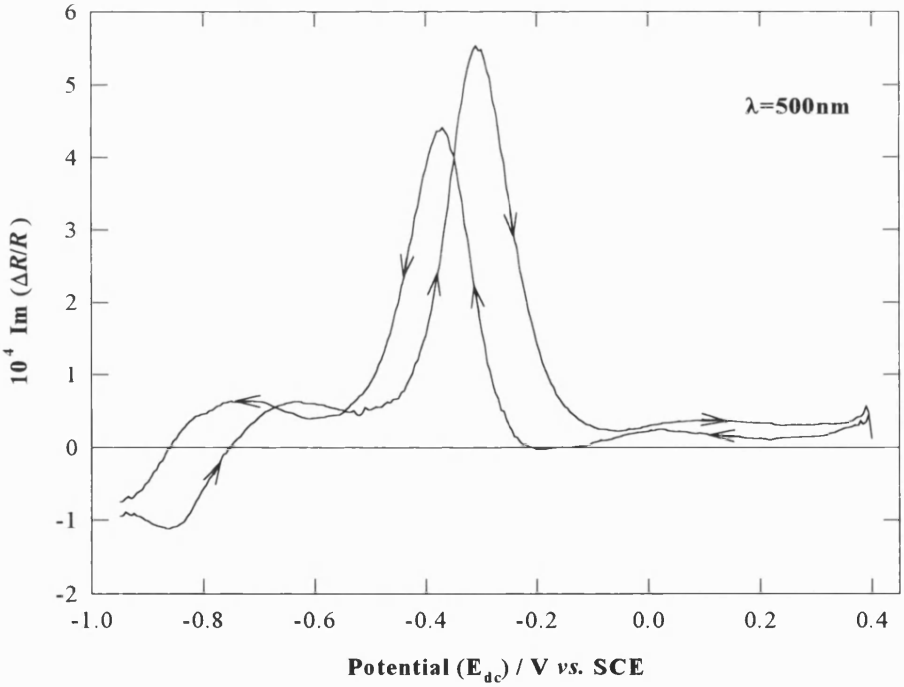

Figure 6.11 : PMR voltammogram of an Ru-Ir alloy in alkali media. λ=400nm, E_o=10mV rms, modulation frequency=1Hz; $C_{[NaOH]}$=0.1M.

6.2.4 Frequency response analysis

Preliminary frequency response analysis studies of Ru-Ir alloys were performed at a modulation frequency of 1Hz and amplitude of 10mV rms. **Figure 6.12** illustrates the frequency dependent optical response recorded of a Ru-Ir alloy at E_{dc}=-0.40V and λ=320nm. These conditions correspond to the electrochromic region previously identified by PMR spectroscopy. A characteristic semi-circle is observed over the frequency range ω=1 - 10^3Hz. The frequency dependent response at λ=320nm therefore confirms that the reversible redox process observed during cyclic voltammetry involves a surface film process. It should be noted that in order to derive kinetic information regarding the reversible electrochromic effect, it is necessary to know the spectroscopic properties (i.e. ε) of the surface film. It was not possible to carry out ellipsometry studies of the surface films to provide this information. Therefore in this study, frequency response analysis of the optical response of Ru-Ir alloys was limited to its use as a diagnostic for surface redox processes.

Similar frequency dependent optical responses were obtained at E_{dc}=0.00 and E_{dc}=0.40V. **Figure 6.13** illustrates the frequency dependent optical response recorded at E_{dc}=0.00V and λ=400nm. The frequency dependent optical response at E_{dc}=0.40V and λ=500nm is also shown in **Figure 6.14**. The semi-circular responses observed at both potentials confirms that the PMR spectra observed at E_{dc}=0.0 and 0.40V are also associated with surface redox processes.

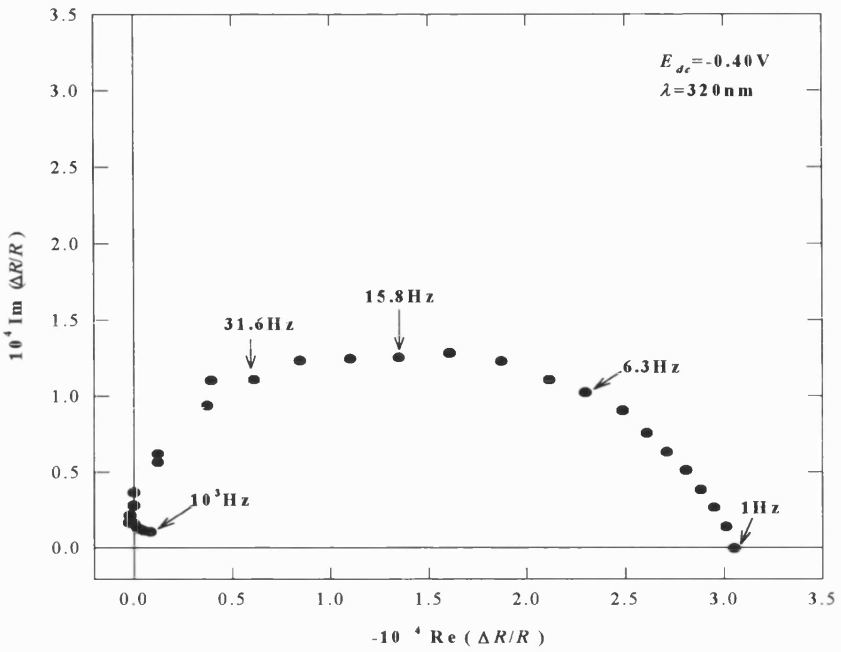

Figure 6.12 : Frequency response analysis of the PMR response of a Ru-Ir alloy in the electrochromic region. E_{dc}=-0.40V; E_o=10mV rms; λ=320nm; $C_{[NaOH]}$=0.1M.

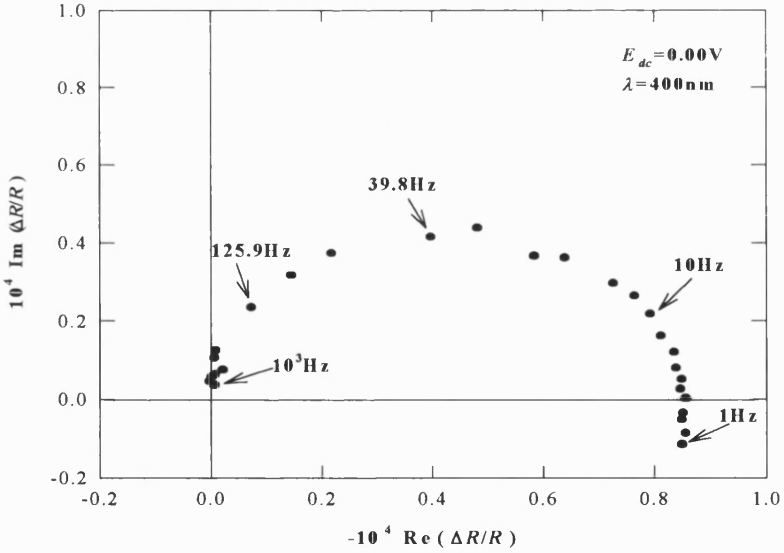

Figure 6.13 : Frequency response analysis of a Ru-Ir alloy. E_{dc}=-0.00V; E_o=10mV rms; λ=400nm; $C_{[NaOH]}$=0.1M.

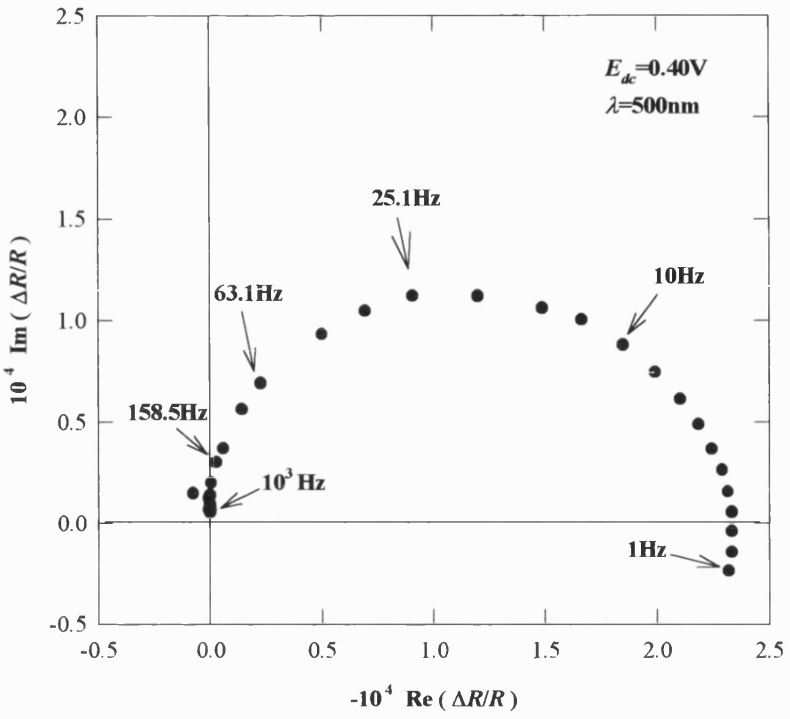

Figure 6.14 : Frequency response analysis of a Ru-Ir alloy. E_{dc}=-0.40V; E_o=10mV rms; λ=500nm; $C_{[NaOH]}$=0.1M

6.3 Discussion and Conclusions

PMR studies of the $Ru_{0.4}Ir_{0.6}$ alloy have shown that the surface electrochemistry of an electrodeposited Ru-Ir alloy is dominated by iridium. An electrochromic effect has been observed at the reversible peak (E=-0.36V) which is attributed to the Ir(III) $\rightleftharpoons$ Ir(IV) redox couple. The PMR spectra are consistent with those reported by Gutiérrez *et al.* [25] for an anodically grown iridium oxide film in alkali media, over the same potential range.

It is interesting to note that several authors have reported that surface enrichment of Ru-Ir anodes with Ir occurs using XPS and Auger spectroscopy [6-9,34,35]. In

PMR spectroscopy, only the optical properties of the oxide film layer formed on the metal electrode of interest, are studied. Penetration of the light source into the metal layer is ~0. As a result, the technique is surface sensitive. The predominant electrochemical response of iridium at Ru-Ir alloys therefore supports the surface segregation effects reported by these authors.

The frequency response analysis of Ru-Ir has been used as a diagnostic for surface redox processes both in the electrochromic region and the surface charge region. Further kinetic analysis of the frequency dependent optical response has not been possible due to a lack of available spectroscopic data regarding the surface films under study.

Further work is needed in this area to gain a complete understanding of the electrochromic effect observed at Ru-Ir alloys. The application of ellipsometry to Ru-Ir alloy films would provide valuable optical information regarding the surface oxide films [35]. The use of impedance spectroscopy in conjunction with PMR spectroscopy has been used to study electrochromic WO_3 thin films [37]. The two complementary techniques would therefore be applicable to the study of Ru-Ir alloys where an electrochromic effect has been observed by PMRS.

Finally, the $RuO_4^{2-} \rightleftharpoons RuO_4^-$ redox couple was not observed during O_2-evolution in alkali media. This demonstrates the stabilising effect of iridium on ruthenium electrochemistry.

References

1. S. Trasatti and W.E. O'Grady, in "Advances in Electrochemistry and Electrochemical Engineering", vol. 12, H. Gerischer and C.W. Tobias, Editors, p. 177, Interscience, New York (1981)
2. C. Iwakura, K. Hirao and H. Tamura, *Electrochimica Acta*, **2**, 329 (1977)
3. R. Kötz, S. Stucki, D. Scherson and D.M. Kolb, *J. Electroanal. Chem.*, **172**, 211 (1984)
4. A. Bewick, C. Gutierrez and G. Larramona, *J. Electroanal. Chem.*, **332**, 155 (1992)
5. R.S. Yeo, J. Orehotsky, W. Visscher and S. Srinivasan, *J. Electrochem. Soc.*, **128**, 1900 (1981)
6. R. Kötz and S. Stucki, *J. Electrochem. Soc.*, **132**(1), 103 (1985)
7. R. Kötz and S. Stucki, *Electrochimica Acta*, **31**(10), 1311 (1986)
8. C. Angelinetta, S. Trasatti, Lj.D. Atanasoska and R.T. Atanasoski, *J. Electroanal. Chem.*, **214**, 535 (1986)
9. C. Angelinetta S. Trasatti, Lj.D. Atanasoska, Z.S. Minevski and R.T. Atanasoski, *Mat. Chem and Phys.*, **22**, 231 (1989)
10. V. V. Gorodetskii, V.A. Neburchilov and M.M. Pecherskii, *Russian J. Electrochem.*, **30**(8), 916 (1994)
11. M. Vukovic, D. Čukman, M. Milan, L.D. Atanasoska and R.T. Atanasoski, *J. Electroanal. Chem.*, **330**, 663 (1992)
12. D.N. Buckley and L.D. Burke, *J. Chem. Soc., F.T.1*, **71**, 1447 (1975)
13. D.N. Buckley and L.D. Burke, *J. Chem. Soc., F.T.1*, **72**, 2431 (1975)
14. S. Gottesfeld and S. Srinivasan, *J. Electroanal. Chem.*, **86**, 89 (1978)
15. R. Kötz, H. Neff and S. Stucki, *J. Electrochem. Soc.*, **131**, 72 (1984)

16. J. Mozota and B.E. Conway, *J. Electrochem. Soc.*, **128**(10), 2142 (1981)

17. S. Gottesfeld, J.D.E. McIntyre, G. Beni and J.L. Shay, *Appl. Phys. Lett.*, **33**(2), 208 (1978)

18. G. Beni and J.L. Shay, *Appl. Phys. Lett.*, **33**(7), 567 (1978)

19. S. Gottesfeld and J.D.E McIntyre, *J. Electrochem. Soc.*, **126**(5), 742 (1979)

20. J.D.E McIntyre, W.F. Peck, Jr. and S. Nakahara, *J. Electrochem. Soc.*, **127**(6), 1264 (1980)

21. J.D.E. McIntyre, S. Basu, W.F. Peck, Jr., W.L. Brown and W.M. Augustyniak, *Phys. Rev. B.*, **25**(12), 7242 (1982)

22. J. Mozota and B.E. Conway, *Electrochimica Acta*, **28**(1), 1 (1983)

23. B.E. Conway and J. Mozota, *Electrochimica Acta*, **28**(1), 9 (1983)

24. S. Hädzi-Jordanov, H. Angerstein-Kozlowska and B.E. Conway, *J. Electroanal. Chem.*, **60**, 359 (1975)

25. C. Gutiérrez, M. Sánchez, J.I. Peña, C. Martinez and M.A. Martinez, *J. Electrochem. Soc.*, **134**(9), 2119 (1981)

26. C.G. Granqvist, *Appl. Phys. A*, **57**, 3 (1993)

27. See e.g. P.A. Cox, "*The electronic structure and chemistry of solids*". Oxford University Press (1987)

28. A.K. Goel, G. Skorinko and F.H. Pollak, *Phys. Rev. B.*, **24**(12), 7342 (1981)

29. T.M. Silva, A.M.P. Simões, M.G.S. Ferreira, M. Walls and M.D.C. Belo, *J. Electroanal. Chem.*, **441**, 5 (1998)

30. S.H. Glarum and J.H. Marshall, *J. Electrochem. Soc.*, **127**(7), 1467 (1980)

31. R. Kötz and S. Stucki, *J. Electrochem. Soc.*, **130**(4), 825 (1983)

32. D. Ĉukman, M. Vukovic and M. Milan, *J. Electroanal. Chem.*, **389**, 209 (1995)

33. K.S. Kang and J.L. Shay, *J. Electrochem. Soc.*, **130**(4), 766 (1983)

34. I.M. Kodintsev, S. Trasatti, M. Rubel, A. Wieckowski and N. Kaufher, *Langmuir*, **8**(1), 283 (1992)

35. Lj Atanososka, R. Atanasoski and S. Trasatti, *Vacuum*, **40**(1-2). 91 (1990)

36. A.J. Bard and L.R. Faulkner, "*Electrochemical Methods, Fundamentals and Applications*", Wiley & Sons, p. 583 (1980)

37. J.J. Kim, D.A. Trk, T. Amemiya, K.Hashimoto and A. Fujishima, *J. Electroanal. Chem.*, *435*, 31 (1997)

Chapter 7

Chapter 7

Conclusions and Future Work

It has been demonstrated that Potential-Modulated Reflectance Spectroscopy is a powerful diagnostic tool for studying electrochemical processes. The theoretical relationship between the optical response and electrical response at an electrode-electrolyte interface has been derived and a direct relationship between optical response and Faradaic admittance has been established. In particular, it has been shown how the use of frequency response analysis enables the distinction between surface and solution processes to be made.

The ferro-ferricyanide redox couple has been used as a model diffusion-controlled redox system to verify the theoretical principles derived for the frequency dependent optical response of solution species. A direct relationship between the frequency dependent optical response and Faradaic admittance of the system under study has been verified. Since PMR spectroscopy is primarily sensitive to the Faradaic component of the frequency dependent response of an electrochemical system, it follows that the complimentary techniques of *ac* impedance and frequency dependent PMR can be used to distinguish between Faradaic and non-Faradaic processes.

The major area of research in the thesis has been centred around the study of ruthenium-based electrocatalytic electrodes used in the chlor-alkali industry. Previous work in this area has been directed towards understanding the kinetics and mechanisms of the oxygen and chlorine evolution reactions and also understanding the structural properties of dimensionally stable anodes (DSAs®). However, there has been only limited research concerning oxidation states changes at metal oxide catalysts surface

during gas evolution. XPS studies have identified the role of Ru(VI) in the oxygen evolution process and some work has been carried out in an attempt to identify corrosion products formed during this process. In this work, PMR spectroscopy has been used to investigate oxidation state changes at the surface of metal / alloy electrode catalysts, in particular Ru metal and Ru-Ir alloy anodes.

PMR spectroscopic investigations of electrodeposited Ru metal electrodes have identified for the first time, Ru(VI) and Ru(VII) - in the form RuO_4^{2-} and RuO_4^- respectively, as corrosion products formed at the onset of oxygen evolution in alkaline media. The observed PMR peaks correlate well with the literature λ_{max} values of RuO_4^{2-} at 460nm and RuO_4^- at 385 and 315nm, measured by UV-Vis absorption spectroscopy in alkali media [1]. The PMR spectra were compared with the difference absorption spectrum of RuO_4^- and RuO_4^{2-} calculated from literature data. A shift in the isosbestic point of the PMR spectrum as a function of potential suggests that mass balance does not apply. This indicates that the electrochemistry at the electrode-electrolyte interface is more complicated that the simple reversible redox couple, $RuO_4^{2-} \rightleftharpoons RuO_4^-$.

Frequency response analysis confirmed that RuO_4^{2-} and RuO_4^- are present in solution. However, deviation of the low frequency slope from unity (the value expected for a diffusion-controlled process with no homogeneous complications) suggests that the redox species, RuO_4^{2-} and RuO_4^- are not in simple equilibrium via electron transfer. As a result, it is proposed that the electrochemistry of Ru anodes during O_2-evolution may involve a further chemical reaction, $4RuO_4^- + 4OH^- \rightarrow 4RuO_4^{2-} + 2H_2O + O_2$.

An interesting feature of the PMR response of Ru in alkaline solutions is observed at the high frequency limit. A semi-circular response confirms that a surface process occurs in conjunction with the solution electrochemistry discussed above. The high frequency optical response is attributed to a change in stoichiometry of a surface oxide

e.g. RuO_{2-x} $RuO_{2+x+\delta x}$. It is clear from frequency response analysis that the diffusion-controlled process, which corresponds to the formation of RuO_4^-, is complicated by a surface process, previously unidentified by PMR spectroscopy. This observation highlights the importance of using frequency response analysis in conjunction with PMR spectroscopy. Clearly, complete interpretation of PMR spectra carried out at single frequencies measurements can be confusing if frequency response analysis is not carried out. There are many examples of this in the literature.

Studies of Ru-Ir mixed alloy have shown that the electrochemical and PMR response is dominated by Ir. The PMR response at constant frequency is in excellent agreement with the PMR spectra previously reported for the electrochromic effect at iridium oxide electrode [2]. Frequency response analysis has been used in this study as a diagnostic tool to confirm that the PMR spectra are attributed to surface electrochemical processes. The work is consistent with previous XPS studies which have identified surface segregation of Ir at mixed Ru-Ir alloy / oxide anodes (see e.g. ref. [3-5]). Further work is necessary on this system to gain a full understanding of the electrochemistry of Ru-Ir anodes. Spectroscopic ellipsometry, for example, would provide valuable optical information for the particular Ru-Ir alloy under study which would then enable kinetic information to be derived regarding the electrochromic and oxidation processes that occur at the surface. The use of *ac* impedance spectroscopy in conjunction with PMR spectroscopy would also be useful as a tool for distinguishing between Faradaic and non-Faradaic processes at the electrode interface.

In conclusion, PMR spectroscopy promises to be a useful tool for *in-situ* investigations of electrode processes at catalytic metal / alloy surfaces. It is anticipated that the application of this technique to other electrocatalytic systems will help in

understanding how the nature of the anode material influences the kinetics and mechanisms of electrode reactions.

References

1. R.E. Connick and C.R. Hurley, *J. Am. Chem. Soc.*, **74**, 5012 (1952)

2. C. Gutiérrez, M. Sánchez, J.I. Peña, C. Martinez and M.A. Martinez, *J. Electrochem. Soc.*, **134**(9), 2119 (1981)

3. R. Kötz and S. Stucki, *J. Electrochem. Soc.*, **132**(1), 103 (1985)

4. C. Angelinetta, S. Trasatti, Lj.D. Atanasoska and R.T. Atanasoski, *J. Electroanal. Chem.*, **214**, 535 (1986)

5. I.M. Kodintsev, S. Trasatt, M. Rubel, A. Wieckowski and N. Kaufher, *Langmuir*, **8**(1), 283 (1992)